Università di Napoli "Federico II"

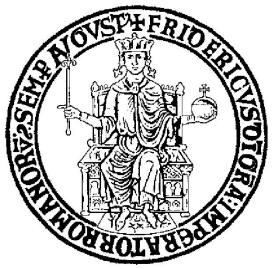

Dottorato di Ricerca
in
Fisica Fondamentale ed Applicata
XXII Ciclo

Improving the Virgo detector sensitivity: Effects of high power input beam and Electrostatic actuators for mirror control

dott. Simona Mosca

advisor: prof. Rosario De Rosa

referee: prof. Alberto Aloisio
prof. Enrico Santamato

To Ernesto

Contents

Introduction

This thesis is finalized to provide new scientific tools in order to improve the sensitivity of Virgo, a ground-based interferometric antenna for gravitational wave detection, located in Cascina (Pisa, Italy).
The gravitational waves were predicted by Einstein in 1916 as a consequence of general relativity theory. Their existence has been indirectly provided by R.A. Hulse and J.H. Taylor (Nobel Price 1993). They observed an orbital period decay of the binary star system PSR 1913+16, which was in agreement with the results predicted by gravitational wave emission.

The direct detection is extraordinarily difficult because gravitational waves interact weakly with matter and their amplitude is very small. Only the most dramatic process of the cosmos such as supernova explosion, interaction of black hole, merging of binary systems and catastrophic collisions between stars emit gravitational waves detectable with actual detectors. Their sensitivity depends on the emission frequency of gravitational waves. Specifically Virgo is a sophisticated interferometer with highly reflecting mirrors suspended to multipendula which effectively filter the seismic noise and with a high power laser sent in its arms. In recent years the gravitational waves detectors have achieved high levels of sensitivity thanks the big scientific and technologic efforts in the frequency band included between some Hz to some kHz.
Nevertheless at low frequency the seismic vibration limits the sensitivity. At medium frequency the sensitivity is instead limited by mirror thermal noise. Finally the shot noise is still dominant at high frequency. Furthermore elaborate control systems, combined with the high power laser and noisy instrument, generate additional technical noise.
Presently real chances to detect gravitational waves exist but the rate of ex-

pected events, on the basis of the astrophysical population models, is still low.
With the goal of increasing the sensitivity by about one order of magnitude, allowing us to see many events for years, hundreds of scientists are working to the realization of next generation of gravitational waves detectors.
Advanced materials and new technologies will be needed to reduce the principal noise sources. Promising alternatives to the main optical elements and control systems have been proposed, whose advantage and realizability have to be experimentally tested.
This work is part of an experimental analysis of two possible upgrades of the Virgo interferometer:

- Increasing of laser power of to 200W in order to reduce the Virgo Shot Noise.

- Using of electrostatic actuators for mirrors control to reduce the virgo mirror thermal noise and at the additional technical noise.

The **high power laser** produce thermal effects non negligible in the injection optics, in particular the right working of *Faraday isolator*, the device that isolates the laser by light back reflections, is really compromised. Faraday isolators satisfying these strong requirements, imposed by stabilization in frequency and intensity of beam laser for advanced detectors target are not commercially available. Therefore they are subject of research. Here we have a detailed study of the involved thermal effects and the proposed solutions were experimentally analyzed. Particular attention was direct to the analysis at induced birefringence by photoelastic effect of thermal strains with radial symmetry. The thermal strain produces problem in controlling the system because it introduces a mode conversion and an apparent depolarization of beam. This effect was studied in depth. A careful analysis allowed us to explain that its physical origin is due to a spin to orbital angular momentum conversion of light. This effect is typically generated in special optical devices, called Q-plate, used in quantum information. A comparison with these devices allowed us to understand the way of compensate this unwanted effect.

The **electrostatic actuators** are the most promising devices for mirror

control for the next generation of interferometric gravitational waves detectors. They were proposed to replace the coil-magnet system, presently used for the mirrors control in Virgo. An accurate characterization of the force exerted on the mirror by thess actuators was necessary to evaluate their dynamic range for a correct system design, satisfying the requirements in term of noise reintroduction and control reliability.
A typical problem that arises by using the electrostatic actuator is that *spurious charges* could appear on the mirror, generating additional forces. We show theoretically and experimentally a method to investigate their presence and experimentally show that the effect of stray patch charge on the mirror can be minimized by modulating the driving signal of the actuator.

This thesis is divided in four chapters:
In the **first chapter** is shown how the gravitational waves arise in General Relativity, using the so called weak-field approximation, and it is explained how they interact with matter. Furthermore an overview of possible sources of gravitational waves is presented, including the ones detectable by the Virgo interferometer. The last results obtained by the collaboration, born in 2007, with two Laser Interferometer GW Observatory (LIGO), in US are reported. Virgo and Ligo work today as a single detector, in order to map the sky in different directions, and to provide multiple coincidence in case of detection.
Second chapter: The first scientific run of Virgo experiment took place in 2006. This allowed Virgo to increase its sensitivity and achieve about the design sensitivity. But Virgo is continuously in evolution. Actually, since July 2009, it works with a new upgraded technology version called Virgo+, and produces scientific data continuously since the start of the run. In this chapter we will show the general working principle of the interferometer as well as the single parts that compose it. Then we show the main upgrades finalized to achieve the sensitivity of the advanced interferometer.
The **third chapter** contains a description of Virgo injection system and show the study and the results about the thermal effect generated in the magneto-optics crystals housed in the Faraday isolator. Also the proposed compensation method is described. In particular it is shown that after the crystal the laser beam acquires orbital angular momentum, that disappears

if we use a suitable optical configuration. Then other thermal effects are analyzed by using Shark Hartmann sensor. The comparison with a numerical model are also reported

In the **fourth chapter**, after a short discussion about the advantage to use the electrostatic actuation system , we present the force measurements made in air and in high vacuum, with two different measurement methods, the first based on interferometric technique and the second based on a optical lever. A comparison of the results with a numerical model of the actuator force is also presented and the spurious charge investigation is illustrated and experimentally tested.

Chapter 1

Gravitational Waves

In this chapter we will briefly discuss how gravitational waves (GWs) of finite speed arise from General Relativity. We will use the "*linearized theory*" which consists of expanding the Einstein equations around the flat Minkowski metric $\eta_{\mu\nu}$, using the so-called weak-field approximation. This allow us to see immediately how a waves equation emerges and how these waves interact with a detector, idealized for the moment as a set of test masses.
A description of the main GWs sources is also presented.

1.1 Waves equation in General Relativity

In the theory of the general relativity of Einstein [1–5] the spacetime is not an infinitely rigid support as in special relativity but it is a dynamic medium that can be deformed. In other words in general relativity the interval ds between two points in the spacetime (x^μ and $x^\mu + dx^\mu$) is expressed as

$$ds^2 = g_{\mu\nu} dx^\mu dx^\nu \qquad (\mu, \nu = 1, 2, 3, 4). \tag{1.1}$$

Here $x^\mu = (-ct, x, y, x)$ (c is speed of light) and $g_{\mu\nu}$ represents the metric tensor which describes the geometry of spacetime. The structure and the evolution of metric tensor $g_{\mu\nu}$ are regulated by the Einstein field equations, which determine the $g_{\mu\nu}$ tensor and its derivatives as a function of the impulse-energy tensor of matter $T_{\mu\nu}$:

$$R_{\mu\nu} - \frac{1}{2} g_{\mu\nu} R = \frac{8\pi G}{c^4} T_{\mu\nu}. \tag{1.2}$$

where $R_{\mu\nu}$ is the Ricci tensor: contraction over two indices of the Riemann tensor $R_{\mu\nu\rho\sigma}$ ($R_{\mu\nu} = g^{\rho\sigma}R_{\mu\nu\rho\sigma}9$, G is the Newton's gravity constant and R is the scalar curvature $R = g^{\mu\nu}R_{\mu\nu}$, contraction of the Ricci tensor. These equations are non linear and in the general case cannot be analytically solved. In vacuum ($T_{\mu\nu} = 0$), the Einstein equation is simplified as

$$R_{\mu\nu} - \frac{1}{2}g_{\mu\nu}R = 0. \tag{1.3}$$

As the general theory contains the special relativity, the Minkowski metric $\eta_{\mu\nu}$ is a solution of the above equation.
The GWs are extremely weak, they can be approximated as small perturbations to the Minkowski flat metric. Therefore we write in weak-field approximation:

$$g_{\mu\nu} = \eta_{\mu\nu} + h_{\mu\nu} \tag{1.4}$$

with $|h| << 1$. In this way the equations can be linearized by expanding the tensor $R_{\mu\nu}$ to the first order in $h_{\mu\nu}$. The Einstein equations in vacuum become:

$$\Box h_{\mu\nu} - \frac{1}{2}\eta_{\mu\nu}\Box h = 0, \tag{1.5}$$

were $\Box = -(\frac{1}{c^2})\partial_{tt}^2 + \nabla^2$ and $h = \eta^{\mu\nu}h_{\mu\nu}$ is the perturbation's trace.
If we define the so called "$trace - free$" tensor:

$$\bar{h}_{\mu\nu} = h_{\mu\nu} - \frac{1}{2}\eta_{\mu\nu}h \tag{1.6}$$

and choosing the Lorentz gauge (also called harmonic gauge)

$$\partial^{\nu}\bar{h}_{\mu\nu} = 0, \tag{1.7}$$

the Einstein equations reduce to:

$$\Box\bar{h}_{\mu\nu} = 0. \tag{1.8}$$

Since this equation is the waves equation, the metric perturbations $\bar{h}_{\mu\nu}$, outside the source, propagate at the speed of light through the space-time and are called gravitational waves.

1.2 Propagation of GWs and their interaction with test masses

A generic solution of equation (1.8) can be written as superposition of plane waves of the kind:

$$\bar{h}_{\mu\nu} = \epsilon_{\mu\nu} e^{ik_\sigma x^\sigma} + \epsilon^*_{\mu\nu} e^{-ik_\sigma x^\sigma} \qquad k^\sigma k_\sigma = 0 \tag{1.9}$$

where $\epsilon_{\mu\nu}$ is a symmetric tensor 4x4 and only six of its ten independent components reamain free, due to four conditions imposed by the lorentz gauge (1.7), that in the case of the (1.9) solutions became $k^\mu \epsilon_{\mu\nu} = 0$. It is possible to further reduce the degrees of freedom by exploiting a residual arbitrariness respect to coordinate transformations $x^\mu \to x^\mu + \xi^\mu$, generated by functions $\xi_\mu(x)$ satisfying the equation $\Box \xi_\mu = 0$. In particular we can choose ξ_μ such that:

$$\epsilon^i_i = 0 \qquad Traceless \tag{1.10}$$

That togheter to

$$\epsilon^i k_i = 0. \qquad Transverse \tag{1.11}$$

defines the $transverse - traceless$ gauge, or TT gauge and we will denote the relative metric by $h^{TT}_{\mu\nu}$. It is interesting to note that plugging eq. (1.10) in eq. (1.6) we obtain that $\bar{h}_{\mu\nu} = h^{TT}_{\mu\nu}$.
The tensor $\epsilon_{\mu\nu}$ is called the polarization tensor and in TT gauge is reduced to:

$$\begin{pmatrix} 0 & 0 & 0 & 0 \\ 0 & \epsilon_{11} & \epsilon_{12} & 0 \\ 0 & \epsilon_{12} & -\epsilon_{11} & 0 \\ 0 & 0 & 0 & 0. \end{pmatrix} \tag{1.12}$$

We define $\epsilon_{11} = h_+$ and $\epsilon_{12} = h_\times$ and, in the case of GW propagating along the z axis, we can write:

$$h^{TT}_{ab} = \left(\begin{pmatrix} h_+ & 0 \\ 0 & -h_+ \end{pmatrix} + \begin{pmatrix} 0 & h_\times \\ h_\times & 0 \end{pmatrix} \right)_{ab} cos(\omega t - kz)) \tag{1.13}$$

where $a, b = 1, 2$ are indices in the transverse (x,y) plane; h_+ and $h_\times$ are called the amplitudes of the "plus" and "cross" polarization waves with relative angle of 45 degrees. In terms of the interval ds^2 :

$$\begin{gathered} ds^2 = -c^2 dt^2 + dz^2 + [1 + h_+ cos(\omega t - kz)] dx^2 \\ + [1 + h_- cos(\omega t - kz)] dy^2 + 2 h_\times cos[\omega t - kz] dx dy. \end{gathered} \tag{1.14}$$

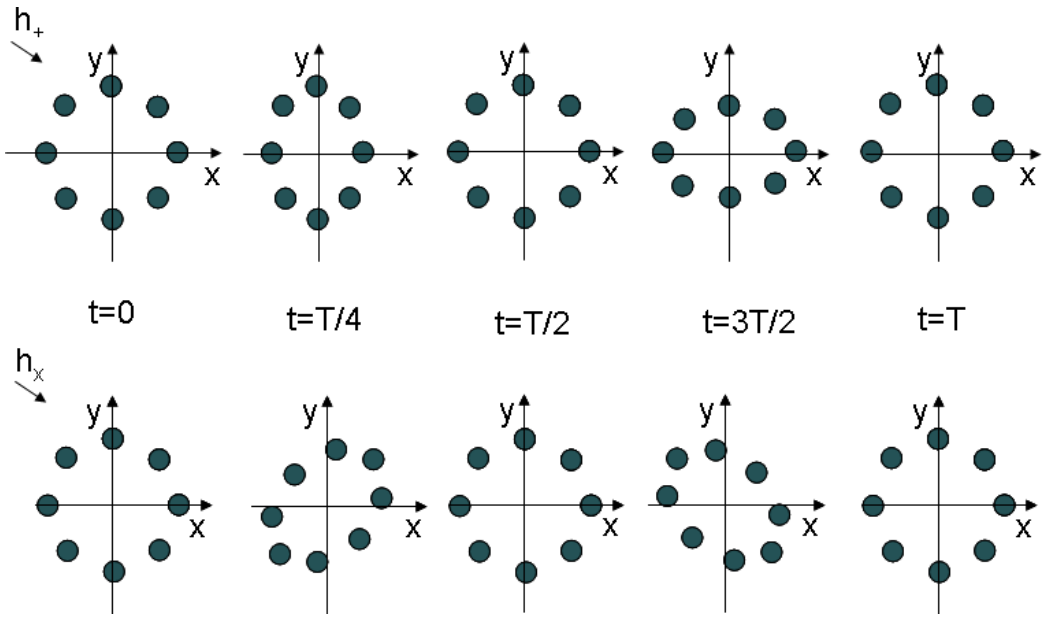

Figure 1.1: The effect of a passage of a gravitational wave on a ring of free masses.

where we used the eq. (1.1), (1.4) and (1.13) If we consider a GW investing a ring of freely-falling masses, we will observe oscillation of their relative distances described by eq. (1.14). In particular, let us suppose to have two masses along x axis, in the points of spacetime $(t, x_1, 0, 0)$ and $(t, x_2, 0, 0)$ such that $x_1 - x_2 = L$, and a h_+ polarized GW propagating along z, the 1.14 becames :

$$ds^2 = 1 + h_+ cos(\omega t) dx^2. \tag{1.15}$$

By integrating we obtain:

$$s = L[1 + \frac{1}{2} h_+ cos(\omega t)]. \tag{1.16}$$

Therefore, the proper distance changes periodically in time because of the GW. This effect will be more evident as much as the length L and the amplitude h+ will be greater.
In Fig. 1.1 are shown the deformations of a ring of test masses associated with the two modes of polarization h_+ e $h_\times$ where the positions of the masses are schematically represented at different fractions of an oscillation period T.

1.3 Sources of Gravitational Waves

Linearizing the equation of Einstein (1.2) using the (1.4), in presence of matter (source) we obtain:

$$\Box h_{\mu\nu} = -\frac{16\pi G}{c^4} T_{\mu\nu}. \tag{1.17}$$

Therefore the impulse-energy tensor produces a perturbation of the surrounding space-time metric.
The solution of this equation is:

$$h_{\mu\nu}(r,t) = \frac{4G}{c^4} \int d^3\vec{x'} \frac{[T_{\mu\nu}]_{t-r/c}}{r} \tag{1.18}$$

where $r = |\vec{x'} - \vec{x}|$ is the distance from the source to the observer. Under the hypothesis that the dimension of the source R is much smaller respect to the distance from the observation point, it is possible to perform a multipole expansion like for electromagnetic waves. By replacing the electric charge with the source mass, we can define the dipole moment of mass as the electric dipole moment. From the conservation of momentum and angular momentum laws, we obtain that the first non-zero term is the quadrupole momentum:

$$h_{\mu\nu}(r,t) = \frac{2G}{c^4} \frac{1}{r} [\frac{d^2}{dt^2} I_{\mu\nu}]_{t-r/c} \tag{1.19}$$

where $I_{\mu\nu} = \int d^3\vec{x}\rho\big(x_\mu x_\nu - \frac{1}{3}|\vec{x}|^2\big)$ is the quadrupole momentum associated with the density of the source $\rho(x,t)$. It is important noting that the amplitude of the wave in (1.19) is different by zero, only when the symmetry of source is not spheric.
To estimate the order of magnitude of the intensity of such radiation, we consider a body of mass M and size R and the approximate his quadrupole momentum with $Q = \epsilon R^2 M$, where ϵ is a factor measuring the asymmetry of the mass distribution. We can write:

$$h \sim \epsilon^2 \frac{GM}{c^2} \frac{1}{r} \big(\frac{v}{c}\big)^2 \tag{1.20}$$

where v is the typical speed v of internal motion of the body. Since the factor $\frac{G}{c^2} = 7.4 \cdot 10^{-28} m/Kg$ is very small, by the (1.20) we can deduce that the emitted gravitational waves assume a consisting amplitude only

for relativistic and compact objects. Therefore we understand the difficulty to generate in laboratory detectable gravitational wave. Then, our efforts will be concentrated on the detection of gravitational waves generated by astrophysics sources. The universe becames our laboratory.
The GWs are classified into three types according to the wave form:

1. Periodic GW sources: spinning neutron stars (pulsars), binary systems of massive compact object.
   The temporal behavior of these sources is sinusoidal with frequency f constant over time of the order of observation time.

2. Burst GW sources: supernova explosion, final coalescence of compact binary systems.
   The duration of these events is smaller than observation time.

3. Stochastic GW sources: cosmologic sources related to the Big-Bang
   Their amplitude vary casually.

1.3.1 Periodic sources

Pulsars

The Pulsars with mass distribution asymmetric with respect the rotation axis emit GWs at frequency twice of the rotating frequency. The amplitude of the wave depends by the momentum of inertia of the star I_{zz}, by the distance from the Earth r, by the ellipticity ϵ in the equatorial plane, and by the frequency emission f. We can estimate that [6]:

$$h \sim 8 \cdot 10^{-19} \epsilon \Big(\frac{I_{zz}}{10^{38} Kgm^2}\Big) \Big(\frac{f}{1KHz}\Big)^2 \Big(\frac{10Kpc}{r}\Big) \tag{1.21}$$

Generally, since the ellipticity is small (about $\epsilon = 10^{-5}$), the amplitude is very small, but the periodicity allows to integrate over a sufficiently long time to improve the sinal-to-noise ratio. An example interesting in our galaxy is the Crab pulsar. The emission frequency is 60 Hz, the estimated amplitude is of the order of 10^{-24}.

Coalescent binaries

Binary system composed by two coalescent strongly compact, as two neutron stars (NS), two black holes (BH) or a neutron star and a black hole lose considerable energy by means of gravitational radiation. These systems are very important for the physics community, because in 1993 J.H.Taylor and R.A. Hulse gained the nobel price, obtaining a proof indirect of the existence of gravitational waves by observation of one of these. They observed that the orbital period decay of the binary system PSR 1913+16 was perfectly in agreement with the results predicted by gravitational wave emission [7]- [8]. The frequency of the emitted wave is double of the orbital one, and it increases as the two bodies become closer, until they merge together. The lifetime of these objects can be of millions of years (for the PSR 1913+16 is 10^8 years), but the gravitational radiation can be detected directly only in the last minutes of their life, when the orbital frequency is above several hertz and amplitude is large enough to be detected.

1.3.2 Supernovae explosion

The supernovae explosions are the result of the gravitational collapse of nuclei of stars enough massive. The amplitude of the GWs, emitted during the explosion (few milliseconds), depend on the velocity and asphericity of the collapse and on the amount of energy ΔE emitted, but the modeling of this kind of events is very difficult. An estimate can be given by [6]

$$h = 2.7 \cdot 10^{-20} \Big(\frac{\Delta E}{M_{\odot} c^2}\Big)^{\frac{1}{2}} \Big(\frac{1KHz}{f}\Big)^{\frac{1}{2}} \Big(\frac{10Mpc}{r}\Big). \tag{1.22}$$

In our galaxy, that is in a radius of about 10 kpc, it is estimated few Supernova explosions per century. In the Virgo cluster (at about 10 Mpc from the Earth), it is expected some event for year.

1.3.3 Stochastic background (SGWB)

The incoherent sum of random gravitational wave signals coming from astrophysical sources generate a stochastic background. But the SGWB have also a cosmologic origin that make it very interesting. Fellowing the pre-Big-Bang

model and standard inflationary model, in the early phases of the evolution of the Universe, GWs can be produced by the mechanism of amplification of vacuum fluctuations. Once produced, the GWs travel through space-time at the speed of light as we know, and are essentially unaffected by the matter they encounter. As a result, GWs emitted shortly after the Big Bang (and observed today in SGWB) would carry unaltered information about the physical processes that generated them. Therefore the SGWB should carry also a unique signatures from the earliest epochs in the evolution of the Universe, inaccessible to standard astrophysical observations.
The SGWB is usually described in terms of the gravitational-wave spectrum:

$$\Omega_{GW}(f) = \frac{f}{\rho_c}\frac{d\rho_{GW}}{df} \tag{1.23}$$

where ρ_{GW} is the energy density of gravitational radiation contained in the frequency range f to df and ρ_c is the critical energy density of the Universe. About this amplitude it is possible only to put upper limits [10]. The last results [11], using the data from about two-year science run of the Laser Interferometer Gravitational-wave Observatory (LIGO), constrain the $\Omega_{GW}(f)$ to be $< 6.9 \cdot 10^{-6}$ at 95% confidence, in the frequency band around 100Hz. This results constitute an improvement of more than an order of magnitude over the previous LIGO result, and improve on the indirect limits from BBN (Bing Bang nucleosynthesis) and cosmic microwaves background (CMB); this is one of the major milestone that which LIGO was designed to achieve.

Chapter 2

Virgo+ Experiment

In the previous chapter we have observed that a GW modifies the flat spacetime. Now we consider a light ray that propagating between two test masses interacting with a GW. We can understand that there will be a change of phase of light because of the GW passage. These light phase displacements are detectable by the well know interferometric methods. Therefore the more promising GWs detectors are interferometer. In particular Virgo is very sophisticated Michelson interferometer born by a collaboration between italian INFN and franch CNRS and it is located in Cascina near Pisa (Italy). Actually by July 2009, in its new upgraded technology called Virgo+, it is in scientific run together with two Laser Interferometer GW Observatory (LIGO) in the US. In this chapter we will show the general working principle of the interferometer and of the single part that composed it. Particular attention will be given to the fundamental and technical noise sources strictly linked to the sensitivity of the detector . In the last section we will discuss about some R&D projects aimed to develop an advanced generation of detectors with a remarkably improved sensitivity.

2.1 GWs Interferometric Detection

We consider a plus-polarized gravitational wave h_+ of frequency $\nu_g = \frac{\omega_g}{2\pi}$ traveling along the z direction, the effect on the metric will be given by

$$ds^2 = c^2dt^2 + (1 + h_+)dx^2 + (1 - h_+)dy^2. \tag{2.1}$$

Let us consider a the round trip experiment, in which a light ray is firstly emitted from a point placed at $x_0 = 0$ at time t_0, then received at point at $x_1 = L > 0$ at time t_1. Since we know that the light in the vacuum, follows a null geodesic, the (2.1) becomes:

$$0 = c^2dt^2 + (1 + h_+)dx^2 + (1 - h_+)dy^2. \tag{2.2}$$

It can be shown [12] that the round trip time of the pulse light depends on the gravitational wave amplitude and frequency and is given by

$$t_r = t_0 - \epsilon\frac{2L}{c} + h\frac{L}{c}\text{sinc}\frac{\omega_{GW}L}{c}\cos(\omega_{GW}(t - L/c)). \tag{2.3}$$

Where $\epsilon = 1$ for the x direction and -1 for the y, and where we substituted h_+ with h.
Consider now two light pulses of wavelength λ and wave vector $|\overrightarrow{k}| = 2\frac{\pi}{\lambda}$ emitted on a free falling mass in the origin of the coordinate system toward two other masses at a distance L along the x and y axes, reflected back to the origin and detected there. The two pulses arrive at the origin, traveling different the optical due to effect of GW, with a dephasing given by :

$$\delta\Phi_{GW} = \frac{4\pi hL}{\lambda}\text{sinc}\frac{\omega_{GW}L}{c}\cos(\omega_{GW}(t - L/c)). \tag{2.4}$$

Where the term $(\frac{\omega_{GW}L}{c})$ is close to 1 for gravitational waves of frequency below few thousands of Hz.
Therefore by observing this little dephasing, in principle, we can have a direct measurement of amplitude h of the GW.

2.2 Michelson interferometer

The simplest optical configuration for detecting a small light dephasing is a Michelson interferometer. A laser beam impinges on a half reflecting beam splitter, the two emerging beams are sent toward orthogonal directions, reflected back by two mirrors and they recombine at the beam splitter see fig. 2.1. The static tuning $\alpha = 2k(l_a - l_b)$ of the interferometer is the phase difference at the beam splitter between the two reflected beams without considering the effect of any GWs.

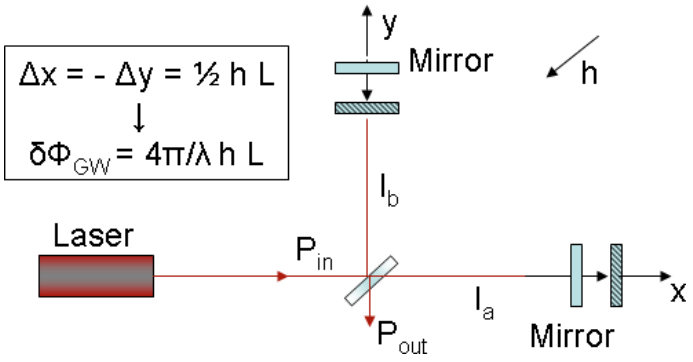

Figure 2.1: Effect of a gravitational wave over a Michelson interferometer, the GW is z propagating (perpendicularly to the plane of the figure.)

The power detected at the output port is:

$$P_{out} = \frac{P_{in}}{2}\frac{r_a^2 + r_b^2}{2}[1 + Ccos(\alpha)] \tag{2.5}$$

where C is the contrast which depends on the reflectivity of the two mirrors r_a and r_b:

$$C = \frac{2r_a r_b}{r_a^2 + r_b^2}, \tag{2.6}$$

that is equal to 1 for perfectly reflecting mirrors .
When a gravitational wave passes through the Michelson interferometer, the light beams interfere at the output port undergo an additional different dephasing given by eq. 2.4:

$$P_{out}^{GW} = \frac{P_{in}}{2}\frac{r_a^2 + r_b^2}{2}[1 + Ccos(\alpha + \delta\Phi_{GW})]. \tag{2.7}$$

The effect is a variation of the power detected at the output port which can be expressed developing at first order the (2.7):

$$P_{out}^{GW} - P_{out} = \delta P_{out}(t) = \frac{P_{in}}{2}\frac{r_a^2 + r_b^2}{2} C sin\alpha \cdot \delta\Phi_{GW}(t) \tag{2.8}$$

2.3 Noise sources

In previous paragraphs we seen that the interferometric detection of gravitational waves essentially consists in the measurement of phase-difference

of the beams in the two interferometer arms. This can be done simply by measuring the intensity at the output port of the interferometer. But this detection is not so simple due by the extreme smallness of GWs amplitude. We need a very sensitive interferometer on the measurement frequencies band. Therefore is very important to analyze and to reduce all noises that arise during the detection. The noise sources are really numerous and they can be divided in three types:

- fundamental noise sources: connected with fundamental physical processes;
- seismic noises sources: related to the ground motion;
- technical and environmental noise sources: mainly due to environmental disturbances and control systems of the interferometer.

2.3.1 Seismic noise

The amplitude of the seismic noise is strictly connected to the location of the detector and to human activities.
The seismic vibrations of the ground are many order of magnitude greater than the displacements which we need to detect. Typically, above some Hz, the spectrum of seismic vibrations is well approximated by the empirical expression:

$$x_s = \frac{a}{f^2}\frac{m}{\sqrt{Hz}} \tag{2.9}$$

with $10^{-7} < a < 10^{-6}$. If these vibrations propagate to the mirror, producing a displacement x_s, it will be possible to detect a gravitational wave of amplitude h only if $h > x_s/L$, independently by the use of any technique of optical amplification of the signal. It follows that it is possible to reduce the effect of vibrations x_s, induced by seismic noise, only by increasing the interferometer arm-length. But since it is not possible to build interferometer with arm-length greater than a few km, it is necessary to implement very efficient seismic noise attenuation systems.
An effective attenuation system consists of a chain of pendula in cascade. By considering a mirror suspended to a pendulum of frequency ω_0 and time constant $\tau = \frac{2\pi}{\omega_0}$. The mirror displacement x_a, induced by a seismic vibrations

x_s of the suspension point, is:

$$x_a = A(\omega)x_s = \frac{\omega_0^2}{-\omega^2 + \omega_0^2 + i\frac{\omega}{\tau}}x_s \tag{2.10}$$

The function $A(\omega)$ is called the transfer function of the pendulum. $A(\omega)$ has a maximum (in module) at resonance frequency ω_0 of the pendulum . For frequencies $\omega >> \omega_0$ the behavior is:

$$\frac{x_a}{x_s} = -\frac{\omega_0^2}{\omega^2} \tag{2.11}$$

that is, for frequencies larger than the resonance one, the seismic vibrations are attenuated by a factor $\frac{x_a}{x_s} = -\frac{\omega_0^2}{\omega^2}$. Then a pendulum is a mechanical lowpass filter with cut-frequency ω_0. Therefore, for a fixed frequency $\omega > \omega_0$, we can increase the attenuation by lowering the resonance frequency of the pendulum and by using several pendula in cascade. In fact for a chain of N pendula with resonance frequence $\omega_0, \omega_1, ...\omega_{N-1}$ rispectly, the attenuation factor will be:

$$\sqrt{A_N} = \frac{\omega_0 \cdot \omega_1 \cdots \omega_{N-1}}{\omega^N} \tag{2.12}$$

2.3.2 Fundamental noise sources

Shot noise, radiation pressure noise and quantum limit

The shot-noise is due to the statistic fluctuation of the number of photons present in the laser beam coming on the photodiode at the output port of the interferometer. In particular, the uncertainty in measuring the phase and the photons number is regulated by the quantum uncertainty relation $\Delta\Phi\Delta n > 1$. Considering that photons emitted by a laser are in a coherent state, we can assume that they have a poissonian distribution, then $\Delta n = \sqrt{n}$, following an uncertainty on the phase given by:

$$\Delta\Phi = \sqrt{\frac{h\omega}{\eta P_0}} \tag{2.13}$$

where P_0 is the power of the input laser, $\frac{\omega_L}{2\pi}$ is the frequency of the laser, η the quantum efficiency of the photodiode and t is the measure time.
If we compare this noise with the amplitude of a gravitational wave signal

given by the equation (2.4), we can find a limit for the minimum h allowed value:

$$h = \frac{1}{L}\sqrt{\frac{\hbar c\lambda}{2P_0}}\frac{1}{\sqrt{Hz}}. \tag{2.14}$$

where we supposed $\frac{\omega_{GW}L}{c} << 1$. It is interesting to note that this noise don't depend by GW frequency.

From eq. (2.14) we can see that it is possible to reduce the shot-noise effect by increasing the input power P_0. The thirth chapter of this thesis will be dedicated to this subject.

But the power cannot increase away because there is a quantum limit due by the noise induced by the pressure fluctuations on the mirrors. In fact, the mirrors are subject to a force F due to the radiation pressure: $F = 2n\frac{\hbar\omega}{c}$ where n is the number of photons which impinges on the mirror per time unit. Each fluctuation of the photon flux produces a variation of the force F and then a displacement of the mirror. It can be show [6] that the radiation pressure noise is:

$$h_{rp}(f_{GW}) = \frac{1}{mf_{GW}^2 L}\sqrt{\frac{\hbar P_{in}}{2\pi c\lambda}} \tag{2.15}$$

where m is the mirror mass. Thus we have two different sources of noise associated with the quantum nature of light. Note that they have opposite scaling with the light power: shot noise declines as the power grows, but radiation pressure noise grows with power.

We can consider these two noise sources to be two face of a single noise; we call it *optical redout noise*, given by quadrature sum:

$$h_{o.r.n.}(f_{GW}) = \sqrt{h_{shot}^2 + h_{rp}^2(f_{GW})}. \tag{2.16}$$

At very low frequencies, the radiation pressure term (proportional to $\frac{1}{f^2}$) will dominate, while at higher frequencies the shot noise (which is independent of frequency) is more important. Furthermore at any given frequency f_0, there is a minimum noise spectral density; clearly, this occurs when the power P_{in} is chosen to have the value P_{opt} that yields $h_{shot} = h_{rp}(f_0)$.The power that satisfies this relation is

$$P_{opt} = \pi c\lambda m f^2. \tag{2.17}$$

P_{opt} is typically quite large $\sim$ 1 Megawatt for $f_{GW} = 100Hz$. Therefore generally the GW interferometers (also the next generation ones) run well

below their optimum power, and have shot noise larger than the optimum. When we plug this expression for P_{opt} into formula for $h_{o.r.n}$ we find:

$$h_{QL}(f_{GW}) = \frac{1}{\pi f_{GW}} L \sqrt{\frac{\hbar}{m}}. \tag{2.18}$$

This is the so called standard quantum limit.

Thermal noise

The thermal noise is a fundamental noise present in all mechanic systems. It is defined as the fluctuation of a physical observable (position of the mirror surface, in our case) due to the microscopic nature of the ensemble that is in thermal equilibrium with the enviroment. The internal energy of a macroscopic apparatus, at thermal equilibrium, is shared between all its normal modes. The main calculation tool to estimate the thermal noise is the *Fluctuation − Dissipation Theorem* [13] that, for an harmonic oscillator, can be written:

$$\tilde{x}(\omega) = \sqrt{\frac{4K_B T \omega_0^2}{MQ\omega[(\omega^2 - \omega_0^2)^2 + \omega^4/Q^2]}}. \tag{2.19}$$

Where K_B is the Boltzmann's constant,T is the temperature, M is the mass, ω_0 is the resonant frequency,and $Q = \frac{\omega_0}{/}\Delta\omega$ is the quality factor, where $\Delta\omega$ is the width measured at half-hight of $\tilde{x}$.
In general in any system the total thermal noise is the sum of several contributions like that in equation (2.19). To reduce the thermal noise away from the resonant frequency, the usual strategy is to concentrate most of the thermal energy at the resonance by having an high quality factor Q. This depends on the materials and structures adopted to build up the mechanic system. An other way to reduce this noise is turning down the temperature until cryogenic levels. But this solution shows several technical difficulties.
For an interferometer with suspended mirrors the thermal noise is due to the energy loss processes of suspension wires and test masses. In particular the suspension wires contribute to the thermal noise through 3 processes:

- Pendulum thermal oscillation
- Vertical thermal oscillation

- Violin modes.

Dwell on the first contribute (For the other two suspension wire contributions see [14]). The pendula of the suspension have the resonance frequencies well below the detection bandwith ($\omega_0 << \omega_{GW}$), so the eq.(2.19) becomes:

$$\tilde{x}_{tp}(\omega) == \sqrt{\frac{4K_bT\omega_0}{MQ\omega^5}} \tag{2.20}$$

. Then Pendulum thermal noise decreases with increasing the frequency $\propto (\omega^{-5/2)})$, dominating at low frequency.
The test mass thermal noise is connected to internal vibrations of mirror and can be described as a set of oscillators corresponding to its normal modes. In this case the frequencies are of the order of several kHz, then above the detection bandwidth; so the eq.(2.19) becomes:

$$\tilde{x}_{tm}(\omega) = \sqrt{\sum_i \frac{4K_BT}{m_iQ_i\omega_i^3}} \tag{2.21}$$

where m_i is the effective mass of the mirror corresponding to the normal mode i with resonance frequency ω_i.
Finally, we can notice that, as for the seismic noise, being

$$h_{tn}(f) = \frac{2}{L_{arm}}\sqrt{< \tilde{x_{tn}} >^2}, \tag{2.22}$$

also for the thermal noise there is a decreasing (with L^{-1}) of the interferometer sensitivity independently by the use of any techniques of optical amplification of the signal (Fabry-Perot).

2.3.3 Technical and environmental noise

This type of noises cannot be forecasted with a general model because they are strictly linked to the detector site and to environmental conditions as well as working condition of the systems used to perform the interferometer control. The noise sources are very much, after that we will present only some of them, which analysis and reduction regards more strictly the present work.

2.4 A sofisticated interferometer: VIRGO

The gravitational wave interferometer VIRGO, supported by the french CNRS (Centre National de la Recherche Scientifique) and the italian INFN (Istituto Nazionale di Fisica Nucleare) is located at the European Gravitational Observatory (EGO), close to Cascina (Pisa, Italy). Virgo is designed to detect gravitational waves emitted by astrophysical sources in the frequency range from a few HZ to a few KHz. With spectral sensitivity h of about $10^{-23}\frac{1}{\sqrt{Hz}} - 3 \cdot 10^{-22}\frac{1}{\sqrt{Hz}}$ in the frequency range near 100 Hz. This corresponds, in terms of relative displacements of the test masses, to measure length variations of less than $10^{-19}\frac{m}{\sqrt{Hz}}$. It is important noting that the Virgo experiment is continuously in evolution and after the commissioning first phase the detector could be operated with a good stability close to the design. Consequently a first long science run (VSR1) took place in 2007 in coincidence and in collaboration with the runs of two LIGO detectors. Since then, a series of improvement are took place to further increase the sensitivity. Therefore the GWs detector, in the upgraded version Virgo+, started a longer science run (VSR2) in mid 2009 together with the LIGO S6 run. In parallel the Advanced Virgo detector is been designed, aiming at a sensitivity 10 times better than Virgo, in the full bandwidth. The construction phase is expected to start at mid 2011.

2.4.1 Optical lay-out

The actual optical layout of Virgo+ is shown in figure 2.2. This is a Michelson interferometer with arms replaced by 3 Km long resonant Fabry-Perot cavities with a finesse $F = 50$. The input TEM00 beam is generated by a laser with a power of 20 W and a wavelength of 1064nm. The beam jitter reduction is obtained by passing the input light through a 144m long input mode-cleaner cavity (IMC) that also cleans the higher transverse modes TEM_{lm}. The beam outgoing the injection system enters the interferometer (ITF) through the power-recycling mirror (PR). This mirror and the Michelson ITF form a Fabry- Perot cavity called power recycling cavity (PRC).
When the ITF is locked at its working point, the two beams are recombined to create a destructive interference at the main output port, called dark port.

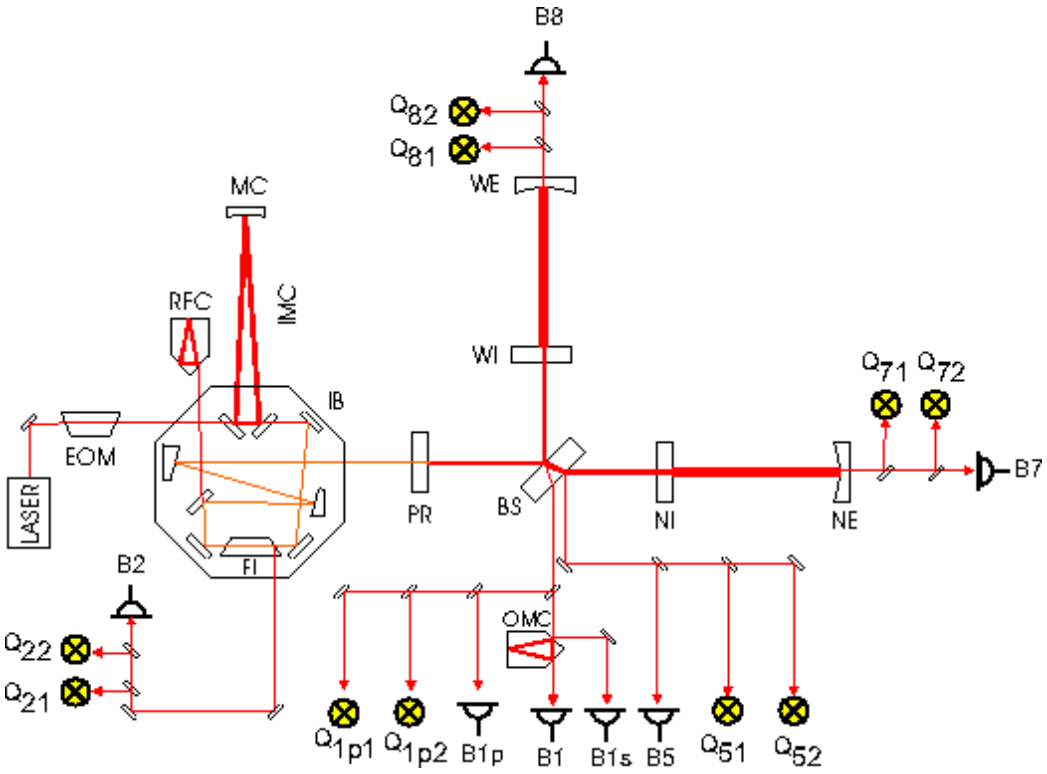

Figure 2.2: Simplified scheme optical lay-out of Virgo. The laser beam is passing the IMC cavity, then it is split at the BS in two Fabry Perot cavities (the North and West cavity). The ITF is locked to have a destructive interference at dark port, here the GW signal is detected with B1 photo-diodes B1 after having been filter by an output mode cleaner (OMC).

This is the dark fringe condition. In this condition most of light is reflected to the bright port, thus to enhance to power circulating in the interferometer the PR mirror reflected back again the light inside of the ITF. Finally the beam is filtered by the output mode-cleaner (OMC), then is detected by a set of InGaAS photodiodes (B1), by which the dark port signal is reconstructed. Other signals are extracted from the ITF, essentially for control purposes. Conventionally the sensors beginning with B are used for the longitudinal control and the ones starting with Q for the alignment control.

2.4.2 Injection system

The input of Virgo+ is a laser beam of 20 W power and 1064nm wavelength, generated by a system of master-slave laser show in fig.2.3 . The slave laser is an high power $Nd : YVO_4$ source locked to an high stability solid state Nd:YAG master laser. The light beam is modulated in phase by using two electro-optic modulators EOM2 (6MHz and 22MHz) and EOM3 (8MHz). The beam direction is controlled at the level of two benches placed in laser

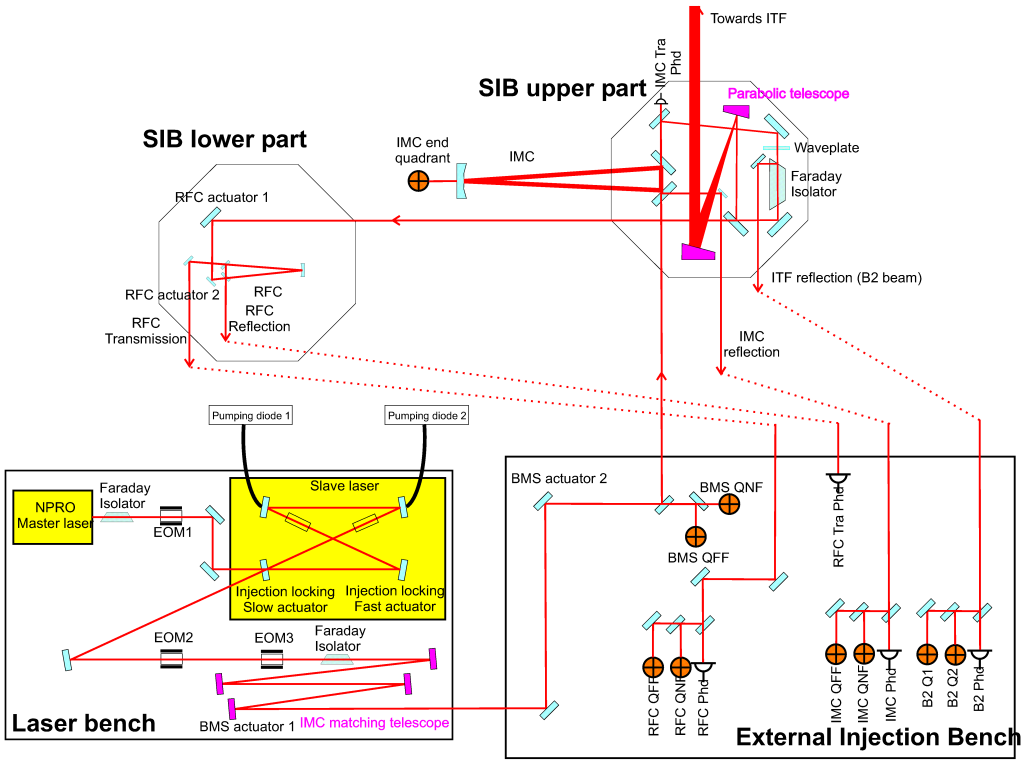

Figure 2.3: The injection system scheme. The beam of 20W and stabilized coming from the laser system, arrive on the suspended injection bench(SIB), where the Input Mode Cleaner (IMC) filter its transverse modes. Then pass trough a Faraday isolator and is sanded at the interferometer by a mode matching telescope.

laboratory, by the beam monitoring system (BMS). The beam can be translated and steered by two mirrors mounted on piezo-electric actuators. The

first mirror (upstream) is placed on the laser bench, while the second mirror (downstream) is mounted on the external injection bench, where several photodiodes are also placed and used to longitudinal control and quadrant photo-detectors for the angular control of interferometer. The laser system is placed on the laser bench, that is rigidly connected to ground and closed inside an acoustic isolation enclosures.

After the BMS system the beam is sent into the vacuum chamber to the suspended injection bench fig.2.3. On this bench there is a paricular optical component, the *dihedron* which togheter with a highly reflecting mirror form the Input Mode-Cleaner (IMC), a triangular cavity 144 m long with a finesse $F \sim\equiv 1000$. The role of this cavity is to filter the laser beam suppressing all transverse mode different from the fundamental Gaussian one. The IMC cavity is maintained on resonance for the carrier frequency using a Pound-Drever-Hall technique based on a 22 MHz demodulation of the IMC reflection see [15]. The 22 MHz sidebands are not resonant inside the input mode cleaner, while the carrier, the 6 MHz and the 8 MHz are trasmitted by this cavity.
The beam transmitted by IMC passes through a Faraday isolator (FI), this avoids the light reflected by the power recycling mirror to enter the IMC and interfere with its control, as well as with laser control system. The beam transmitted by the IMC is sent afterward to a telescope composed by the parabolic mirrors M5 and M6 wich mode matches the beam to the resonant mode of the power recycling cavity (PRC). Moreover, a small part of the FI transmission is sent through a periscope to the lower part of the bench to the $reference\ cavity$ RFC, a monolithic triangular cavity 30 cm long, which is used as a reference for frequency stabilization of the laser and it is part of the full interferometer longitudinal control.

2.4.3 Fabry Perot cavities as interfeometer arms

As we saw in the previous chapter the phase-difference induced by a gravitational wave at the output of the interferometer is proportional to its arms length, therefore the sensitivity has an intrinsic limit. Considering that is not technically easy to have arms longer than 3-4 km, a way to improve the

sensitivity of the detector, without changing the arms length, is to increase the optical path by implementing Fabry-Perot cavities in each interferometer arm (see fig.2.2). The two arm cavities are called north and west arm. The two mirrors composing each cavity are called input and end mirror.
The light, before recombining, is stored in the two cavities for a time proportional to their Finesse F. If the cavity is in resonance, the variation Δd of the cavity length produces a phase variation $\Delta\Phi$ on the reflected beam given by:

$$\Delta\Phi_{F.P.} = \frac{4\pi}{\lambda}\frac{2F}{\pi}\Delta d. \tag{2.23}$$

The phase-difference induced by a gravitational wave of frequency ω_{GW} at the output of a Michelson interferometer with FB cavity is:

$$\Delta\Phi_{F.P.} = \frac{4\pi}{\lambda}\frac{2F}{\pi}\frac{hL}{\sqrt{1+(\frac{2F}{\pi}\frac{\omega_{GW}L}{c})^2}} \tag{2.24}$$

. Therefore the effect is amplified by the presence of the factor F, that in the Virgo+ case is 50, but new mirrors allowing to achieve an higher cavity finesse will be installed in 2010. The mirrors used for cavities mirror are made of high quality fused silica, with a diameter of 35 cm and a mass of about 21 kg. The two NI and WI mirrors are flat, the two NE and WE are concave, with radius of curvature (ROC) of $\sim 1500m$.

2.4.4 Configuration of dark fringe and recycling of light

The GW interferometer works in the dark-fringe conditions, we see now the reason of this choice.
Remembering the (2.8):

$$\delta P_{out}(t) = \frac{P_{in}}{2}\frac{r_a + r_b}{2}Csin\alpha \cdot \delta\Phi_{GW}(t) \tag{2.25}$$

the best choice for the tuning of the interferometer seems the one that maximizes the sine in this equation, that corresponds to having half of the maximum power in the output port. This condition is usually called $gray\ fringe$. This should be true if there were no sources of noise limiting the ability to detect power fluctuations. In reality, as we know, there is a fundamental limitation to the accuracy of power measurements, given by the shot noise.

Therefore the best tuning for a Michelson interferometer is found maximizing the signal-to-noise ratio:

$$SNR(f) = \frac{1}{2}\sqrt{\frac{P_{in}}{h_p\nu}}\frac{Csin\alpha}{\sqrt{1+cos\alpha}}\frac{2\pi L}{\lambda}h(f) \tag{2.26}$$

having used the (2.14) and (2.5). The maximum of the SNR with respect to the static tuning α is

$$cos\alpha = \frac{-1+\sqrt{2(1-C^2)}}{C} \tag{2.27}$$

Since the contrast is close to 1, the best tuning of a Michelson interferometer is very close to the *dark fringe condition*. This technique is usually called DC detection.

In this condition the light is almost all reflected back toward the interferometer input. It is possible to use this light placing a mirror in front of the laser which reflects back again the light toward the interferometer . In practice, the recycling mirror and the whole interferometer form a cavity Fabry-Perot, called recycling cavity. If the cavity is in resonance with the input laser, the power inside the interferometer (that is the power on the beam-splitter) increases of a factor depending by the Finesse of this new cavity. Consequently, there is a decrease of the shot-noise limit and then an increase of phase sensitivity. The power increasing factor depends by the reflectivity of the recycling mirror and the reflectivity of the interferometer:

$$P_0^r = P_0\frac{t_r^2}{(1-r_r r_{ITF}})^2 = P_0 G_r \tag{2.28}$$

where r_r and t_r are respectively the reflectivity and the transmissivity of the recycling mirror, while r_{ITF} is the reflectivity of the interferometer and G_r is called recycling gain. r_{ITF} represents the fraction of light incident upon the beam-splitter which is reflected back toward the laser when the interferometer is in dark-fringe conditions.

The power recycling mirror is made, as the cavity mirror, of high quality fused silica, with a diameter of 35 cm and a mass of about 21 kg, and its reflectivity a @1064nm is such that the recycling gain G_r is about 40.

2.4.5 Suspension system

The main optical components of the interferometer are suspended by a sophisticated seismic isolation system: the Superattenuator (SA), see fig.2.4, and located in an ultra-high vacuum system. The SA is a multistage pendular suspension ~ 7 m high, which isolates the test masses from the ground motion as mentioned in section 2.3.1. The reduction of the seismic noise is performed for frequency higher than a few Hz (the pendulum longitudinal resonance frequency are all confined below 2.5 Hz) and the passive attenuation of the whole chain is better than 10^{-14} at 10 Hz, corresponding to an expected residual mirror motion of $10^{-18} m/\sqrt{Hz}$ at the same frequency [16]. The first stage of the SA is an inverted pendulum (IP) [17] formed by three legs that sustain the top stage (filter 0) of the entire suspension chain. If we considere the IP as a bar of length l and stiffness k which supports a mass M, the elasticity of the leg joints, combined with the opposite effect of the gravitational force (acting as an anti-spring) gives a system with a resonance ω_0 at about 40 mHz:

$$\omega_0 = \sqrt{\frac{k}{M} - \frac{g}{l}}. \tag{2.29}$$

The IP is used as pre-isolation stage to reduce the seismic motion at very low frequency, of the top suspension point.
Then a chain of five mechanical filters is suspended from the filter 0. From the last stage of the chain, the filter 7, the so called marionetta is suspended by a steel wire. Suspended to the marionette there is the payload system composed by the test mass (mirror) and by an aluminum reference mass (RM), independently suspended behind the mirror. Both the mirror and the reference mass are separately suspended to the marionette by four wires each.
The vertical attenuation is obtained using a star of triangular pre-bended blades of metal on the bottom of each stage (see.fig.2.4). The resonant frequency of this system would however be too high, due to the stiffness of the metal to support the weight of the entire suspension. They are therefore combined with two sets of magnets in repulsive configuration. They form a magnetic anti-spring [18] that combined with the blades gives a low resonant frequency, comparable to the horizontal modes ones.

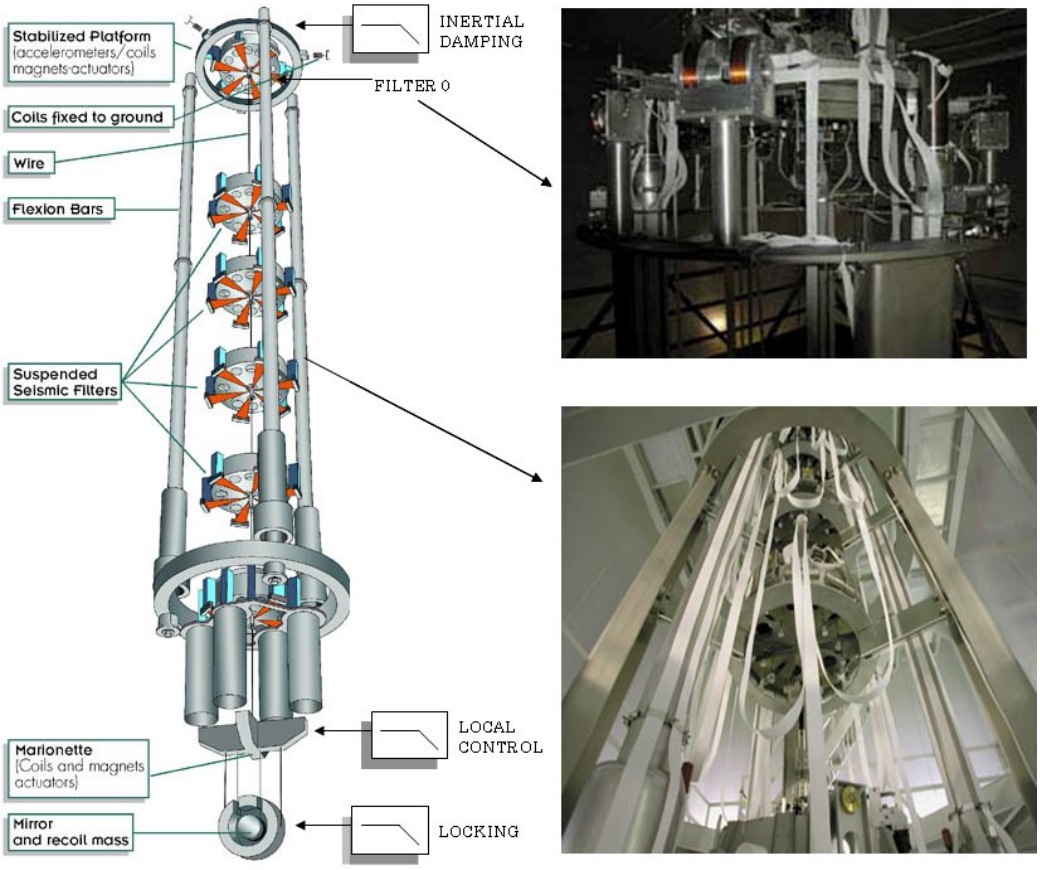

Figure 2.4: The superattenuator (SA)

Damping Control

The test mass suspension of the VIRGO detector (the SA) has been designed in order to suppress seismic noise below the thermal noise level above 2.5 Hz. At lower frequencies, in the range of the normal modes of the SA (0.042 Hz), the residual motion of the mirror is much larger (tens of microns) and it can saturate the interferometer control system. This motion is reduced by implementing a wideband multidimensional active control (the so-called inertial damping [17]) which makes use of both accelerometers and position sensors (LVDT). All signals are acquired by analog-to-digital converters (ADC) and processed by custom digital-signal-processors (DSP). Feedback forces are exerted by coilmagnet actuation system on the top of the inverted pendulum pre-isolator stage fig. 2.5.

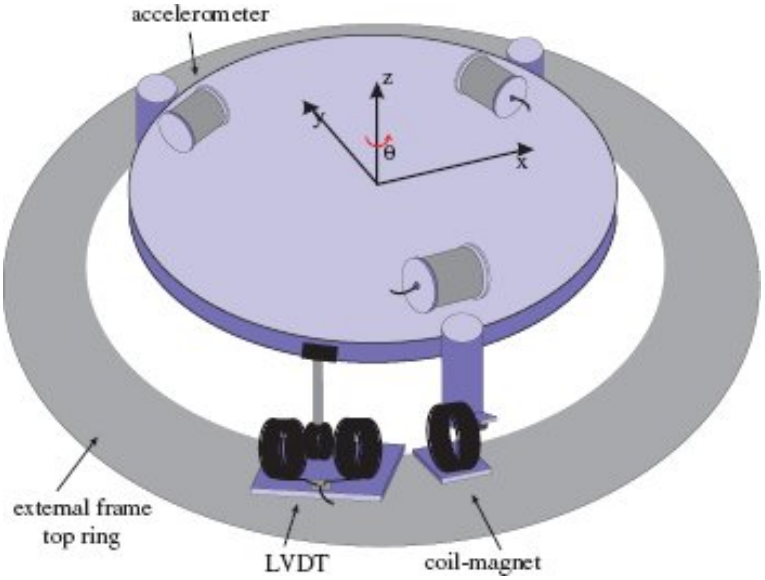

Figure 2.5: simplified view of the IP top table, provided with the three accelerometers. One LVDT position sensor and one coilmagnet actuator are also shown. The X, Y, Θ normal modes of the IP correspond approximately to translations along the $\hat{x}$ and $\hat{y}$ axes and rotation around the $\hat{z}$ axis.

Local Control

The local control [19] of the mirror can be made both acting at the mirror or at the marionetta level. Four magnets are glued to the back face of each mirror, in correspondence of four coils attached to the reference mass. By controlling the current flowing through these coils it is possible to apply longitudinal and torsional forces to the mirror. Four other magnets are attached to the marionette, in correspondence to coils that, suspended through cylindrical bars coming down from the filter 7, exert a force on the marionetta. The error signals for the local control systems are obtained using optical levers devices, composed by low power red laser diodes and position sensing detector(PSD) photo-detectors (see fig2.6).

These optical levers are used to measure the angular and longitudinal displacement of the mirror (see chapter 4) and the angular one of the marionette, using a small mirror attached to it. When the motion is too large for the dynamical range of the PSD sensors, the rough position is reconstructed

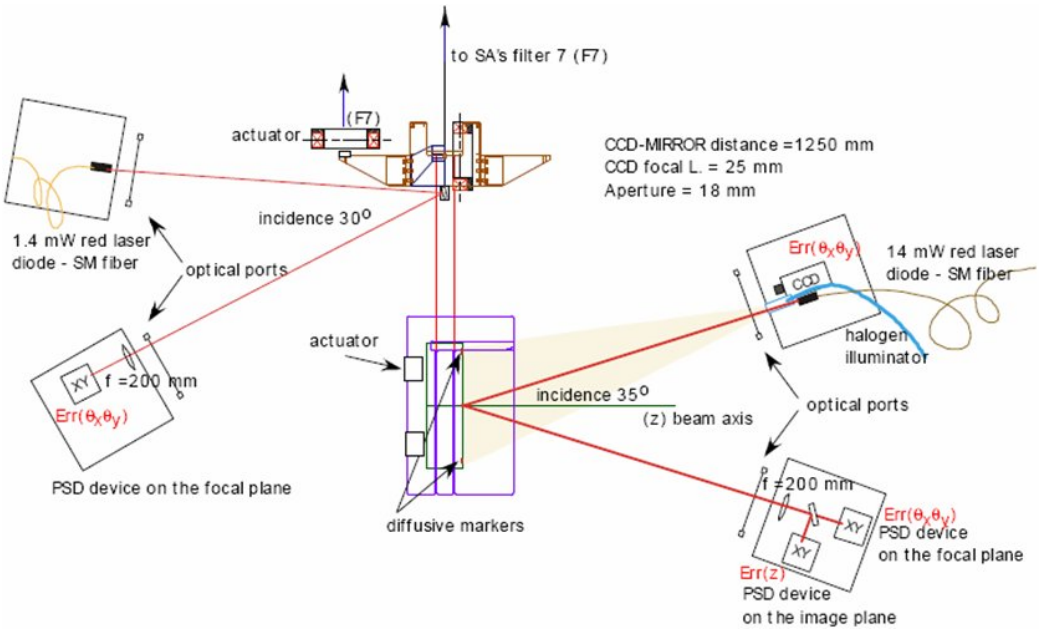

Figure 2.6: The local control system. The optical level divices of Virgo use red laser diodes to control the position of the marionette and the reference mass.

using a CCD camera which looks at diffusive markers attached to the mirror itself. All local control signals, for each mirror, are acquired by ADC boards and processed by a dedicated DSP. This system also receives global interferometric signals for the longitudinal and angular sensing and control (section 2.4.6).

2.4.6 Global Control

After the pre-alignment made by using the local control system, the interferometer need to be locked at its working point. This means that the laser beam is in resonance with the Fabry-Perot and recycling cavities and the main output port is on the dark fringe. These conditions can be achieved by fixing relationships between the laser wavelength and four independent lengths of the interferometer [20]:

- $DARM = L_x - L_y$

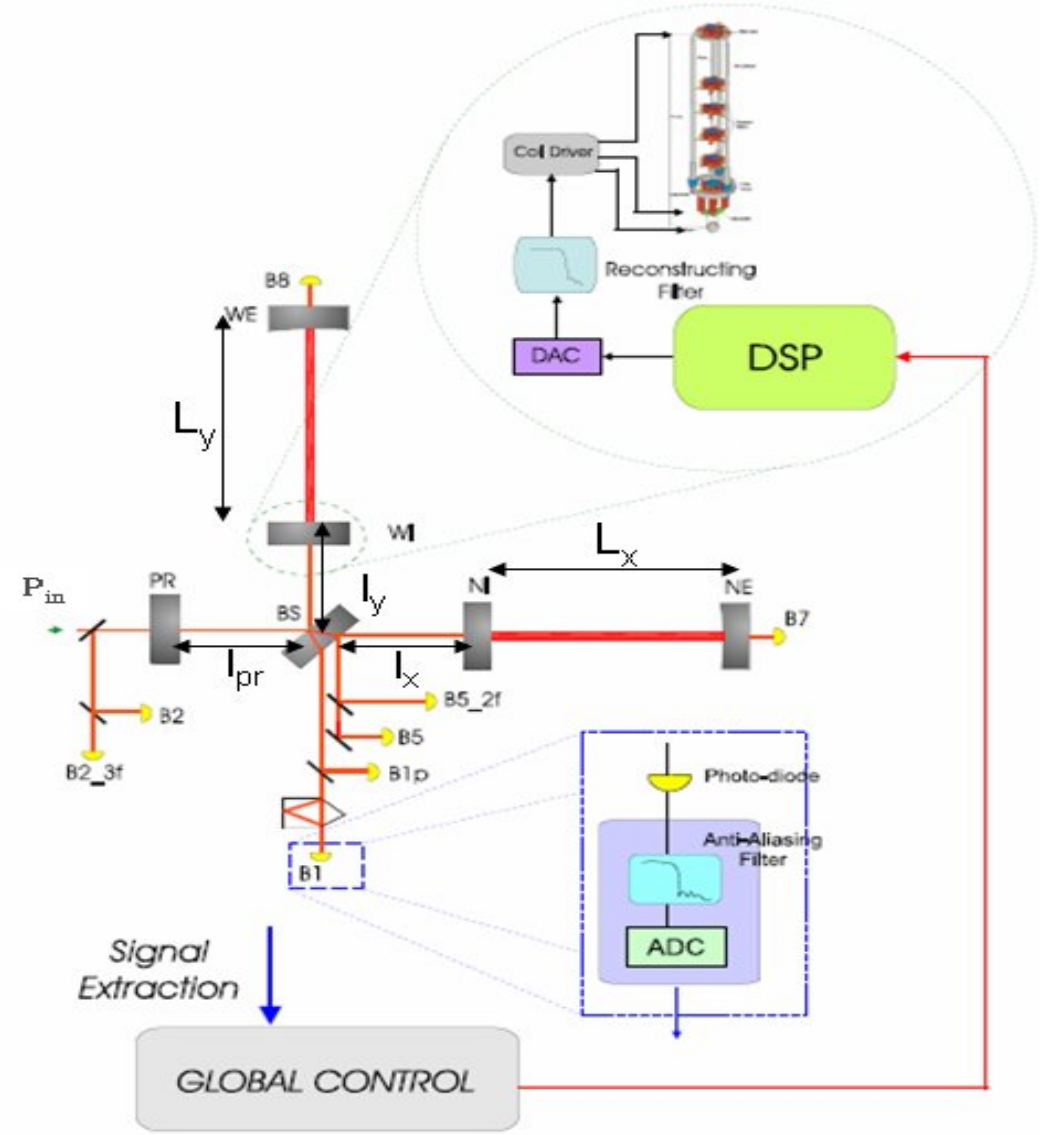

Figure 2.7: Longitudinal control chain. Signals extracted from the ITF by photodiodes are sent to the Global Control, which combines them in order to compute corrections, which are sent to the DSP of the involved suspensions. The lengths of the Fabry-Perot cavities L_x and L_y are $\sim$ 3 Km wile the lengths in the central interferometer l_x, l_y and l_pr are $\sim 6m$

- $CARM = L_x + L_y$
- $PRCL = l_{pr} + \frac{l_x + l_y}{2}$

- $MICH = l_x - l_y$

Where (see fig. 2.8) DARM is the differential arm length, CARM is the common arm length, PRCL is the recycling cavity length and the MICH is the Michelson length degreeof freedom. These four lengths have to be controlled with a very high accuracy (typical rms of $10^-12 - 10^-10m$). The longitudinal control is performed by using the Pound-Drever-Hall technique, being the input beam modulated at 6.26 MHz. All the four lengths can be reconstructed by mixing the signals coming from photodiodes placed at different output ports of the interferometer. The photodiode signals are digitized and sent, via optical links, to the global control system [21] that computes, at a 10 kHz sampling rate, the correction signals to be sent to the reference mass coils, converted to an analog signal by the DAC of the suspension electronics (fig.2.8).

When this control is engaged the active swing reduction makes smaller the compensation force to be applied at the mirror level to maintain the interferometer locked. This allows to reduce the electronic noise induced by the driving system of the coil used for the test mass control.

Indeed this noise is proportional to the range of the force made available at the mirror level. For the same reason the large (hundreds of microns) drifts of the mirror (between DC and a few tens of mHz) are compensated by acting to the suspension top stage (Tidal control). The induced control DAC noise at the top stage is filtered by the suspension chain below. Once the tidal control is implemented, the mirror residual displacement is around 1 μm peak to peak and occurs mainly between tens of mHz and a few Hz. This displacement is compensated acting on the marionette so that the DAC noise is filtered by the last pendula stage. Using this hierarchical control, only nanometer displacements (above a few Hz) are compensated by acting directly at mirror level (from the reference mass coils). The reduction of the reference mass force range makes the DAC noise, in the VIRGO dtection band, smaller than the other noise contributions limiting the antenna sensitivity.

Once the interferometer is longitudinally locked it is necessary to maintain the mirrors aligned each other and with respect to the incoming beam.

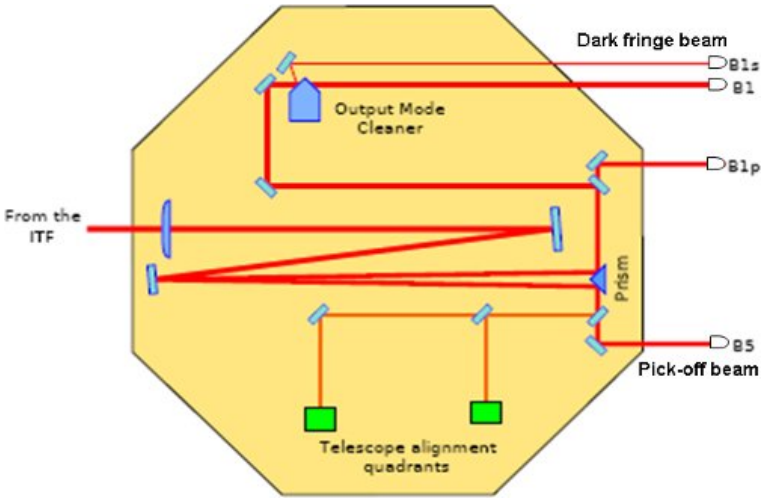

Figure 2.8: Schematic drawing of the suspended and external detection system. The dark fringe beam pass trough the output mode-cleaner(OMC) a monolithic cavity with finesse 50 and length of 3 cm, and then detected by B1 detectors, while the detector B1p take 1% of transmission of the BS before the OMC and it is used for angular and longitudinal control. On the B5 detector impinges the second reflection from the AR coating of BS of the Michelson (pick-off beam). The pick-off beam is used to monitor the beams shape and position and as well as to obtain error signals for the telescope alignment.

The required accuracy (rms close to $10^{-}9$ rad), not achievable by the ground-based mirror local control, can be reached by the Anderson-Giordano technique [22]. The laser phase-modulation frequency is chosen so that the sidebands of the first order optical transverse mode (TEM01) are resonant in the arm cavities. The light transmitted by the cavities is detected by quadrant photodiodes and a set of signals proportional to the mirror misalignments, are generated. The error signals are received by the global control that computes the feedback correction signals sent to the marionette coil-magnet actuators. This is done with a control bandwidth of a few Hz in order to avoid the injection of noise in the VIRGO band.

Finally it is interesting to note that while the very low frequency component is actued by the inertial damping, the intermediate frequency component is actuated on the marionette and only the high frequency one is sent to the

reference mass coils.

2.4.7 Thermal compensation system (TCS)

One of the main upgrades of Virgo+ respect to Virgo is to increase the input laser power from 8 to 25 Watt: commissioning efforts are related to compensate the thermo-optic effects caused by the spurious absorption of the high power beams. by the mirrors.

The biggest problem caused by the increase of power is the thermal lensing in the input mirrors of the long Fabry-Perot cavities, which prevents the achieving of a stable lock of the interferometer. To solve this problem, it was implemented a Thermal Compensation System (TCS), which consist in 2 CO_2 lasers (one for each input bench) that can heat the coating input mirrors with a suitable pattern. A similar solution was implemented at LIGO a pair of years ago. In particular the positive thermal lens caused by the main YAG laser can be compensated with the CO_2 laser by illuminating with an annulus-shaped pattern around the main beam. A second beam also originating by the source CO_2 laser, which has a similar size as the YAG beam, can be switched on when the interferometer unlocks. This solution keeps the mirrors in the same thermal condition, allowing for a fast relock of the interferometer. The installation of the system was recently completed. More commissioning time will be required for the fully optimization the system.

2.4.8 Virgo+ Sensitivity

The Virgo+ experiment is expected to reach its design sensitivity in a near future. In particular monolithic suspensions will be soon implemented in order to reduce the wire thermal noise, when the steel wires will be substituted with fused silica wires joint to mass using the silicate bonding technique [25]. In figure 2.9 the expected Virgo+ sensitivity is reported Virgo+ configuration with monolithic suspensions, 25 W laser power after IMC, finesse of 150 and recycling gain equal to 20 [26].

Presently Virgo+ at present time is in science run it did not reach the full design sensitivity yet. In the figure 2.10 is shown the last improvements of the Virgo+ sensitivity [14]. It is important to remember that the monolithic suspensions was not implemented yet.

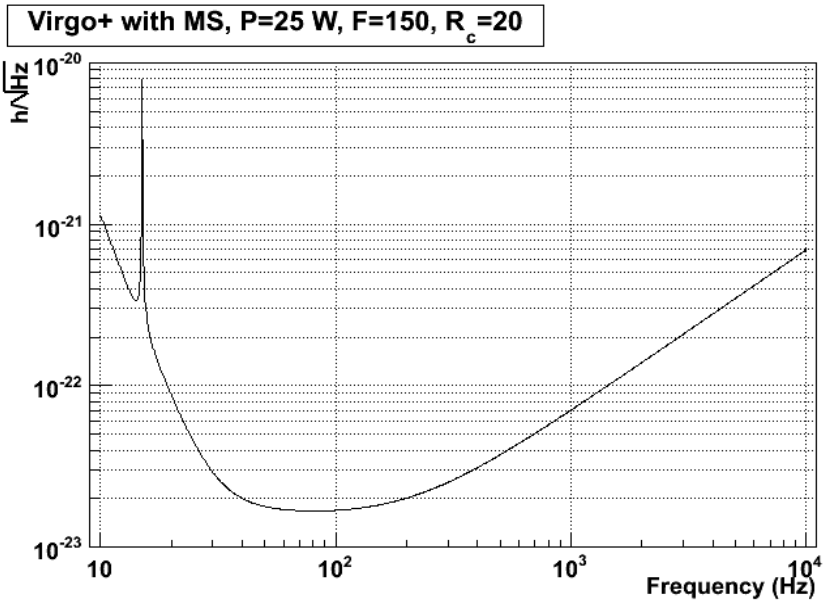

Figure 2.9: Virgo+ design sensitivity

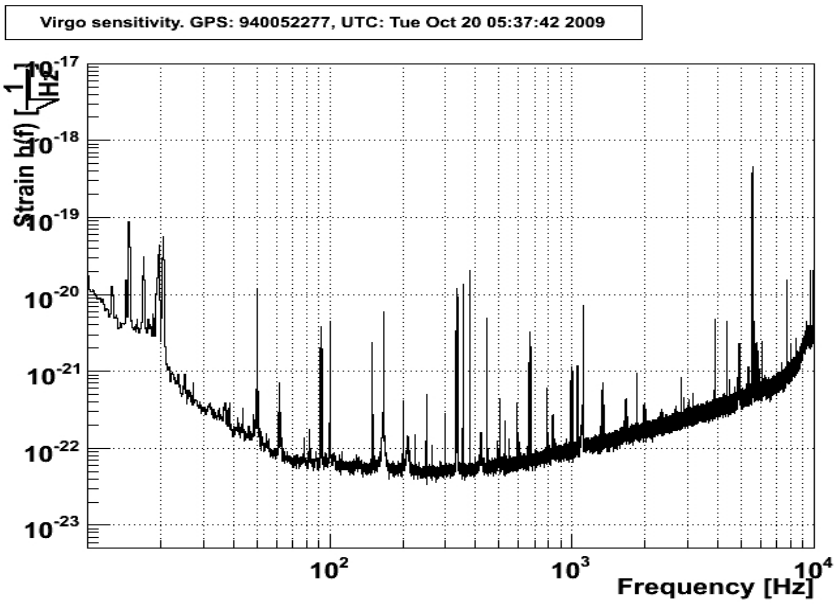

[h!]

Figure 2.10: Virgo+ sensitivity measured at October 2009

2.5 Advanced Virgo

Advanced Virgo (AdV) is the project that aims to upgrade the Virgo detector to a second generation detector, that will give us the chance to open new window on the universe. AdV will be able to scan a 1000 times larger volume of the Universe than initial Virgo. Even it will be hosted in the same infrastructures as Virgo, the AdV sensitivity will be better by one order of magnitude over most of the detection band. The target of this section is to give a summary of the design features of AdV describing briefly the upgrades necessary to convert the initial Virgo instrument to the AdV detector [27].

Interferometer optical configuration

AdV will be a dual recycled interferometer [6] (see fig2.11).

Beside the standard power recycling, a signal recycling (SR) cavity will be implemented. The tuning of the SR parameters allows to change the shape of the sensitivity curve, optimizing the detector for a given astrophysical source. The recycling cavities are designed to be non resonant for higher order optical modes (non degenerate recycling cavities, NDRC). This design is expected to greatly reduce the interferometer sensitivity to misalignments and thermal effects. The coating thermal noise limits the AdV sensitivity in the mid-frequency range. One way to lower its level is to enlarge the spot size on the test masses. Therefore, unlike Virgo, the beam waist will be placed closed to the center of the 3 km Fabry- Perot cavities, resulting in beam radii of 56mm and 65mm for the input and end mirrors, respectively.

Laser

More laser power is needed to improve the sensitivity at high frequency, where the detector is shot noise limited. The AdV laser will provide a power of about 200 W, the ideal candidate should be a fiber laser, but this is a topic of discussion yet. One will develop appropriate power and frequency control, as well as polarization and beam jitter control. New optical material and new technology have to be used compatibly with a so high power (see chapter 3).

Injection system

The input optics for AdV must be compliant with the 10 times increased optical power. Proper electro-optic modulators and Faraday isolators are being developed (see chapter 3). The Virgo configuration for the input mode cleaner (144m long triangular cavity) will be kept. The suspended injection bench will host two mirrors of the power recycling cavity.

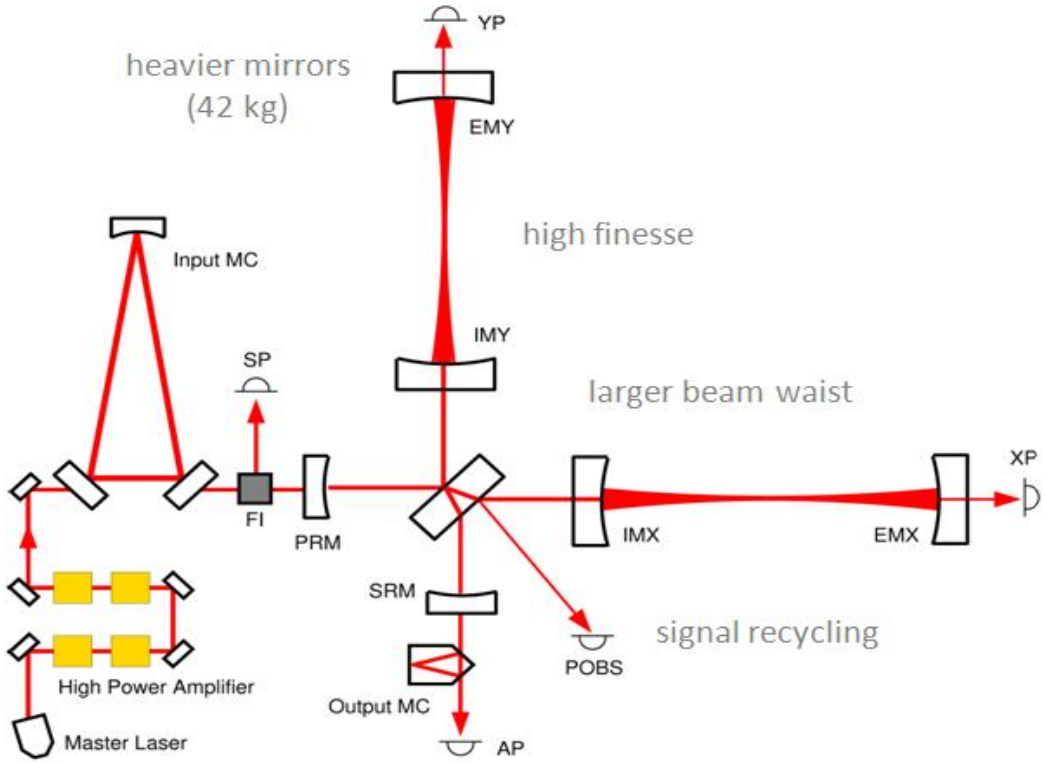

Figure 2.11: Advanced Virgo baseline

Mirror

Given the much larger optical power in the cavities, radiation pressure noise becomes a limit in the low frequency range and heavier test masses are needed to reduce it. The mirrors designed for AdV have the same diameter as the Virgo ones (35 cm) but are twice as thick (20 cm) and heavy (42 kg). A large $R\&D$ effort is being carried out in the GW community to produce coatings

with lower mechanical losses (an thus less thermal noise). The coating of the AdV mirrors is expected to start in mid 2010.

Detection

AdV will use a DC detection scheme, which improves the quantum noise and eliminates some technical noises (such as RF phase noise) which would be limiting the detector sensitivity in case of heterodyne readout. The main photodiodes will be placed on the suspended detection bench (in vacuum) to improve the rejection of seismic and acoustic noise. The detection bench will host the Signal Recycling mirror and one of the folding mirrors of the non-degenerate signal recycling cavity.

Interferometer sensing and control

An extended variable finesse technique [28], successfully tested in Virgo, will be used to achieve the full lock. The reference solution for the lock of the high finesse Fabry-Perot cavities foresees an auxiliary laser with different wavelength, for which the arm cavity finesse is much reduced. [29] Possible sets of modulation frequencies and cavity lengths have already been defined.

Vibration isolation and mirror suspensions

The seismic attenuation provided by the Virgo superattenuator (SA) is already compliant with the AdV sensitivity. The only important upgrade planned is the implementation of a tilt control at the base of the inverted pendulum: this will allow to control the inertial platform in 6 degrees of freedom, increasing the detector robustness in windy days [27]. The lower part of the SA will be modified to be compliant with the thicker and heavier mirrors. To reduce the pendulum thermal noise, the AdV test masses will be suspended by fused silica fibers as in Virgo+.

Vacuum

The current Virgo vacuum level needs to be improved by a factor of about 100 in order to be compliant with the AdV sensitivity. Such improvement requires to bake out the pipes. In the current configuration this can be done only if the

towers are baked as well, which has several drawbacks. Therefore, the use of cryotraps separating the 3 km tubes from the towers was proposed for AdV. Vacuum links with a larger diameter are needed in the central area, to allow for the larger size of laser beam and for the folded path in the non-degenerate recycling cavities. The links will have also different lengths to meet the new requirements on the position of the towers set by the interferometric sensing and control subsystem.

Infrastructure

To reduce the influence of anthropogenic disturbances most of the noisy machines will be either replaced with more silent ones, seismically and acoustically isolated or moved out of the experimental halls.

2.5.1 AdV Sensitivity

The design AdV sensitivity was computed [30] taking into account the main noise contributions (see fig 2.12). The SR (signal recycling) parameters to compute it have been chosen in order to maximize the sight distance for Binary Neutron Stars (BNS) .
With this choice, the inspiral ranges are about 150 Mpc for BNS and 1.1 Gpc for Binary Black Holes (BBH) [30].
In fact the presence of the SR cavity allows to think of AdV as a tuneable detector: the sensitivity curve can be shaped in order to optimize it for targeting different astrophysical sources. The SR mirror transmittance influences the detector bandwidth, while the microscopic lenght of the SR cavity changes the frequency of the maximum sensitivity.

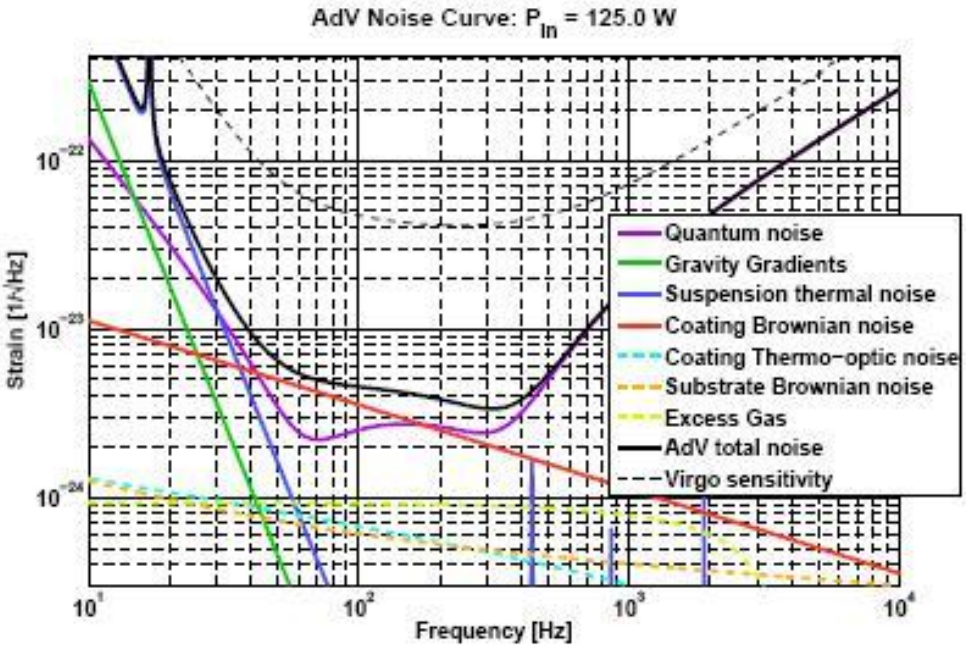

Figure 2.12: Reference AdV sensitivity and expected noise contributions.

Chapter 3

High power thermal effects in Faraday isolator for AdV

Advanced Virgo will work with an input laser power of the 200 W, in order to reduce the shot-noise as described above. In this chapter the thermal effects induced by absorption of laser radiation in of the injection optics bulk. While are described the thermal compensation (TCS) effects due by the coating input mirrors was already implemented in Virgo+, the thermal effects due by absorbtion in injection system is still under investigation. This is the principal subject of the *R&D* project for AdV: `"High power input optical components for Advanced Virgo"`. We expect that, by using an high power laser (HP), these thermal effects will significantly limit the working AdV right conditions interferometer, because it will add a not negligible technical noise . Already in Virgo+, with 20 W power, similar problems was encountered some these problems. We have analyzed the thermal effect in the main optical elements that we be will used in AdV injection systems. In particular the Faraday isolator is more strongly affected by thermal effect. In fact his core is a TGG crystal, a magneto-optical media that presents a not neglgeble absorbtion. Here the thermal effects in TGG are investigated in depth.

3.1 Injection system of advanced Virgo

The Injection system (INJ) of AdV (fig.3.1) consists in all optics downstream of the high power laser and before of the interferometer core (ITF).

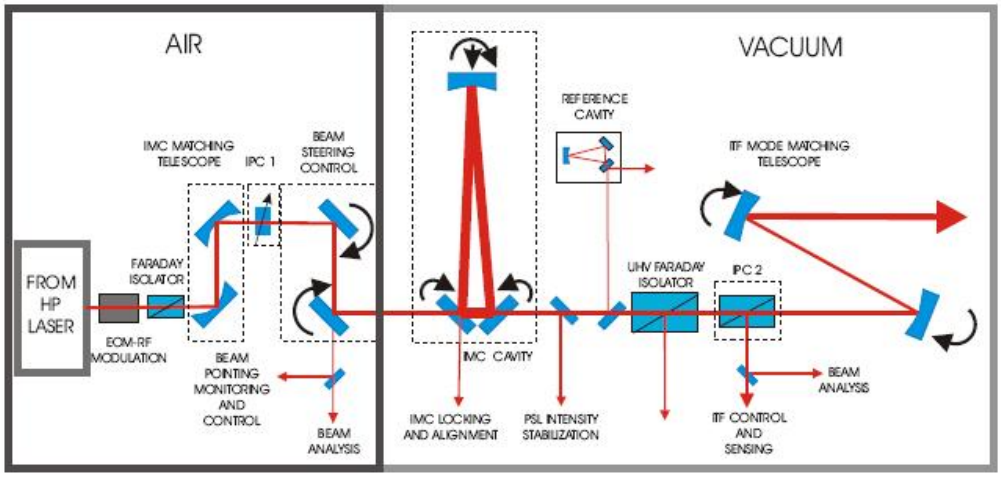

Figure 3.1: Schematic of the possible INJ system of AdV

An Electro-Optic Modulation (EOM) will provide the needed RF phase modulation (for control purposes). A power adjustment system, consisting of a half wave-plate and a polarizer will be used in order to tune ITF input power. A matching and steering system in air will be used to couple the beam into the in-vacuum suspended input mode cleaner (IMC). The resonant IMC which length is locked on the reference cavity (RFC), will also serve as first stage of frequency pre-stabilization. After the IMC an intensity stabilization section will provide the signal for stabilizing the laser RIN (relative intensity noise) and reach INJ requirements. An in-vacuum Faraday isolator will prevent interaction of the ITF reflected light with the IMC and laser system, avoiding serious problems with the control. Finally, an ITF mode matching telescope will give to the beam the correct dimension and shaping for matching with the interferometer. The requirements for the beam caming out from the INJ system are: transmission to the ITF $> 70\%$ (125 W), non-TEM00 power $< 5\%$, intensity noise $< 2 \times 10^{-9}/\sqrt{Hz}$ at $10Hz$, and beam Jitter $< 10^{-9} rad/\sqrt{Hz}$ ($f > 100Hz$).

In all these components, the high power will introduce thermally induced lensing and birefringence effects, together with other potential unexpected problems. We are measuring and studying all these effects to propose strategies of compensations. In LIGO the tests on input optics components have

not been performed with input power larger than 100 W, so the measurements to be performed in Virgo will give additional information. The tests actually going on are taking advantage from the LIGO experience in order to design components for the specific needs of AdV.

3.2 Faraday isolator for high power laser

Light back reflected by the ITF towards the IMC has already been an issue in Virgo. This problem will be more significant with the higher power of AdV. The solution for this problem has been the use of an in-vacuum Faraday isolator placed between the IMC and the ITF. Either in the case in which a suspended IMC or a fiber IMC will be used, the in-vacuum Faraday isolator between the interferometer and the IMC will be necessary. A Faraday isolator (FI) is a device largely used in laser applications, in order to protect laser oscillators from optical feedback. When we use very high power laser as in the next generation of GWs detector cases (advanced Virgo and LIGO), the problem becomes very important, because commercially FIs are not available for so high power. Therefore they are subject of research to satisfy the strong requirements imposed by stabilization in frequency and intensity of beam laser to reach the advanced detectors sensitivity target.

A Faraday Isolator is a unidirectional device based on the Faraday effect (see Appendix B). A Faraday Rotators is a magnet-optic medium with high damage threshold that produce a uniform 45° polarization rotation when a magnetic field is applied $\overrightarrow{\mathbf{B}}$. The amount of polarization rotation is

$$\theta = nV(T)\vec{\mathbf{L}} \cdot \vec{\mathbf{B}} \tag{3.1}$$

, where n is refractive index, V the Verdet constant (dependent on temperature T), L the crystal length and B the longitudinal magnetic field applied, to the crystal. When a Faraday rotator is placed between properly aligned polarizers the back reflection is stopped by first polarizer and we obtain a optical diode, see fig. 3.2. The magnetoptic medium is generally a TGG (Terbium Garnet Gallium) with cylindrical geometry . Virgo experience shows

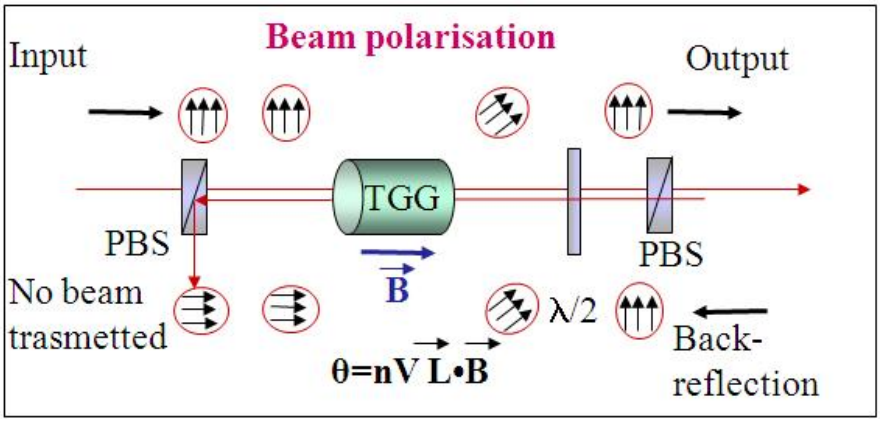

Figure 3.2: Faraday isolator. The FI works as a optical diode: the input beam pass trough the device maintaining his polarization, but the back-reflection beam rotate of $\frac{\pi}{2}$ his polarization and is stopped by first polarizer.

that a lack of optical isolation (less than 20 dB) makes the locking acquisition of the recycling cavity difficult or impossible, and some visible effects on the low frequency ITF alignment start to be visible. It is generally agreed that in the next interferometers an isolation better than 40 dB should be provided, even in view of the fact that experienced degradation of the isolation with the change of power and when going from air to vacuum have been observed. A design already that will be already adopted in Enhanced LIGO was propose for AdV. The prototype exhibits an optimal optical isolation, exceeding 49 dB, at more than 100 W input laser power. However, simulations of thermo-optical effects in TGG show that the isolation ratio changes when going from air to vacuum, depending on the laser power going through the Faraday crystal. In order to optimize the optical isolation, a remote tuning will be necessary. Here we present an analysis of thermal effects induced in TGG crystal that confirm this promising right working of proposed design and supply new tools to optimize this one.

When we have a strong absorption of laser radiation in magneto-optical material it will be present a radial temperature gradient $\frac{dT}{dr}$, (where r is the distance from the center $r = 0$) and an increasing of mean temperature T. We can observe three not negligible thermal effect that modified the optical characteristics of the output laser beam:

- Induced birefringence by photo-elastic effect of thermal strain with radial symmetry. The thermal strain limits the isolation ratio and cause problem to control systems. In fact this generate a mode conversion and an apparent depolarization of beam. This effect was studied in depth in this work. A careful analysis allowed as to explain its physic origin, in particular we observed a spin-orbital angular momentum conversion (STOC) in the photons of beam.

- Strong Thermal lensing due the radial temperature gradient. This effect generate a mismatch of beam with ITF cavities. The mismatch change with power laser causing problems in the control of the interferometer.

- Variation of Verdet constant on the temperature and consequently rotation of polarization angle beam's. We already had solved this problem for Virgo+, compensating it with a motorized half-plate.

3.2.1 Photo-elastic effect by radial thermal gradient and induced birefringence

We consider the case of an infinite cylindrical medium (in the our case is a TGG crystal, but the following discussion can be made for any isotropic medium). We shall neglect bound effects and we will consider a laser that impinges on the TGG crystal . We are interested, for the moment, only at radial temperature variation, therefore we have to solve the one-dimensional conduction equation, neglecting also the head radiation and convection that given a small contribution to temperature gradient:

$$\frac{1}{r}\frac{d}{dr}\big(r\frac{dT}{dr}\big) = -\frac{h(r)}{k} \tag{3.2}$$

where T is the temperature, r the radial coordinate, h the internal heat generation rate, k the thermal conductivity (only for isotropic or cubic crystal it is independent from the direction). In the case of TEM00 beam we have: $h(r) = \frac{\alpha P_{in}}{\pi r_0^2} e^{-\frac{r^2}{r_0^2}}$ where α is the absorbtion coefficient, P_{in} the input power impinging on the crystal, and r_0 is the beam waist. Integrating the (3.2) we

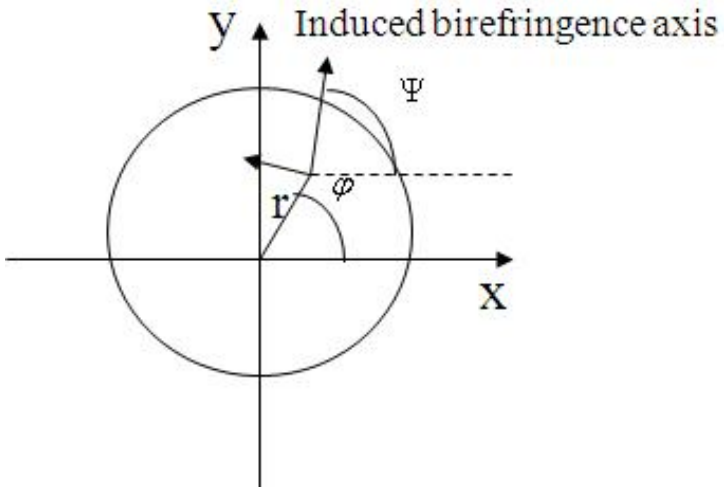

Figure 3.3: The radial temperature gradient induced a stress in the crystal in a direction Ψ dependent on orientation of crystal. In [1 1 1] oriented crystal o in homogenous medium $\Psi = \phi$.

obtain the temperature gradient:

$$\frac{dT}{dr} = -\frac{\alpha P_{in}}{2\pi k}\frac{(1 - e^{-r^2/r_0^2})}{r} \tag{3.3}$$

The temperature gradient generates mechanical stress in the medium, since the hotter inside area is constrained from expansion by the cooler outer zone (see fig.3.3).

The thermal strains ϵ_i^T with $i = r, \phi, z$ depend upon the elastic strains ϵ_i^E:

$$\epsilon_T = \epsilon_E + \alpha^* T \tag{3.4}$$

where α^* is the thermal expansion coefficient.
The thermal strains produce refractive index variations via the photo-elastic effect. As it is know [31] the refractive index of a medium is specified by the indicatrix, that for a cubic crystal is a sphere (see Appendix B). Under stress the indicatrix becomes an ellipsoid. If the crystal is [1 1 1] oriented, the transverse stresses are in radial and tangential direction, the local indicatrix also orients its axis in these directions (see fig.3.4), then there will be a variation of refractive index Δn_r and Δn_ϕ dependent by thermal gradient.

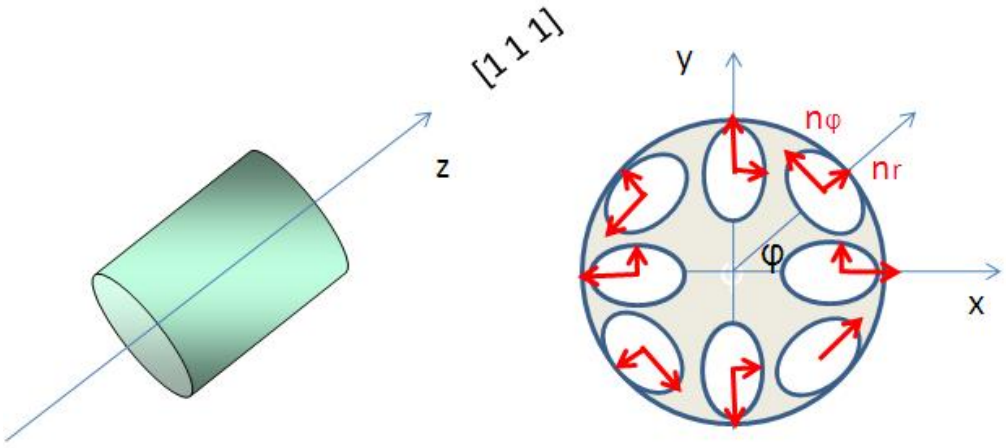

Figure 3.4: The induced birefringence modifie locally the indicatrix

We assume that the incident beam E_{in} is linearly polarized, it will be resolved into two component, one parallel to n_r and the other parallel to n_ϕ. Since $\Delta n_r \neq \Delta n_\phi$, there will be a phase difference between the two components and the light will emerge elliptically polarized. This will occur differently for all points of the crystal with exception for points located along x and y axes. In these points the radiation will see only n_ϕ along y and n_r along x, therefore we will observe only a shift delay.

3.2.2 Power loss in input polarization

In the previous section we showed that a local variation of indicatrix exist that produces an apparent depolarization of light. To evaluate the polarization of $\mathbf{E}_{out}$ we use the Jons matrix formalism. Let us a consider a TEM00 beam with linear polarization $\mathbf{E}_{in}$ impinging on the TGG

$$\mathbf{E}_{in} = \begin{pmatrix} \cos\theta \\ \sin\theta \end{pmatrix} \tag{3.5}$$

where θ is the polarization angle of the incident beam respect to the x crystal axis. After the crystal the fraction of energy in $\mathbf{E}_{out}$ field that remains in the original polarization can be calculated as:

$$\chi = \frac{|\mathbf{E}_{out}\mathbf{E}_{in}|^2}{|\mathbf{E}_{out}|^2 \cdot |\mathbf{E}_0|^2}. \tag{3.6}$$

Where

$$\mathbf{E}_{out} = F(\mathbf{r}, \Psi)\mathbf{E}_{in}. \tag{3.7}$$

We stress that the Jones matrix $F(\mathbf{r}, \Psi)$ is depend on $\mathbf{r}$ and on Φ (the angle

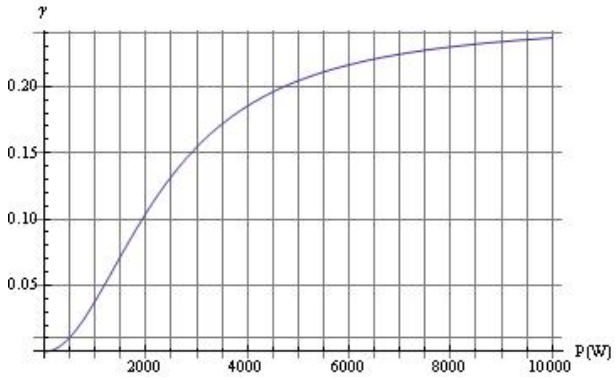

Figure 3.5: Rate of conversion γ in function on input power, with $\alpha = 1600ppm$ and $L = 8mm$

between the linear eigenpolarization and x axis, for a generic orientation of the crystal) see fig. 3.3, in fact as said above, the birefringence is locally different. $F(\mathbf{r}, \Psi)$ can be calculated as

$$F(\mathbf{r}, \Psi) = M(-\Psi)F_{xy}M(\Psi) = \sin\frac{\delta}{2} \cdot \begin{pmatrix} \cot\frac{\delta}{2} - i\cos 2\Psi & -i\sin 2\Psi \\ -i\sin 2\Psi & \cot\frac{\delta}{2} + i\cos 2\Psi \end{pmatrix}, \tag{3.8}$$

where M is the matrix representing a rotation of an angle Ψ and F_{xy} is the Jones matrix for an optical element having linear birefringence along the x and y axes, δ the phase delay between the two linear eigenpolarizations. Then using the 3.5, 3.6, and 3.8 we obtain the expression of energy lost in input polarization:

$$1 - \chi = \sin^2\frac{\delta}{2}\sin^2(2\Psi - 2\theta). \tag{3.9}$$

We notice that, when we have an horizontal or vertical polarization ($\theta = 0, \pi/2$) this expression is equal zero for $\Psi = 0$ *or* $\pi/2$, therefore we expect a black cross in beam carrying the energy $1 - \chi$. This beam will present a different transverse profile respect to TEM00 input beam.

The value of $\delta = \frac{L(\Delta n_r - \Delta n_\Psi)}{\lambda}$ is determined by the photo-elastic effect, and depend on the temperature gradient [32].

$$\delta(r) = \frac{4\pi L}{\lambda} C(\alpha*, n_0, \nu, p_{ij}) \frac{1}{r^2} \int_0^r r^2 \frac{dT}{dr} dr. \tag{3.10}$$

where C is a characteristic coefficient of the medium, dependent by the thermal expansion coefficient $\alpha*$, the refractive index n_0, the Poisson' ratio ν and the photo-elastic coefficients p_{ij}. The coefficient C for a crystal with [1 1 1] orientation becomes [33]:

$$C(\alpha*, n_0, \nu, p_{ij}) = \lambda Q\big[\frac{1+2\xi}{3}\big], \tag{3.11}$$

with

$$Q = \alpha^* \frac{n_0^3}{4} \frac{1+\nu}{1-\nu} \cdot (p_{11} - p_{12}) \qquad \xi = \frac{2p_{44}}{p_{11} - p_{12}} \qquad \Psi = \phi. \tag{3.12}$$

Using the equations (3.9) and (3.10) and (3.3) we can calculate the rate of the power lost in input polarization normalized to the total beam power, integrating over the cross-sectional area of the crystal :

$$\gamma = \frac{\int_0^{2\pi} \int_0^R (1-\chi) e^{-r^2/r_0} r dr d\phi}{\pi r_0} \tag{3.13}$$

where R is the radius of the crystal. In figure 3.5 the losses rate is reported as a function on the input power beam. We note that a plateau appears for very high power. The result was obtained by expanding the 3.3 around r=0.

3.2.3 Measurements of the conversion rate γ

In order to measure the losses rate γ we placed a TGG crystal, 8mm long with absorbtion $\alpha = 1600ppm$, between two crossed polarizer as shown in figure 3.6. The first polarizer ensure that the polarization is horizontal respect to optical bench and the second polarizer project the output beam along the vertical polarization axis, the laser used is a a commercial 200W ytterbium fiber laser from IPG photonics. We observe a cross figure (HG11 Hermite Gauss mode see Appendix A) as said in section 3.2.2 by using a commercial CCD. By rotating the input polarization also the cross rotate (see fig. 3.7) and a LG02 (Laguerre Gauss mode) appears, consistently with the (eq.3.9).

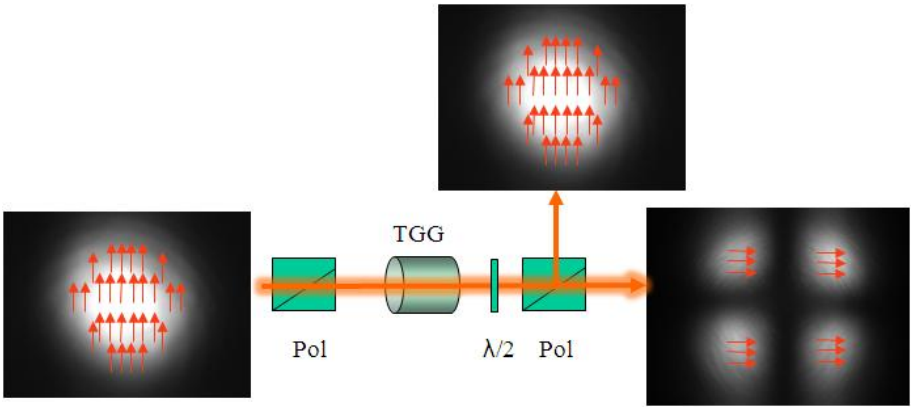

Figure 3.6: The laser beam impinging on the TGG self-induce a changing of polarization and of the transverse profile with a given conversion rate γ

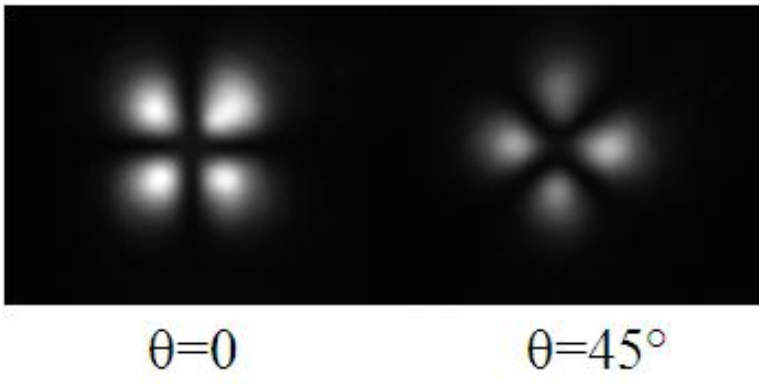

Figure 3.7: Shape of beam at two different input polarization

With a power-meter we measured the power of this beam, for input power until 130W. We obtain a set of experimental measurements in agreement with the γ theoretical beahvior see fig.3.8. These measurements produce a isolation ratio of the FI lower than $40dB$ and not compliant with the requirements of the AdV injection system. Further more they alert us that HG11 (TEM11) beam could be sent to the interferometer core. About the second issue $\gamma \sim 0.2\%$ for 200W input power, this value is much smaller than requirement for AdV Virgo of non-TEM00 power $< 5\%$.
To obtain an isolation ratio bigger than $> 40dB$ as required, we need a compensation for this unwanted effect. An experimental compensation method was implemented for similar crystal for 100W power in [34], but without any theoretical explanation. In order to understand the physics origin of this compensation and to optimize it one until 200W in vacuum, we had more carefully analyzed the involved effects. For this aim we compared the mode conversion observed with similar effect produced in new liquid crystal optical device called Q-plate. An efficient compensation technique can't disregard an accurate understanding of the phenomenon to compensate.

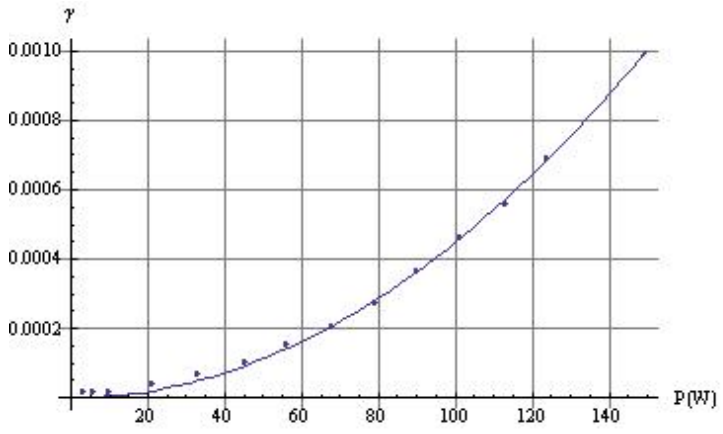

Figure 3.8: Measurements of rate conversion γ on a TGG crystal 8mm long until $P_{in} = 130W$

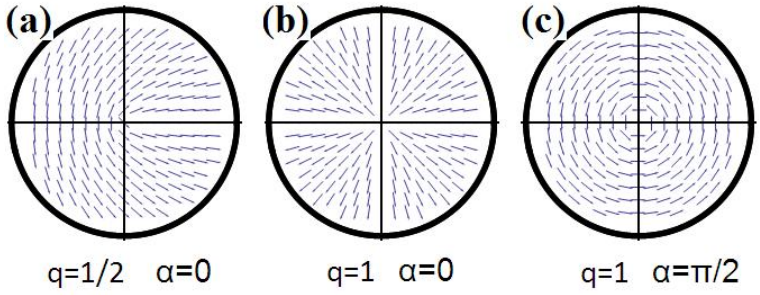

Figure 3.9: Typical pattern liquid crystal in Q plates

3.2.4 Q-plate and Spin to Orbital Conversion (STOC)

It was recently demonstrated [35] that a birefringent plate made of a vortex-patterned liquid crystal film can change the spin angular momentum (SAM) of photons to orbital angular momentum (OAM) going trough them. This particular optical elements are called Q-plates (QP) and the conversion SAM-OAM is know as STOC (spin to orbital conversion).
In a Q plate the birefringence optical axis orientation in the xy plane is specified by the angle Ψ that the liquid crystals orientation form with the x axis. It is assumed to be given by the following equation:

$$\Psi = q\phi + \alpha_0 \tag{3.14}$$

where q and α_0 are constants and ϕ is the angular polar coordinate. In figure 3.9 are the typical patterned liquid crystal used to realize Q-plates are shown.

The main characteristics of a light beam carrying OAM is the presence of a topological point-charge in the optical phase

$$\mathbf{E}(r,\phi) = \mathbf{E}(r)e^{im\phi} \tag{3.15}$$

with OAM=2q. A beam of photons in an OAM auto-state is know be in a hypergeometric mode of electromagnetic field belonging to overcomplete and nonorthogonal set of modes [36](see Appendix A).
The particular birefringence plates cited above can imprint a topological charge into the optical phase of the incident light and the beam acquire a phase factor $e^{im\phi}$, with $m = 2q$, thus it transfers the OAM. In passing

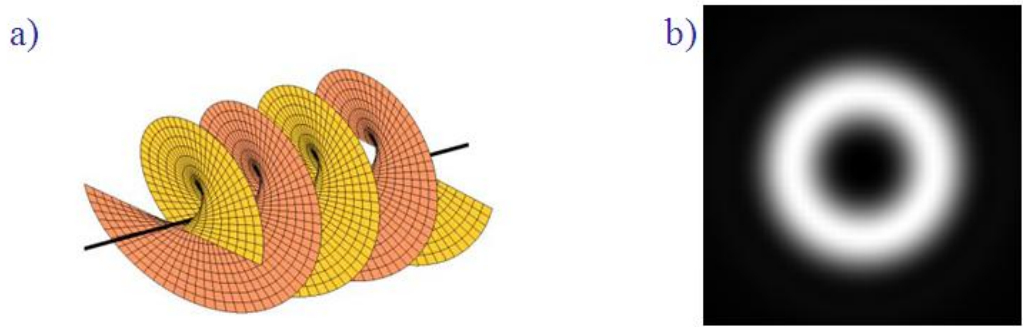

Figure 3.10: The wave front of a beam carrying OAM is helicoidal and the beam shape is a doughnut beam (see Appendix A)

through the plate also the spin changes to ensure the total AM conservation.

To compute the E_{out} we can use Jones matrices as in section 3.2.2. by supposing that each photon carries a $+\hbar$ spin, then using a left circularly polarized light we obtain:

$$E_{out} = E_0 e^{i2\phi} e^{i2\alpha_0} \begin{pmatrix} 1 \\ -i \end{pmatrix} \tag{3.16}$$

The wave emerging from the q plate is therefore uniformly right-circular polarized, as would occur for a normal half-wave plate, but it has also acquired a phase factor $e^{im\phi}$, with m = 2q. It has been transformed into helical wave with orbital helicity 2q (see fig.3.10a) and orbital angular momentum $2q\hbar$ per photon as above anticipated.

It is possible to describe the transverse profile of E_{out} when, for example, LaguerreGauss (see appendix A) beam impinges on Q plate [37]. In the case of a LG00 (TEM00) incident on 1-plate, E_{out} vanishes as $r^{\sqrt{2}}$along the beam axis so that the intensity profile has the characteristic doughnut shape shown in figure 3.10b.

Above we said that when a medium with a not negligible absorption, as a TGG magneto-optical crystal is crossed by an high power beam, it will be affect by a radial temperature gradient, consequently a local radial birefringence, induced by photo-elastic effect, appears and the TGG becomes a Q-plate with birefringence axis $\psi = \phi + \alpha_0$. In figure 3.11 is shown the analogy between the map of strain (coincident with Ψ)in TGG [111] oriented and

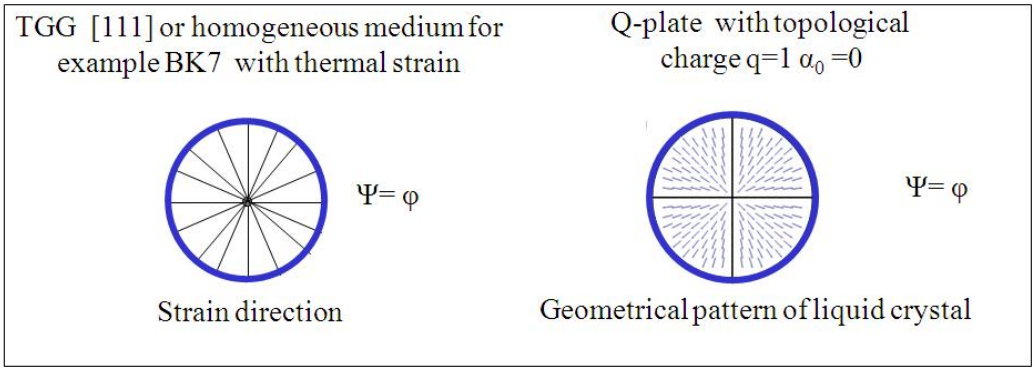

Figure 3.11: Analogy between of strain map in absorbing medium and liquid crystal geometrical pattern in Q-plate. The similitude is evident.

the liquid crystal vortex pattern of Q-plate with a topological charge q=1 and $\alpha_0 = 0$. Thus we expect that the beam passing trough the TGG will be partially converted by TEM00 mode in higher transverse mode, acquiring OAM . This effect could be very useful in the study and application of Q plate contest (quantum information for example), but it was investigated here in order to compensate it in high power faraday isolator.

3.2.5 Wave-front shape analysis and quantum tomography of the converted beam

Here we experimentally show that out beam after TGG crystal presents an helical wave front, meaning that a topological charge is present in its phase eq. (3.15). We also made a tomographic analysis to quantitatively measure the OAM

We used a beam of light with circular polarization, thus each photon carries $\pm\hbar$ of angular momentum depending on the handedness of the polarization, and we produced the "doughnut-like" beam with unknown topological charge (see fig.3.12).

To analyze the wave-front beam we used the interference of this one with a wave-front plane.

The experimental set-up is composed by a Michelson like interferometer, (see fig. 3.13) with a polarizing beams splitter instead of a simple beam splitter

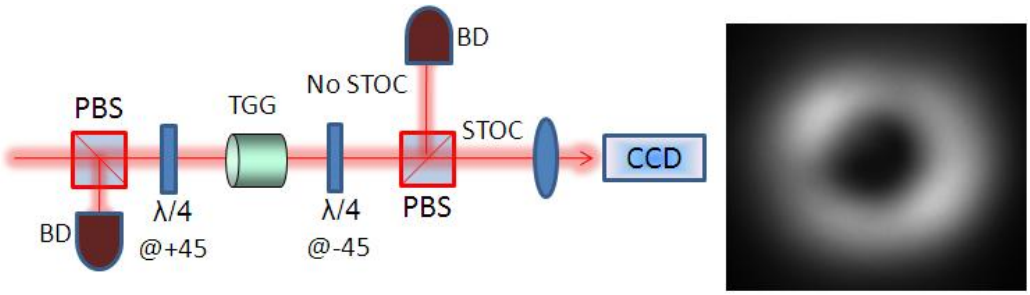

Figure 3.12: With a circular impinging polarization, after the TGG crystal a part of beam is converted in doughnut beam

and two quarter wave plate added in each arms, (oriented at 45 degrees w.r.t. PBS's polarizations). However, the two beams, instead of coming back to the same directions, exit at the 4st face of PBS with different polarizations. By adding a cube polarizer we select a portion of both light and we controlled the visibility of fringes. In the TEM00 arm we added a lens in order to enlarge the beam with a proper focal length.
For non helical waves, the resulting interference pattern would be made of concentric circular fringes. If the wave front of the beam is helical, the pattern takes instead the form of a double spiral [35]. After finding the proper coherent distance the Double-Helical fringes appeared with a good visibility. Figure 3.14 shows the CCD-acquired images.

In order to quantitatively measure the OAM carried by beam by using the technique described in [38]. We have used a complete set of tomography in the orbital angular momentum (OAM) Hilbert space . With six different phase holograms we projected the beam's OAM in the +2 and -2 (binary) Hilbert space associated to tomography in the SU(2) space. First, we measured the hologram efficiencies in the first order of diffraction for this wavelength, 1070 nm, by impinging the TEM00 input beam. Efficiency is defined by intensity at the first order of diffraction divided by the impinging intensity. Then, we put these holograms along the beam path and we measured the intensities at the first order of diffraction. Moreover, by doing this six projections all six "Stokes"- like parameters in the OAM space can be measured [39]. The OAM density matrix is well- measured and de-

fined. Our analysis showed that this beam, indeed, possessing OAM=2. The density matrix proves that the beams possessing OAM=2 with purity of 98%

The same measurements were done with TEM02 beam produced using linear polarization as in section 3.2.3, The CCD diplay shown a double pitch-fork patterns (seefig.3.14) d) and tomographic measurements also had detected the presence of equally shared OAM=±2.

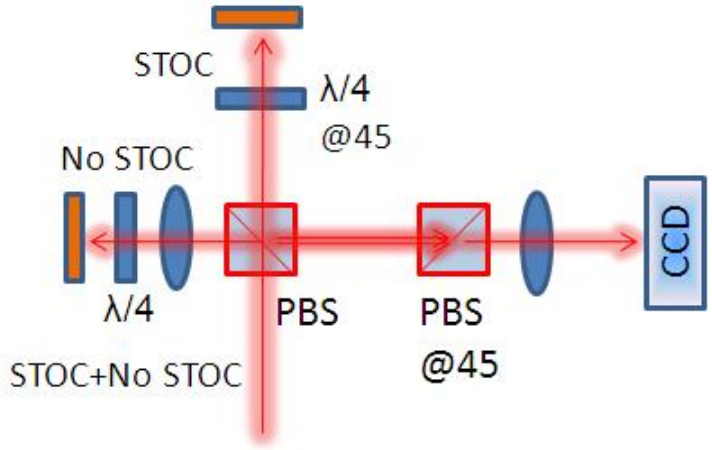

Figure 3.13: Set-up for analyzing the front wave shape

3.2.6 Compensation of STOC effect for AdV FI

As said above, in AdV the STOC effect deteriorates the isolation ratio of FI that depend on conversion rate γ.
We computed γ for the TGG and a Q-plate as done in section 3.2.2, but now we consider also the z-propagation, the graph as a function of the length L are reported in figure 3.15.

The real difference between the self-induced STOC in TGG and STOC in Q-plate is the phase delay. In fact for the first one it depends on natural birefringence of liquid crystal:

$$\delta_{QP} = \frac{L\Delta(n_o - n_e)}{\lambda} \tag{3.17}$$

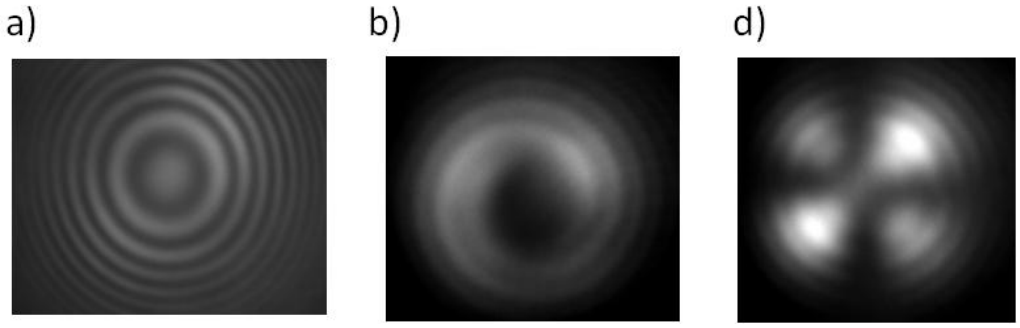

Figure 3.14: a) Interference fringe between a wave plane and TEM00; b)interference fringe between a doughnut beam and a wave plane,d) interference fringe between a mode HG11 and a wave plane. The double helical and double fork reveal that the beams posses OAM

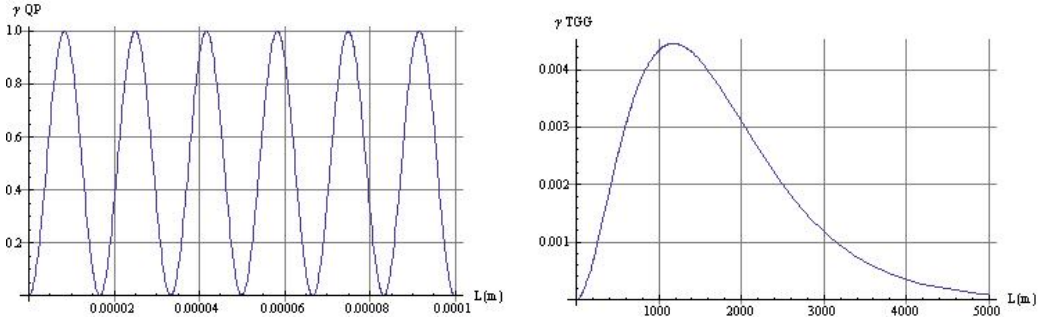

Figure 3.15: The first graph show the conversion rate of a Q-plate (liquid crystal), the second one show the rate conversion of TGG crystal more lower than first one

where n_o and n_e are respectively the ordinary and extraordinary refraction indeces. The second one it depends on the birefringence induced by the temperature gradient $\frac{dT}{dr}$, dependent on r (eq.3.10). It results that γ_{QP} is a sinusoidal function and can be easy minimized, while γ_{TGG} is an increasing function for very big L, therefore cannot minimized by tuning L.
We theoretically will demonstre that an optical system, as that one used in [34], can reconvert the STOC beam, restoring the initial polarization, whatever phase delay δ comes (see fig3.16). For this aim we consider a ket belonging to Hilbert subspace composed by spin and orbital angular

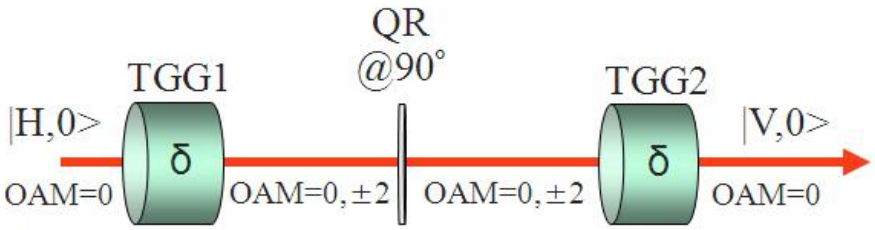

Figure 3.16: This configuration can compensate the STOC effect for any δ induced by birefringence.

momentum $|s, l>$. We will use a particular notation [38], where the spin ket of photons is indicate with their polarization:

state	polarization
$\|H>$	horizontal
$\|V>$	vertical

(3.18)

When photons in the state $|H, l>$ or $|V, l>$ impinge on TGG, the Q-plate effect convert the spin to $OAM = l \pm 2$ as experimentally demonstrated in previous section. Quantitatively we can express the photons state respectively as:

$$\cos\frac{\delta}{2}|H, l> -\frac{1}{2}i\sin\frac{1}{2}[|H, l-2> +|H, +l+2> +i(|V, l-2> -|V, l+2>)] \tag{3.19}$$

or

$$\cos\frac{\delta}{2}|V, l> +\frac{1}{2}\sin\frac{1}{2}[|H, l-2> -|H, l+2> +i(|V, l-2> +|V, l+2>)]. \tag{3.20}$$

We consider two TGG and between them a quartz rotator (@90°) (see Appendix B) as in figure 3.16. By using the equations 3.19 and 3.20 with few states we obtain

$$TGG \cdot QR \cdot TGG|V, 0>= |H, 0> \tag{3.21}$$

or

$$TGG \cdot QR \cdot TGG|H, 0 >= |V, 0 > \tag{3.22}$$

In this way the converted component disappears and also we restored a linear polarization (the beam wasn't irreversibly depolarized, but it was apparently).
The two TGG have to tuned (by varying their length or the magnetic field) in order to obtain the right rotation of polarization to recover the Faraday isolation as described in section 3.2.
In particular the first TGG1 rotate of 22.5°, the quartz rotator add 67.5° to obtain a 90° rotation before the second TGG2 as above requested for the STOC compensation. TGG2 rotates also the polarization by 22.5°. In the back-reflected light (with direction antiparallel to magnetic field B)a rotation 45° is added by two TGGs and $-67.5°$ by the quartz rotator (symmetric optical element see Appendix B). Finally we obtain 90° rotation to assure the Faraday isolation (see fig.3.17).
It is important to note that the perfect STOC compensation require an exact phase delay δ for two TGG crystals. Small differences produce linear terms on δ for $OAM = \pm 2$. In [34] was obtain an isolation ratio>40dB for 100W input power. Since in AdV Virgo the power will be 200W, possible optimizations of the STOC compensator will need. A solutions could be an active control of the phase delay of the TGG2, for example by inducing a little temperature gradient to compensate the one induced by the beam laser. Otherwise an active compensation could be implemented substituting the TGG2 with a tunable Q plate, where δ_{QP} can be directly controlled by applying a external electric field.

3.3 Thermal lensing analysis and compensation

Induced thermal lensing is a serious problem that appears in any absorbing material. This effect consist in an optical distortion caused by the change of the refractive index $\Delta n(r)$ and by the length variation $l(r)$ of crystal. The change of the refractive index can be separated into a temperature and stress

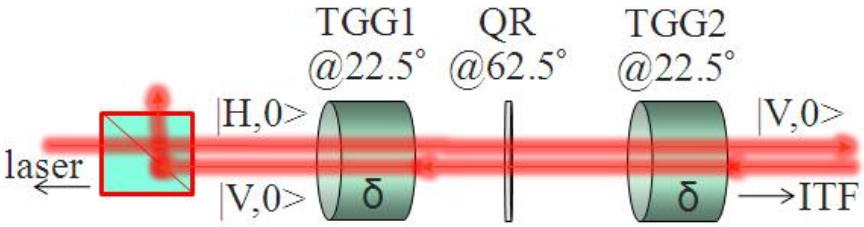

Figure 3.17: The faraday effect is assured by this configuration, that also can compensate the STOC effect.

dependent variation. Hence

$$n(r) = n_0 + \Delta n(r)_r + \Delta n(r)_\epsilon, \tag{3.23}$$

where n(r) is the radial variation of the refractive index, and $\Delta(r)n_T$, $\Delta(r)n_\epsilon$ are the temperature and stress dependent changes of the refractive index, respectively. The temperature dependent change of refractive index can be expressed as

$$\Delta n(r)_T = [T(R) - T(r)](\frac{dn}{dT}), \tag{3.24}$$

where R is the radius of crystal. Instead the stress dependent change due by photo-elastic effect produce a negligible contribute to the thermal lensing. The change in the refractive index leads to a change in optical path length. The optical path length Z(r), at distance r from the center of the beam, is given by:

$$Z(r) = n_0 L + \int_{-L/2}^{L/2} \frac{dn}{dT}[T(R) - T(r)], dz \tag{3.25}$$

where L is crystal length and z is the propagation axis.
Since the optical path length depends on the distance from the center of the crystal, the crystal becomes a thermal lens as shown in figure 3.20. There is an other contribution to this effect due to the so called end effects. In fact on the end-faces the stress produce a distortion of flatness. The deviation from the flatness of the crystal ends is obtain from:

$$l(r) = \alpha^* l_0[T(R) - T(r)], \tag{3.26}$$

where l_0 is the length of the end section of the crystal over which expansion occurs, and α^* is the expansion coefficient.

The radius of the end-face curvature is $R = -(\frac{d^2l}{d^2r})^{-1}$ and the focal length can be obtained from the thick-lens formula of geometric optics:

$$f = \frac{R}{2(n_0 - 1)}. \tag{3.27}$$

However the main contribute to thermal lensing is the one due to the temperature change of refractive index. This contributition depends by temperature map T(r) of the crystal. To obtain this map we have to solve the heat equation and we have to consider also the contributions of the heat radiation and heat convection.
The energy radiated contribute can be obtain by Stefan Boltzmann law:

$$U = \sigma T^4 \tag{3.28}$$

where U is the radiated energy per surface and time unity and $\sigma = 5.67 * 10^{-8} Jm^{-2}K^{-4}s^{-1}$ is the Stefan Boltzamann constant. To compute the convention effects we use an empirical model [40]:

$$\frac{dQ}{dt} = b(T - T_{ref})dS \tag{3.29}$$

where the value of free parameter b can vary between [10:100], corresponding to the turbulent case (b=10) and the laminar case (b=100), Q is the heat, dS is the infinitesimal surface element, T is the temperature and T_{ref} , the temperature of the TGG crystal when there is no laser beam passing through it. To simulate the thermal lensing in a Faraday isolator it was developed a FEM (finite element model) simulation [40]. The mesh for the FEM simulation and the temperature map are shown in figure 3.18.
To study the thermal lensing effects we used the set up shown in figure 3.19. We used the 200W pump laser to heat up some faraday components located in the test area. The lensing effects are evaluated by looking at the modifications of a low power single mode laser (JDS Uniphase 100mW NPRO laser) used as a probe beam. This laser is sent on the element to be tested in opposite direction and polarization with respect to the pump beam. The probe laser is then analyzed with a Shack Hartmann wave front analyser .

Figure 3.20 gives the results of these measurements for different laser power from 10 to 85 W for a TGG of the Northrop Grumann, compared by

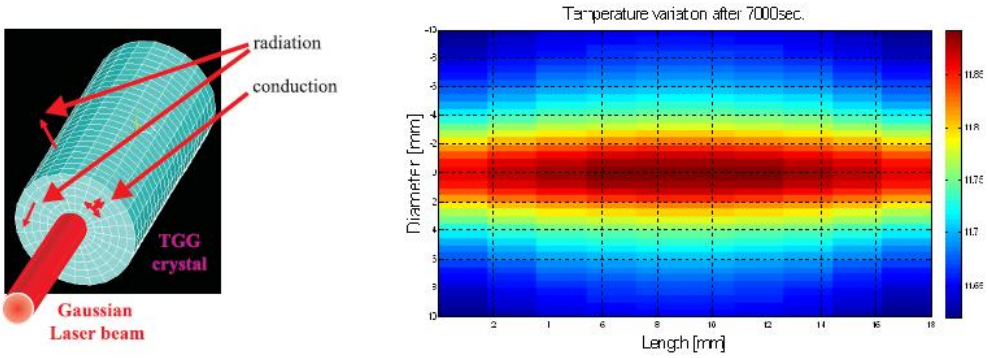

Figure 3.18: Picture showing the mesh for FEM simulation in the crystal and in the surrounding medium to be studied

simulated focal length for different values of absorption of the crystal. The simulations are in good agreement with the measurements, with absorption values close to the manufacturers one (about 1500 ppm).

All these measurements have been carried out in air. In vacuum, as only the radiation is cooling down the samples, the heating of the crystal is much different. Nevertheless we could show with the simulation that the thermal lensing is quite the same, due to the fact that it depends mainly from the radial temperature gradient inside the crystal and not on its average temperature. In-vacuum measurements are planned to confirm the simulations results.
We can see in these measurements that already at average power, we are experiencing significant lensing effect (23m is reached at 84 W for TGG crystal) in TGG crystals. It is clear that the base design of the faraday isolator has to be modified in order to reduce this effect when going to high power. One possibility is to include, in the rotator, a element realizing a passive compensation of these geometrical distortions. For example it is possible to include a DKDP crystal (Potassium Diteuterium Phosphate) of which exhibits a large negative dn/dT values ($dn/dT_{DKDP} = -4.4.10^{-5}K^{-1}$ to compare with $dn/dT_{TGG} = 1.9.10^{-5}K^{-1}$). With the same setup, we performed some tests at different laser power with a 10 mm z-cut DKDP provided by MolTech GmbH. With the measured values, we could compute the length of DKDP

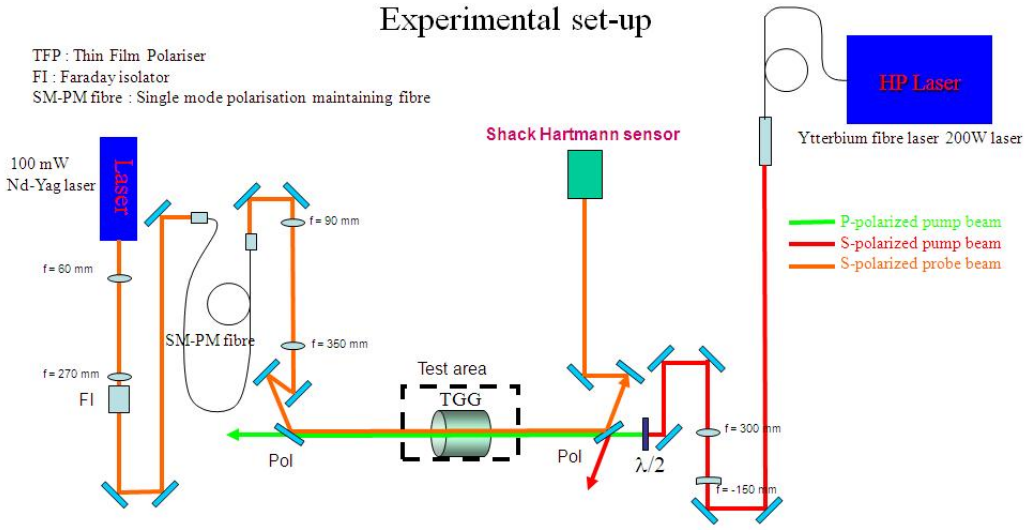

Figure 3.19: High power input optics test bench scheme.

necessary to correct for the TGG distortions. As an example a TGG of 1600 ppm losses heated by 40 W can be corrected using a length of DKDP of about 5 mm (see fig.3.21).

3.4 Rotation of polarization with Verdet V(T)

The last thermal effect spoiling isolators properties is the modification of the rotation angle of the faraday rotator when the TGG crystal is heated. This is due to the temperature dependence of the Verdet constant V and can be derived from:

$$\delta\theta = \frac{1}{V}\frac{dV}{dT}dT\theta \tag{3.30}$$

where dT is the temperature change of the Faraday crystal due to laser heating and θ the angle in (3.1). This effect results in a loss of isolation observed when ramping up power inside a faraday isolator. We measured this loss of isolation for power going from 2 to 48 W. These tests were done by tuning the isolation at low power (2W) and by measuring the ratio between back transmitted light and total light sent back into the isolator when the power is increased. As we can see in figure 3.23, the isolation change is much

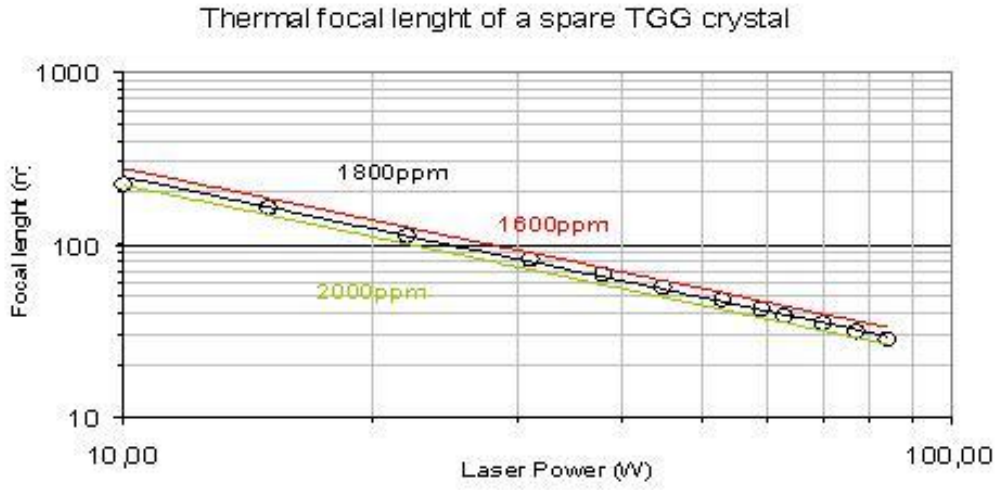

Figure 3.20: Thermally induced lensing in TGG.

Figure 3.21: Thermally induced lensing in DKDP.

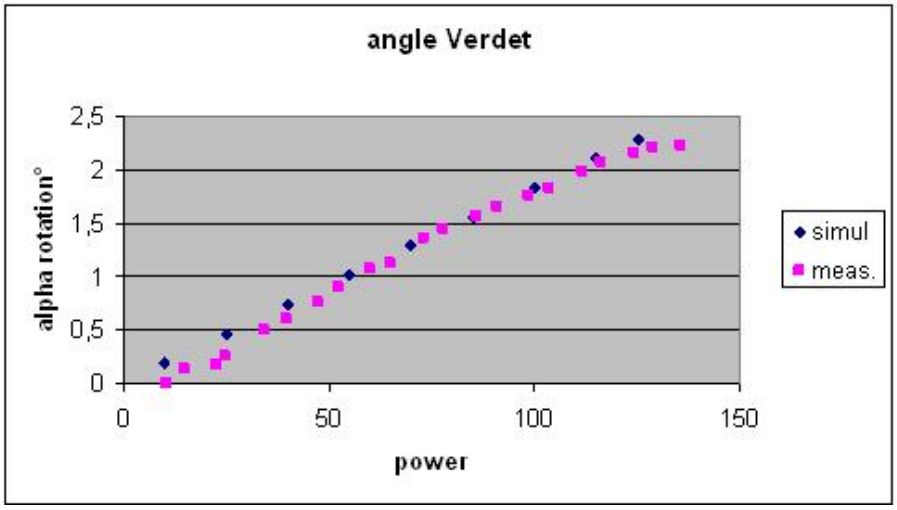

Figure 3.22: Measurement of rotation of θ Verdet compared with simulation.

different in air and in vacuum, due to the different thermal conditions.

In order to compensate this effect, it is possible to introduce a half wave plate inside the isolator (between the faraday rotator and a polarizer) to compensate the rotation change due to the temperature. . Finally this solution has been tested under vacuum for a laser power of 38 W. By turning the wave plate of about 0.7° as foreseen by simulation (see figure 3.22), the isolation can be improved from 32.8 to 36.4 dB. (see figure fig:angle).
The isolation limit is probably due to the other thermal effect discussed above. To compensate the thermal additional angle rotation, an half wave plate motorized, already implemented in Virgo+ experiment will be used in AdV
These analysis and measurements, in additions with the simulation tools that have been developed, helped as to understand thermal effects in the Faraday isolators. The next step will consist to develop a prototype that fulfills all the AdV requirements, in collaboration with Novgorod-IAP group, which scheme will be the one shown in figure 3.24 and to optimize it by using the tools we have developed.

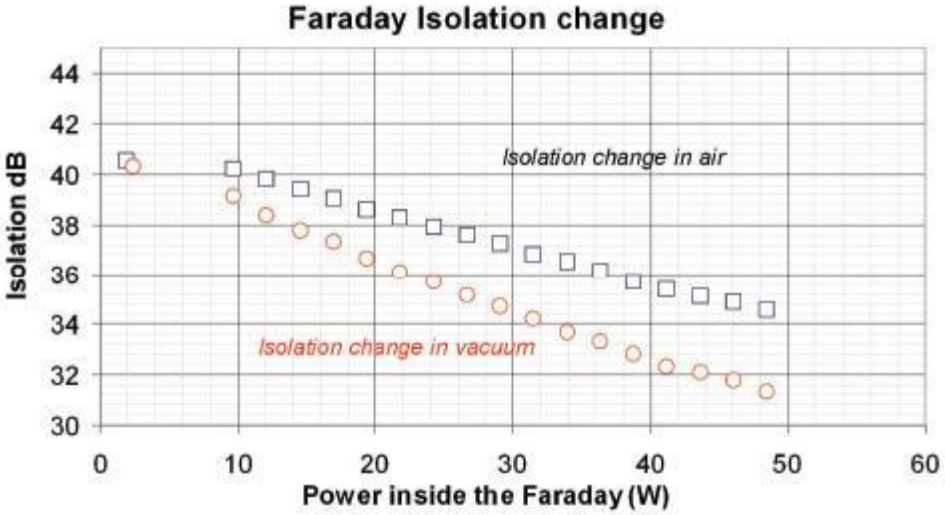

Figure 3.23: Experimental measurement : Faraday isolation change vs laser pumping power (W). in air (squares), in a vacuum (circles).

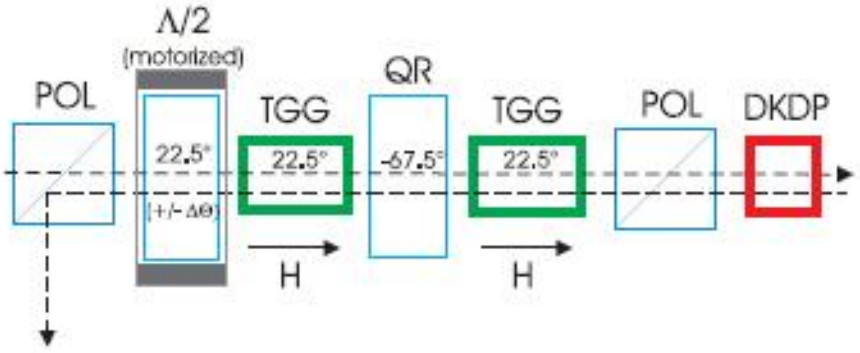

Figure 3.24: Principe of the compensated High Power in-vacuum Faraday isolator.

Chapter 4

Characterization of electrostatic actuators for suspended mirror control

Electrostatic actuators (EA) are one of the most promising devices for mirror control in advanced gravitational waves detectors. An accurate characterization of such actuators is required for a correct design, able to satisfy the requirement of the control system, both in term of low noise content as well as to fit the required dynamic range. In this chapter we discuss the advantage of using of EA system respect to coil-magnet system used at present by Virgo+, and we show a characterization of electrostatic actuation force in air and in vacuum. The measures are compared with a theoretical model. We present also an efficient technique to investigate the spurious charge presence on the mass and show that, by driving the EA with a modulated bias we can minimize the unwanted additional force generated by the spurious charges.

4.1 Actuation coil-magnet system

Presently the actuation system used for suspended mass control by Virgo+ detector are the coil magnet pairs as said in chapter 2. Four permanent magnets are attached to the back of the mirror whose position we want to control and four coils, where current flows, are put in the correspondence of the magnets (see fig. 4.1)on the response mass. Through the application of the magnetic field created by the coils we can control the mirror position.

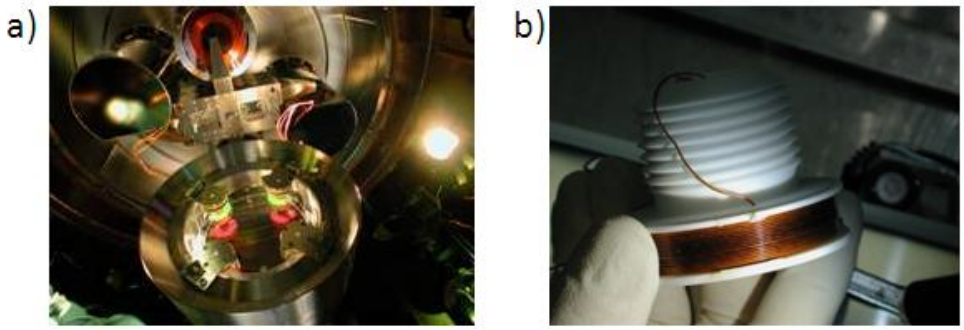

Figure 4.1: a) Last stage of Virgo mirror suspension, b) Depth of a coil

To lock the interferometer on dark fringe, the necessary force is of the order of $10^{-3}N$.

This actuation system introduces few noises sources.

The main drawback of such electromagnetic actuators is the fact that the magnets have to be attached on the mirror surface, which spoils the intrinsic quality factor Q of the mirror, also when silicate bonding technique are used [41], increasing the mirror thermal noise.

An other problem is the coupling with external magnetic fields that produce additional force, generating technical noises. In fact the dark fringe signal is sensitive to the presence of spurious magnetic fields, in proximity of test masses which are not magnetically screened as discussed in [42].

The last issue is linked to the Barkhausen effect the limits the precision in the fine control of the mirrors [43]. This effect consists of a series of sudden changes in the size and orientation of ferromagnetic domains that occurs during the process of magnetization or demagnetization. This effect shows the direct evidence that the magnetization of a ferromagnetic substance by an increasing magnetic field takes place in discontinuous steps, rather than continuously.

These points suggested us the use of alternative actuation system, to control the last stage of suspended mass, based on the electrostatic force.

4.2 Electrostatic actuation system

The use of an electrostatic actuation system could offer several advantages respect to the coil-magnet one. The first evidence is the possibility to use the mirrors as they are, without the necessity to glue the magnets on them. Another advantage is the strongly reduced coupling with external magnetic fields: in fact no direct coupling is possible since there are no magnets. A residual coupling could arise at the level of the marionetta, which is still controlled by magnet-coil pairs, but in this case the residual noise requirements are more relaxed. On the other hand, any possible coupling with variations of external electric fields, is largely reduced thanks to the high electrical conductivity of the vacuum tank where the mirrors are closed.
The working principle of an electrostatic actuator is described by standard electrostatic. For a device of capacity C, polarized at fixed voltage V, the resulting force on a dielectric mass is obtained by calculating the gradient of the stored energy in the system. We have along the z axis:

$$F_z = -\frac{1}{2}\left|\frac{\mathrm{d}C}{\mathrm{d}z}\right| V^2 \tag{4.1}$$

where the capacity depend on the geometric parameter of actuator-mass system. We stress that such forces are always attractive. In the case of actuator for suspended dielectric mirrors, such devices mainly consist in a set of close conductive strips, arranged in a suitable geometry, alternately polarized at two different voltages as shown in fig4.2.

The theoretical expression of the capacity C can be obtain in two step:

- computation of the expression for C_∞ related to an array of electrodes in the free space
- modification of C_∞ in C(z) by applying the method of the image charges to take into account the presence of the dielectric substrate and the dielectric mirror.

The calculation is described in [46], here we want just to recall the most important characteristics. For the simplest geometry, i.e. a set of N parallel conductive strips with period b, rectangular shape of length L and width a, laying on a substrate with relative dielectric constant ϵ_s, placed at distance z

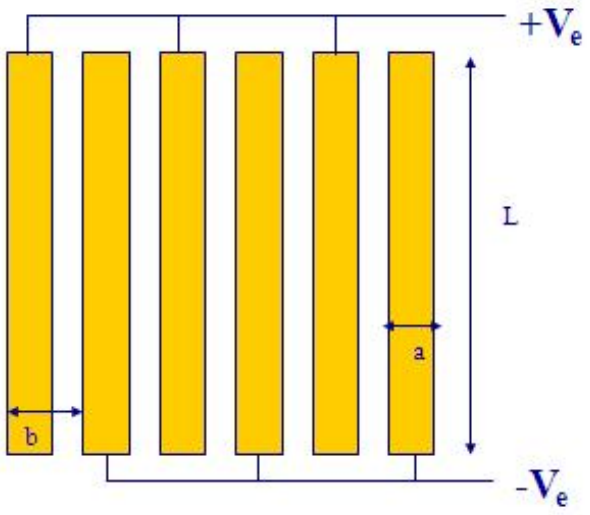

Figure 4.2: A simple scheme of an electrostatic actuator. The force depend by the geometric parameter and by voltage applied

from the test mass having a relative dielectric constant ϵ_m, the capacity can be written as:

$$C(z) = C_\infty \alpha_m \left(\tilde{a}, \tilde{z}, \epsilon_m\right) \tag{4.2}$$

where $\tilde{a} = a/b$ is the normalized strip width, $\tilde{z} = z/b$ is the normalized distance and α_m is a function of the listed parameters describing the effect of the mirror at distance z, while C_∞ :

$$C_\infty = N\pi^2 L \frac{\epsilon_s + 1}{4} \epsilon_0 \alpha_s \left(\tilde{a}\right) \tag{4.3}$$

is the capacity of the isolated actuator, being α_s a function of the normalized strip width that is proportional to the capacity linear density of the electrodes in free space, while the first term, depending on ϵ_s, takes into account the effect of the actuator substrate. It is important to stress that the expression (4.2) is calculated in the approximation of strips with infinite length and taking into account only the contribution of the first image charges, both for the substrate and for the mirror. As a consequence the capacity of real devices become different from the this value for small values of z with respect to b due to the increasing weight of border effects and image charges as the distance decreases [46]. In this work we use a finite element model based on the above

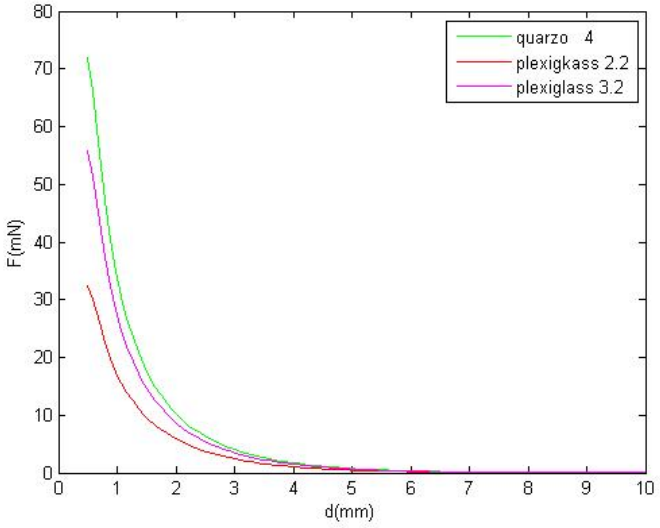

Figure 4.3: The variation of capacity on the dielectric constant.

cited theoretical computation, to simulate the actuator capacity. Therefore we can model the force for any mass-actuator geometry. For example in figure 4.3 is simulated the capacity of a such actuator for different dielectric material of the test mass.

By substituting the capacity (4.2) in the expression of the force (4.1), assuming that the displacement of the test mass is small respect to the static distance d of the actuator, one obtains:

$$F_z = -N\pi^2 L \frac{\epsilon_s + 1}{8} \epsilon_0 \alpha_s \left| \frac{\mathrm{d}\alpha_m}{\mathrm{d}z} \right|_{z=d} V^2 = -\alpha V^2 \tag{4.4}$$

being α the coupling constant of the electrostatic actuator in ($\mathrm{N/V^2}$) where all characteristics, but the polarization voltage, are included.

The last expression has to be modified to consider also the presence of a stray electric charge q on the dielectric mass. In this case, by making the simple approximation that the electric field is proportional to the polarization voltage applied to the actuator, it is possible to write:

$$F_z = -\alpha V^2 + \beta V \tag{4.5}$$

where the factor β is, in general, a function of the charge q, the distance z and the geometry of the actuator. The effects of this term were already

observed on similar set-up [47], and some techniques for its mitigation were already developed [48].

The main purpose of the EA, like any actuation system for the test masses, is the mirror driving to keep the interferometer locked on the right working point, but the expression (4.5) clearly shows a non linear behavior of the force with respect to the applied voltage. Since it is more effective, in the framework of standard control systems, to work with linear actuation systems, a simple approach consists in applying the square root of the driving signal, resulting, because of the square voltage in equation (4.5), in the desired linear driving force. Moreover, to reduce the effect of the stray charges, it is possible to modulate the driving signal, resulting in a zero averaged contribution of the linear term of the actuation force even in presence of charges on the test masses. This driving technique was already successfully experimented in the control of a bench top Michelson interferometer with a suspended mirror controlled by a such EA [49].

To clarify this approach, let $A(t)$ be the driving signal we want to apply on the test mass, A_{DC} the voltage bias and $2\pi\omega_M$ the modulation frequency of the full driving signal. The square root is computed and sent, with the modulation, to the actuator driver. In this way the voltage applied to the actuator is:

$$V = G\sqrt{A_{DC} + A(t)}\cos\omega_M t \tag{4.6}$$

where G is the gain of the EA driver. With this voltage, the force exerted on the test mass becomes:

$$F = -\frac{1}{2}\alpha G^2\left(A_{DC} + A(t)\right)\left(1 + \cos 2\omega_M t\right) + \beta G\sqrt{A_{DC} + A(t)}\cos\omega_M t \tag{4.7}$$

If the modulation frequency is chosen at enough high frequency to have negligible effects on the test mass motion and the frequency content of the driving signal is much smaller respect to ω_M, the force (4.7) only consists of a DC bias term and of a term proportional to the original driving signal $A(t)$.

4.3 Preliminary measurements of actuation force in air

We measured the actuator force exerted on a suspended dielectric mass with a mirror attached on the front face. To sense the mass displacement we used two different experimental set-up placed on the optical bench in air:

- optical lever similar to that one used to read the mirror position in virgo+;
- a Michelson interferometer to measure smaller mass displacements.

The actuator was mounted on a translation stage in order to easily change the distance relative from the suspended mass.

4.3.1 Force measurements with optical lever

Experimental set-up

The working principle of an optical lever reading system is the following: a collimate light sources, in the our case a 1mW super-luminescent LED emitting (SLED) at 830nm (Qphotonics), impinges on the center of the plane mirror place on the suspended mass and the reflected beam is detected by a two-dimensional position sensing photodiode (PSD) model 2044 from Hamamatsu, as shown in figure 4.5. The PSD is a optoelectronic position sensing similar to a standard photodiode but with four outputs. By suitably combining these outputs the beam position or intensity can be obtained (see fig.4.4). These device working as a CCD but allow a continue (not discrete) position with high resolution, furthermore it give a very fast response ($\sim 1.5\mu s$).

The displacement of the mass is geometrically linked to displacement read from PSD by the relation:

$$z = \frac{x_{PSD}}{\sin \alpha} \tag{4.8}$$

where α is lever angle.

In principle the PSD can't distinguish between the mass displacements due to the translations and those one due the mass tilts. In order to decouple the translational motions from the longitudinal ones, a lens with focal length f is added in the path between the mass and the photodiode. In paraxial

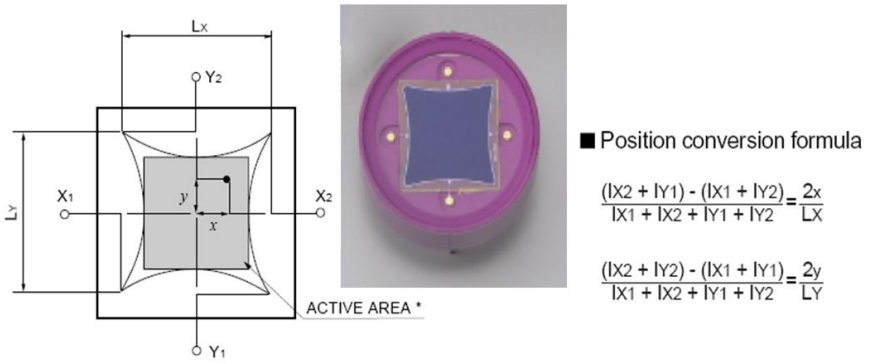

Figure 4.4: Position sensing device

approximation we can use the ray transfer matrix analysis, to compute the relation between the optical vector $(x_{PSD}, \dot{x}_{PSD})$ before the lens and the one after the lens $(x_{PSD1}, \dot{x}_{PSD1})$:

$$x_{PSD1} = \big(1 - \frac{B}{f}\big)x_{PSD} + \big(A + B - \frac{AB}{f}\big)\dot{x}_{PSD} \tag{4.9}$$

where A is the mass-lens distance and B the lens-PSD1 distance as in figure 4.5, the same happen for the other free degree $(y_{PSD}, \dot{x}_{PSD})$. Therefore if we choice $B = B_1 = \frac{Af}{A-f}$ the tilt therm vanish and the PSD read only the mass translation. Idem we could choice $B = B_2 = f$ to only read the mass tilts. Normally it is used a beam splitter and two PSDs are used it when it id neecessary to read both the degrees of freedom. In our case we are interested to read only x_{PSD} that is strictly linked to mass displacement.

The choice of SLED as light source was linked by the low noise introduced in the position signal. In fact respect to laser, they provide an almost monochromatic beam (width-band=20nm), but with a relatively short coherence length (well below 1mm). On the other hand they are not lasing, so they are mode hopping free. The very short coherence length make the LEDs unsuited to cases in which coherent light is needed, as in interferometric optical readouts. For an optical lever there is no need of coherent light. On the contrary the use of incoherent light can be an advantage: the short coherence length avoids the effect of ghost fringes, due to multiple reflections within optical components or windows, which can, in some cases, spoil the

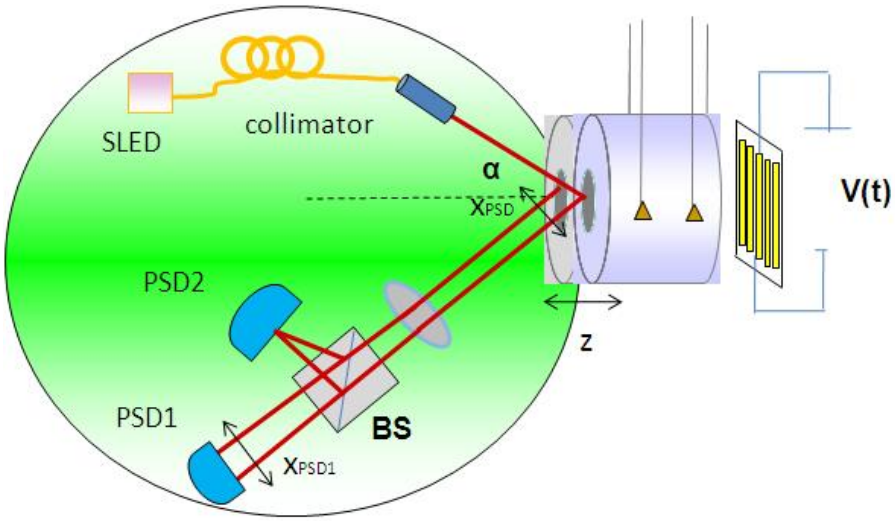

Figure 4.5: Optical lever realized for the EA characterization

sensitivity of the optical lever.
We have measured the displacement noise introduce by different light source, sending the spot directly on the PSD, and analyzing the spectrum of the output signal. Our measurement showed that the SLED is a very gud choice, in fact it presents a level noise about two order magnitude smaller respect to laser sources (laser diode and He-Ne Laser) as show in the figure4.6. The sensitivity of optical lever can be computed, computing the contribution of shot noise and electronic noise, by multiplying them by a conversion factor,

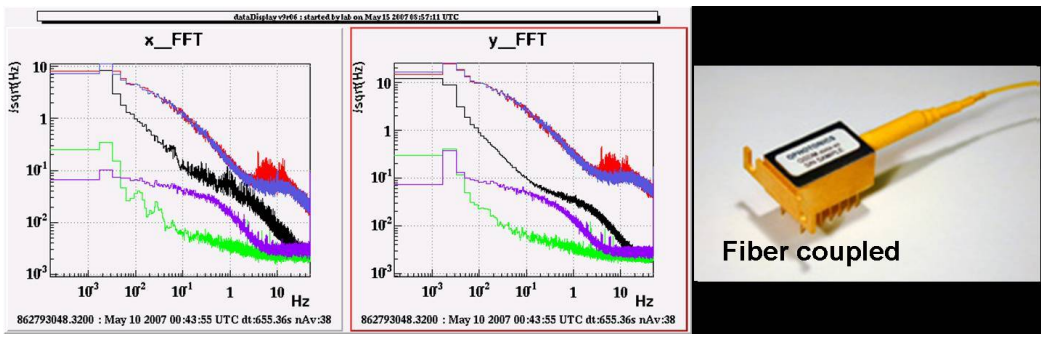

Figure 4.6: Noise measurement of SLED (green curve) compared with laser sources

due by 4.8 and 4.9 and by factor due amplification electronic circuit.
The shot noise, which is due the random fluctuation of the number of photons incident on the light detector per unit of time, results in a current noise I_{SN} in the measured sensor current I_{Ph}, which corresponds to a displacement noise described by the formula:

$$\tilde{x}_{SN} = \frac{\tilde{I}_{SN}}{\frac{dI_{Ph}}{dx}}; \tag{4.10}$$

where the tilde indicates the power spectral density . The shot noise $\tilde{I}_{SN}$ is expressed by $\tilde{I}_{SN} = \sqrt{2I_{Ph}e}$, where e is the electron charge. The photodiode current is evaluated in terms of the optical power P_0 of the light beam and of the photodiode responsivity $\alpha(\lambda)$, depending on the wavelength λ by means of the relation $I_{Ph} = \alpha(\lambda)P_0$
L is the length of PSD, in the interval [-L/2, L/2] the photodiode current ranges from 0 to I_{Ph}. The quantity $\frac{dI_{Ph}}{dx}$ can thus be reasonably approximated by $\frac{2I_{Ph}}{L}$. Taking in account these relations and making $\alpha(\lambda)$ explicit in terms of the quantum efficiency of the photodiode we get:

$$\tilde{x}_{SN} \approx \frac{L}{2}\sqrt{\frac{2h\lambda}{P_0\eta c}} \tag{4.11}$$

Notice that the shot noise limited sensitivity for the lever depends on the light power P_0 and on the measurement range L. The current noise in the trans-impedance amplifier used to read the photodiode current imposes a limit displacement sensitivity given by:

$$\tilde{x}_I = \sqrt{N}\tilde{I}_n(f)|\frac{dI_{Ph}}{dx}| \tag{4.12}$$

where we assume $\tilde{In}(f) = (5.4 \cdot 10^{-12})/\sqrt{f}A/(Hz)^{1/2}$, which is the typical value for a widely used device (Analog Devices OP27EP). The quantity N is the number of current signals: N = 4 for a PSD.

Both the driving and position signals are generated or processed by a digital DAQ system, running at a sampling frequency $F_s = 1$ kHz. The ADC and DAC resolutions are 16 bit, while their range is ±10 V. The driving signal (4.6), is digitally generated by the CPU managing the DAQ system, and is sent, through the DAC, to a commercial HV amplifier, with a gain

$G = 200$, a maximum output voltage of 2 kV and a bandwidth of 1 kHz. The data are visualized and elaborated thanks to software tool that has been developed for the VIRGO experiment and used also in Virgo-lab of Naples.

Force measurements

The measurements where performed by applying, to the HV amplifier, a voltage of the form indicated in equation (4.6), with a simple line at frequency $f = 2\pi\omega = 20Hz << \omega_M$ as driving signal:

$$V = \sqrt{A_{DC} + A_{AC}\cos\omega t}\cos\omega_M t \tag{4.13}$$

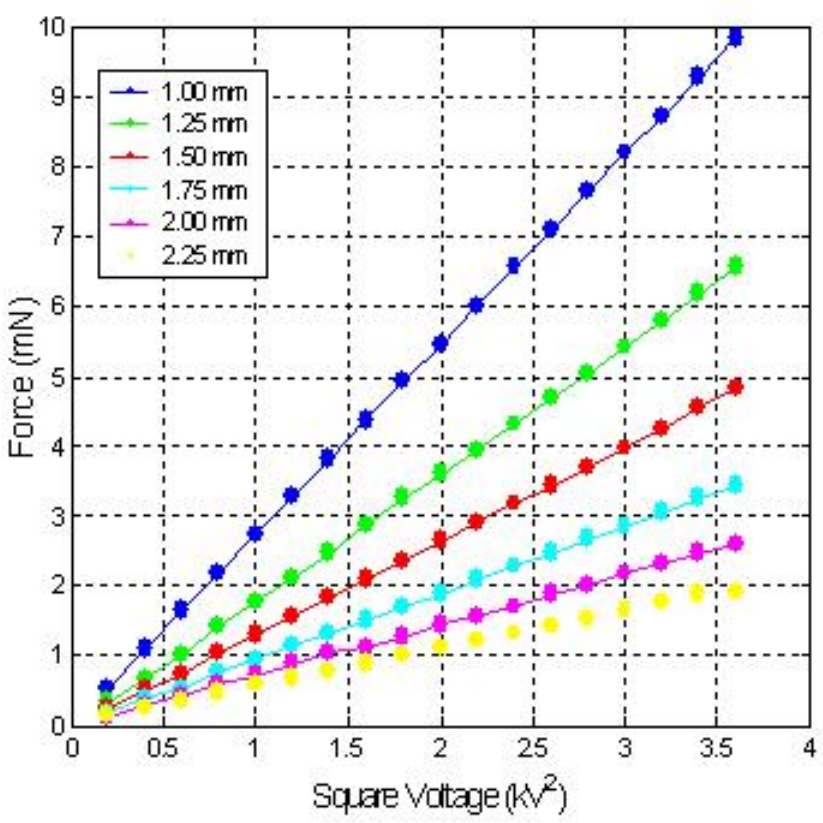

Figure 4.7: Measurement of force in function on the square of potential.

In this way the component at angular frequency ω of the force applied on the suspended mass is:

$$F_\omega = \frac{1}{2}\alpha G^2 A_{AC} = \frac{1}{2}\alpha V_{AC}^2 \tag{4.14}$$

where

$$V_{AC} = G\sqrt{A_{AC}} \tag{4.15}$$

The effect of this force was measured by calculating the displacement spectrum of the mass, using the data coming from the PSD. Finally the displacement was converted in force by taking into account the theoretical transfer function of the suspended mass that can be approximated with a simple pendulum.
The resonance frequency is $f_0 = \frac{1}{2\pi}\sqrt{\frac{g}{l}}$ where $g = 9.8m/s^2$ and $l = 0.18m$, therefore $f_0 = 1.16Hz << f$, in this way f is far from the resonance and we can neglect the effect of the pole of the transfer function. By solving the pendulum equation we obtain:

$$F = x_{mis} m (f_0^2 - f^2) 4\pi^2 \tag{4.16}$$

where m=1.312Kg. We notice that in spite of the optical uncoupling another line at 2.6Hz is present in the spectrum of signal, due the tilt around the vertical axis θ_x, his amplitude is 4% respect to the one due the displacement.

The actuation force was evaluated by sending different amplitude driving signals, at different distances between the actuator and the suspended mass. The force results linear with the square of the potential as shown in figure 4.7. The linearity is good for all the distances analyzed between [d=1-2.25mm]. A graph of force in function on the distances is also reported in figure 4.8.

The performances of optical lever used for these measurements don't allowed as to characterize the actuation force at bigger distances. For this aim we used a semi-suspended Michelson interferometer in order to implement more sensitive measurements.

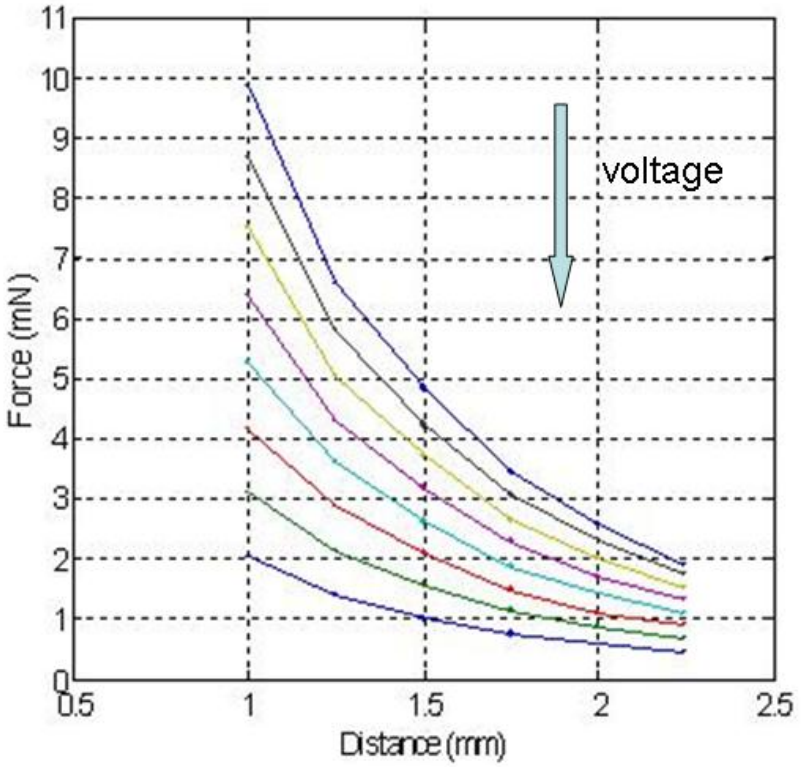

Figure 4.8: force in function on the mass-actuator distance at decreasing potential

4.3.2 Force measurements with a semi-suspended interferometer

We know the a Michelson interferometer allow as to measure very small relative variation of the their arms. We used a set-up, schematically described in figure 4.9 to measure the displacement of suspended mass respect to a mirror fixed on the bench.

The source light is a stabilized He-Ne (Melles Griot) with power P_0=10mW. The light @ 632.8 nm pass trough a Faraday isolator (OFR), after a telescope, with focal lens f_L 38.10 cm and 12.5 cm at distance 20.32 cm, is used to enlarge the beam. The beam impinges on a beam splitter. The arm where 12cm long. The first mirror has mounted on piezo-electric crystal, the other

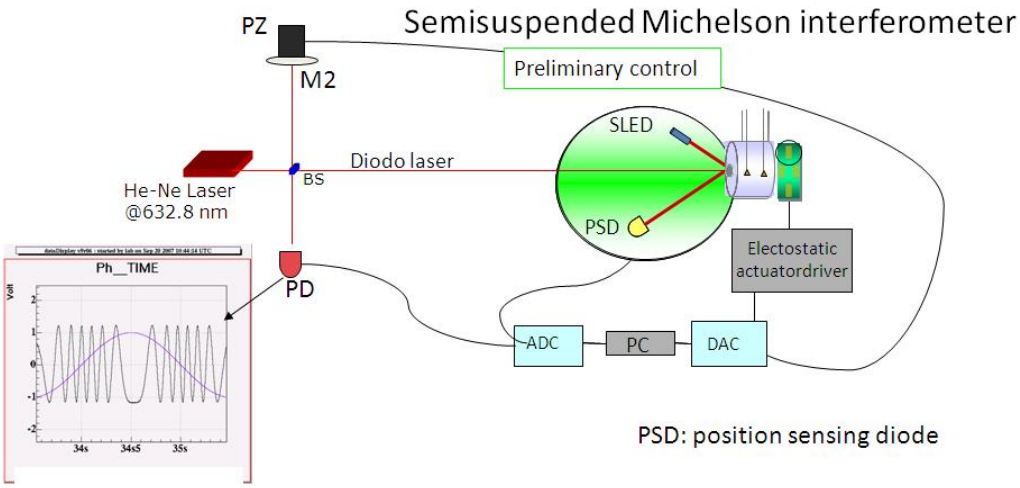

Figure 4.9: Set-up.

one is the suspended mass. mass and the other a fixed bench mirror placed on the piezo-electric crystal . This piezo is produced by Physik Instruments (PI S-315.10): it is a multi axis tip/tilt platform and Z-positioner based on a piezo tripod design. All tree piezo linear actuators can be driven individually by a three-channel amplifier servo-controller. This kind of device provides a longitudinal displacement up to 12 $\mu m(100V)$ and a rotation up to 1.2 μrad (100V) with sub-msec response. In order to characterize the dynamical response of the actuation system we measured the transfer function of the piezo actuator: we sent to the piezo driver a white noise filtered and used a simple optical lever with a Position Sensing Photodiode to read the displacememts. In figure 4.10 the transfer function (TF) is shown.

A preliminary control was implemented using the optical lever as sensor and EA as actuator, because the damping of the mass take a very long time. This control is turn off during the displacement measure.
The acquisition system is the same as described in previous section one.
We have implemented a digital filter to locke the interferometer actuating on the piezo. The interference signal was used both as correction signal and as displacement measure signal.

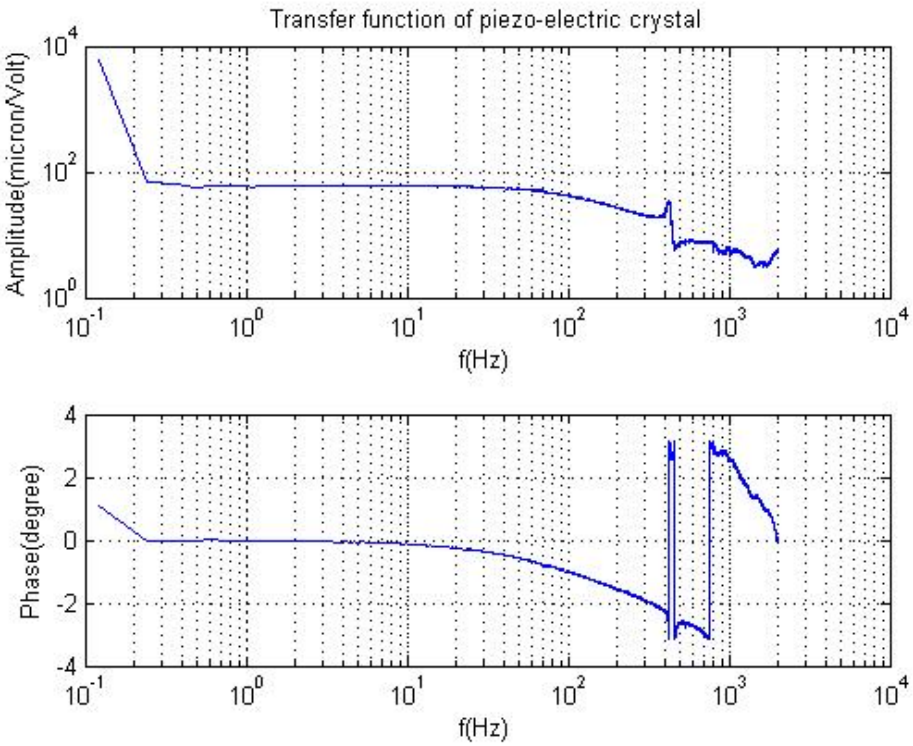

Figure 4.10: Transfer function of piezo-electric crystal.

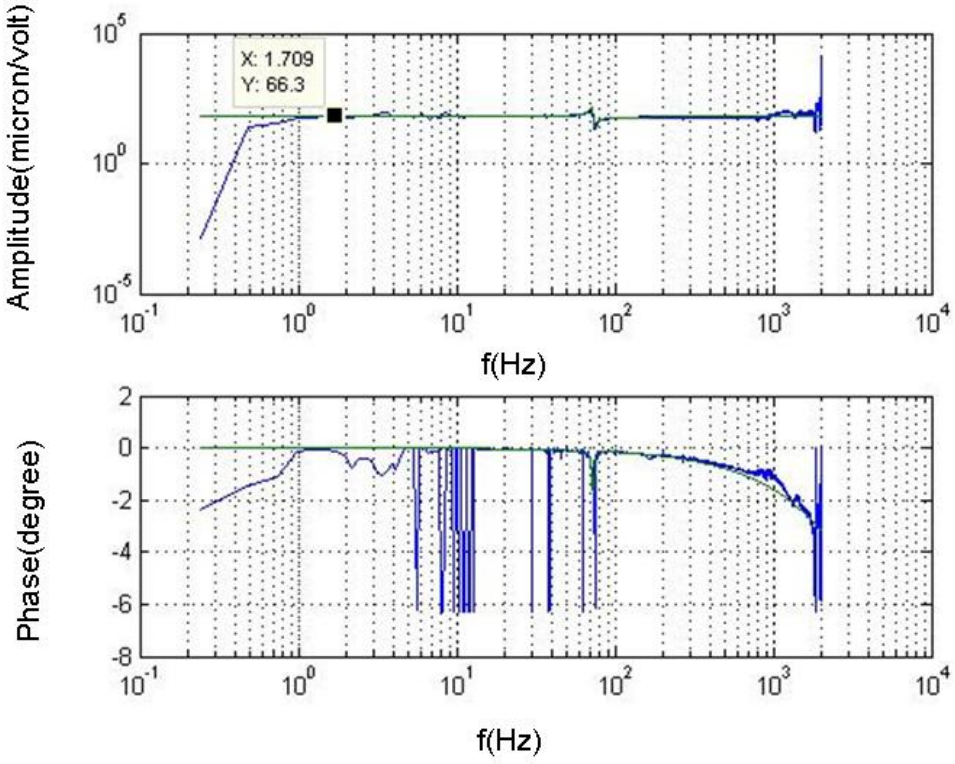

Figure 4.11: Transfer function of semi-suspended Michelson.

The displacement was obtain as:

$$\Delta z = V_{out} \frac{\lambda}{\pi} \frac{1}{V_{in}}, \tag{4.17}$$

where V_{out} is the interference signal read by photodiode PD and V_{in} is the power laser converted in volt by gain of the PD amplification. is shown m/V. In figure 4.11 we reported the function transfer of interferometer. We have fitted it to implement the control filter show in figure 4.12.

In this way we could measure also the weak force exerted by actuator at bigger distances from test mass. In particular In figure 4.13 are shown the force exerted at d=4.5mm, using the signal 4.13 with $A(t) = \cos\omega t$, $\omega = 15Hz,\ 20Hz$ and $\Omega_M >> \omega$.

We observe a good linearity and agreement with the model.

A bigger distance the sensitivity of interferometer is not enough high to detect the mass displacement. We suppose that the sensitivity of our interferometric

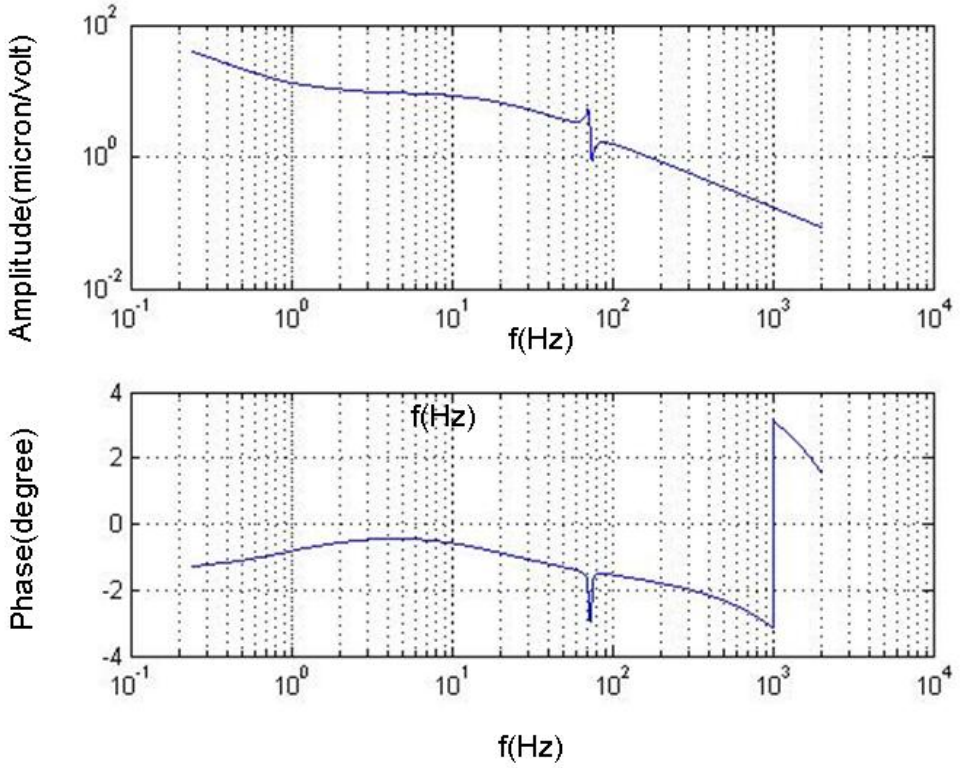

Figure 4.12: Control filter composed by a digital and analogical filter.

detector is limited by presence of spurious charge, in fact in air a great deal stray charge is present. In the next section we describe a technique that we implemented to investigate the presence of spurious charge on the test mass.

4.4 Investigation of spurious charge presence on the test mass

4.4.1 Theoretical computation

The presence of spurious charge on the mass can be investigated by sending a signal with a DC bias. In fact if we observe the displacement spectrum we will observe the presence of multiple frequency, respect to the one injected by the signal.

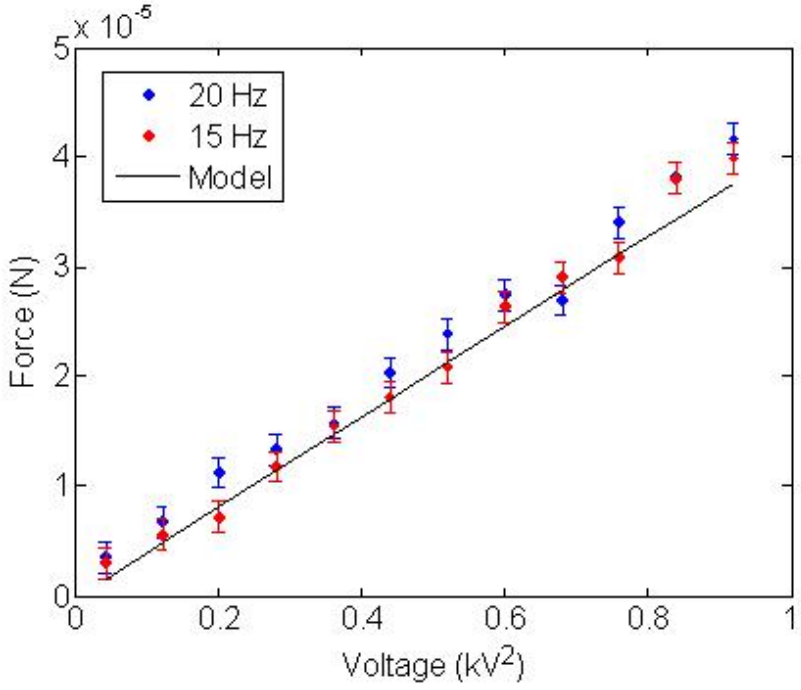

Figure 4.13: Interferometric measure of force compared with the FEM (finit element model)

To compute the amplitude of this multiple multiple peaks we suppose to apply a single frequency signal to the Electrostatic Actuator with square amplitude A_{AC}, frequency $2\pi\omega$, by using a bias square amplitude A_{DC}.

In this case the signal has of the following form:

$$V = \sqrt{A_{DC} + A_{AC}\cos\omega t} \tag{4.18}$$

Now, by denoting with α the coupling constant with the electrostatic force, and by β the coupling constant of the force due to the stray charges present on the test mass, the total force exerted on the mass is:

$$F = \alpha V^2 + \beta V = \alpha(A_{DC} + A_{AC}\cos\omega t) + \beta\sqrt{A_{DC} + A_{AC}\cos\omega t} \tag{4.19}$$

The first term, apart from the DC bias, consists of a signal at fixed frequency $2\pi\omega$, while the second term requires some special attention. We can write the second term of the (4.30) as:

$$\sqrt{A_{DC} + A_{AC}\cos\omega t} = \gamma\sqrt{1 + a\cos\omega t} \tag{4.20}$$

being $\gamma = \sqrt{A_{DC}}$ and $a = A_{AC}/A_{DC} < 1$. We demonstrated that (see Appendix C):

$$\gamma\sqrt{1 + a\cos\omega t} = \gamma\left(c_0 + 2\sum_{n=1}^{+\infty} c_n \cos n\omega t\right) \tag{4.21}$$

where the generic Fourier coefficient is:

$$c_n = -\frac{\Gamma(n - \frac{1}{2})}{2\sqrt{\pi}\Gamma(n+1)}\left(-\frac{a}{2}\right)^n {}_2F_1\left(\frac{n}{2} - \frac{1}{4}, \frac{n}{2} + \frac{1}{4}, n+1, a^2\right) \tag{4.22}$$

where Γ is the gamma function and ${}_2F_1$ is the Gauss Hypergeometric function. Since for real cases $a < 1$, this relation foresees decreasing contribution for all the harmonics of the injected signal.

4.4.2 Experimental investigation of spurious charges

To investigate the spurious charge presence we have to use a set-up placed in high vacuum. In air the increasing stray charges make impossible to send a driving signal without a modulation (DC bias condition), because the additional force, due to the spurious charge, bring an evident drift of the mass as shown in figure 4.14. Furthermore medium vacuum condition also is not optimal, because for high voltage signal we produce unwanted glow discharges. The experimental set-up is based on the use of an optical lever. The mass of the suspended element is still $m = 1.312$ Kg and the length of the suspension wires is $l = 0.18$ m. On the rear face an electrostatic actuator, composed by $N = 20$ strips, with length $L = 8$ cm, width $a = 3.2$ mm, and period $b = 4$ mm, was placed. The EA substrate has a relative dielectric constant $\epsilon_s = 4.47$, while the suspended dielectric mass has $\epsilon_m = 3.7$. All the system, including the PSD, was placed in a vacuum chamber shown in figure 4.15.

The probe beam of the optical lever was sent in the chamber by using an optical fiber and guided to the mirror attached on the test mass by means of a suitable collimator. A schematic view of the experimental set-up is shown in figure 4.17. In order to obtain high vacuum chamber we used a turbomolecular pump (Turbovac see fig.4.16) which can achieve a $10^{-10} mbar$ as ultimate pressure, in series with a rotative pump. Because of the limited

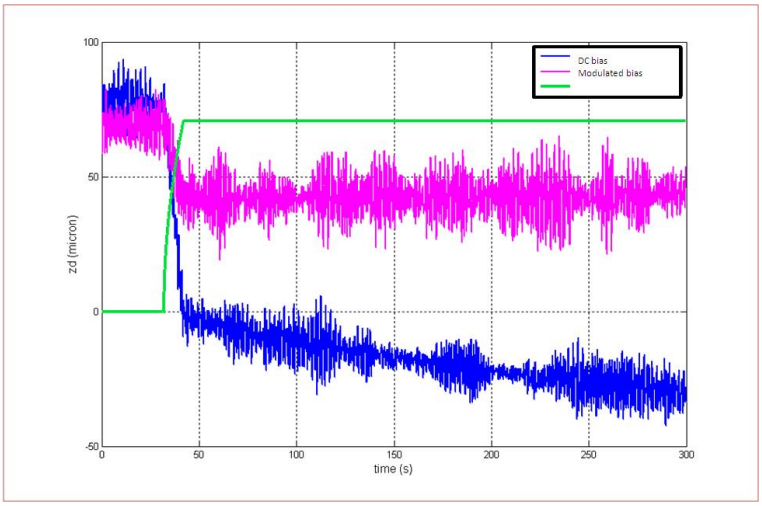

Figure 4.14: Drift of position mass when the DC bias is used

Figure 4.15: vacuum chamber containing the experimental set-up

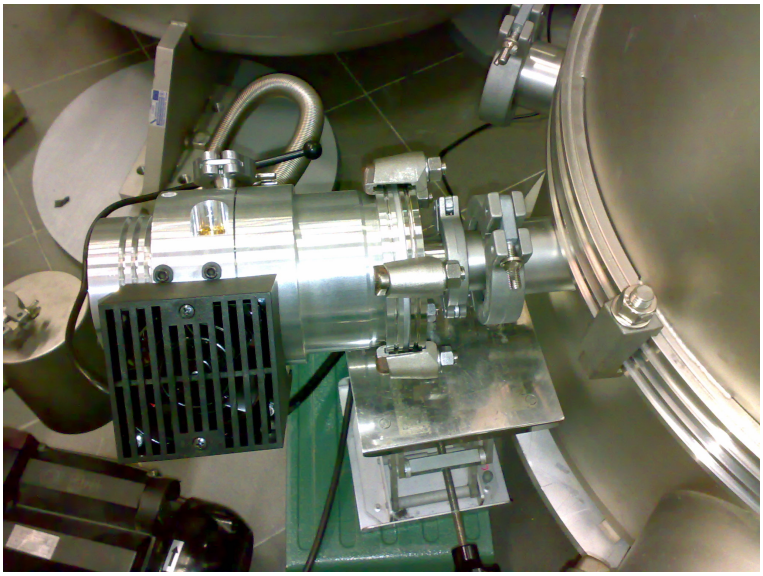

Figure 4.16: Picture of turbo-molecolar pump

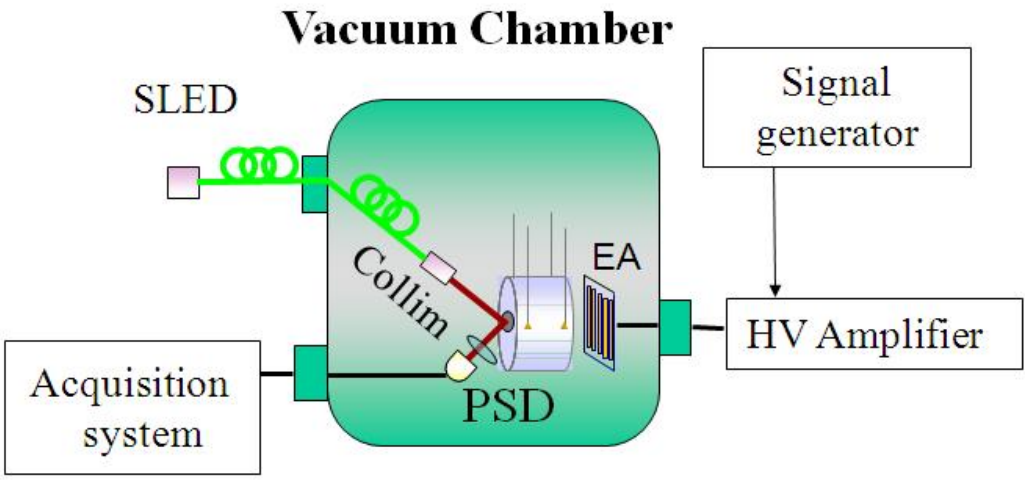

Figure 4.17: Schematic of the experimental set-up.

sampling rate, the modulation frequency for the driving signals was fixed at $f_M = 100$ Hz, that is not a very high value with respect to the suspended mass

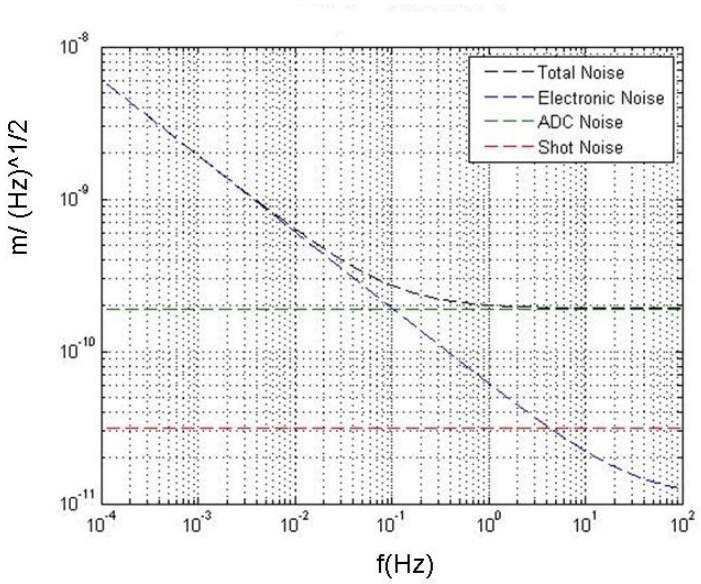

Figure 4.18: Noise contributes at the PSD sensitivity

resonance frequency f_0 (around 1 Hz), but it is high enough for our purposes. The signals coming from the PSD were processed by using an amplifier that also allowed to minimize the effect of the quantization noise due to the analog to digital converter [50], increasing the sensitivity of optical lever used above. The analysis of all the source noise is shown in figure4.18. Where we have changed respect to the lever in air, the power $P = 0.129\ 10^{-}3$ mW and the optical magnification $OM = B/A \sim 4.67$. We computed the total factor conversion of lever F= 1.33 mm/V which was enough in agreement with the measure one $F_m = 1.36$, the little disagreement is due to the indetermination on OM;

The measurements were performed at fixed distance between the actuator and test mass of $d = 2.5$ mm, using a fixed bias $A_{DC} = 50$ V^2, that corresponds to a force equal to the half of the maximum force for the given output range of the HV amplifier. The used excitation frequency was namely 0.1 Hz that is far enough from f_0 to allow us to neglect the transfer function details around the resonance (pole) of the suspended mass. For the measurements in DC bias, also the sign of the voltage applied to the HV amplifier

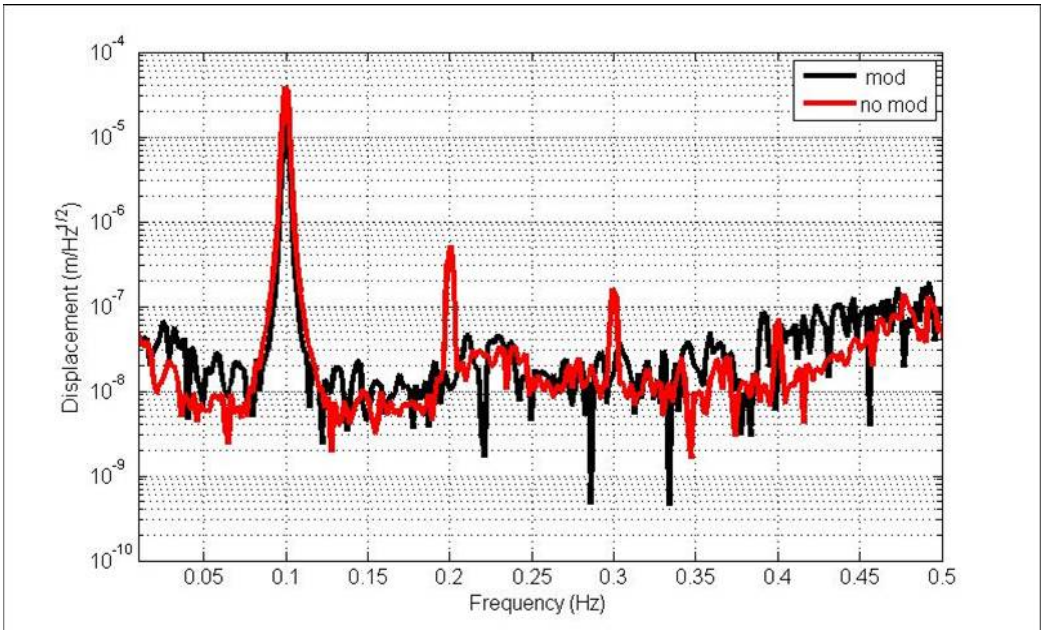

Figure 4.19: Spectra of the mass displacement with and without modulation. The presence of multiple harmonics, in case of DC bias is evident.

was changed to enhance the effects due to the stray charges on the mass, following the suggestions given in [48]. This change can be formally taken into account by changing the sign of G in equation (4.7). A change in the electrostatic force should arise only in the case $\beta \neq 0$ and $\omega_M = 0$.
The analysis of displacement spectra in DC bias conditions, show additional lines placed at multiple frequency respect to the one injected by the signal. These lines disappear if the measurement is performed in AC bias as shown in figure 4.19. Thanks to this behavior, the chosen form of the driving, allows to easily detect the presence of charges on the test mass, simply by looking for the harmonics of the injected line. In figure 4.20 the measured displacements ratio between the 2^{nd} and 1^{st} harmonics (upper graph) and the 3^{rd} and 1^{st} harmonics (lower graph) are reported as a function of the voltage V_{AC}. The measurements were done both for positive and negative G. The comparison with the model, based on the expression (4.22) is also given: $R_i = c_i/c_1$. The large error do not allow to state any definite conclusion, but the measurements largely follow the model. The next step could be to

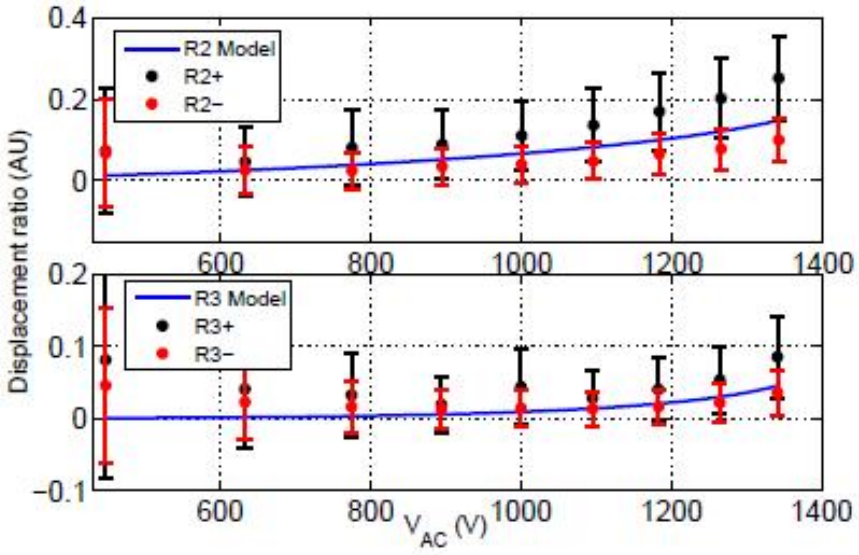

Figure 4.20: Ratios of the displacement harmonics compared with the model.

perform interferometric measurement to quantitatively analyze the spurious charge contribution.

4.5 Characterization of Actuation force in high vacuum

Equation (4.22) also foresees a contribution on the fundamental frequency. We have characterized the actuation force in vacuum by comparing the results obtained with DC bias conditions and AC modulated bias conditions. Two excitation frequencies were used, namely 0.1 Hz and 20 Hz, that are both far enough from f_0 . For each frequency a set of excitation amplitudes A_{AC}, in the range $5 \div 45$ V^2 were used. All the measurements were repeated in DC bias ($f_M = 0$) and alternate bias ($f_M = 100$ Hz) conditions.
The measurements performed at $f = 0.1$ Hz and d=3.5 mm are shown in figure 4.21. The filled dots represent the force measured in AC bias, both with positive or negative G, while the open circles are the force measured in DC bias with different G sign. The deviation from the foreseen behavior,

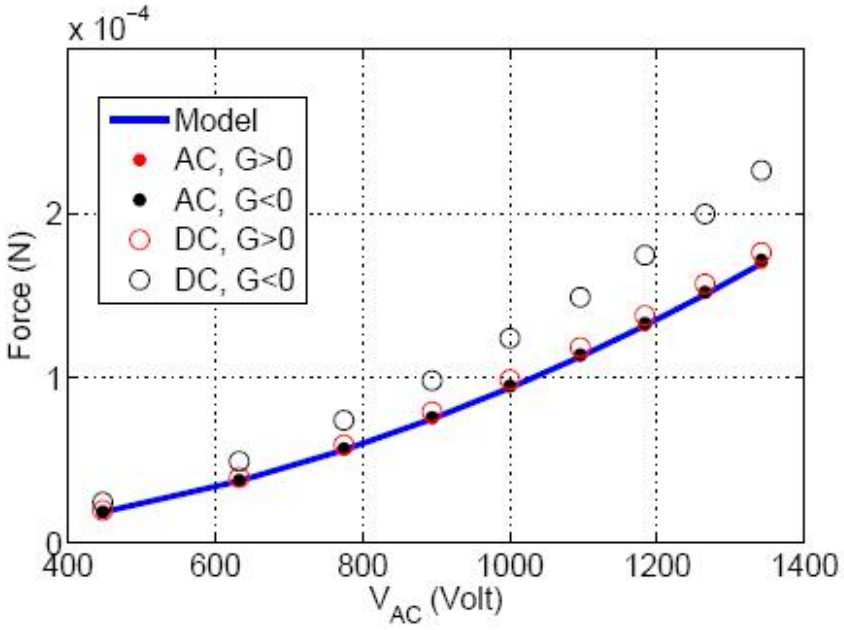

Figure 4.21: Comparison between the model and the force measured, in different bias conditions, for a excitation with f = 0.1 Hz.

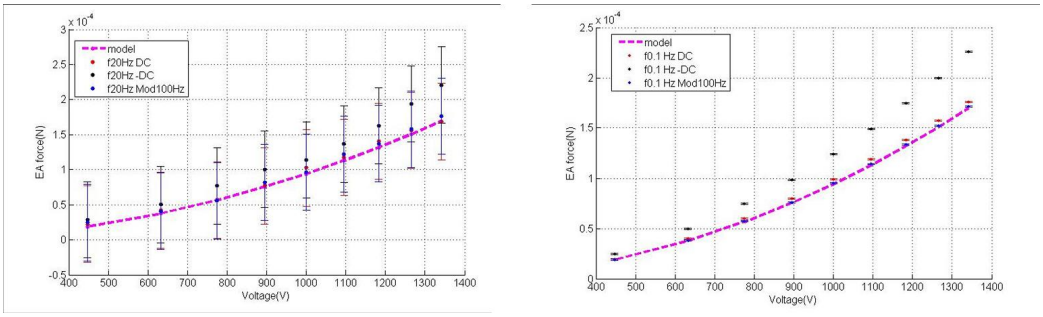

Figure 4.22: Measure of the EA force for different driving amplitudes with and without modulation. The comparison with a numerical model is also reported. at 20 Hz and at 0.1Hz (d=2.5mm)

clearly visible for all the points in DC bias, in particular in the case of negative G, is due to the presence of spurious charges on the dielectric suspended mass.
The two opposite polarizations, for the AC bias, give instead the same results, as the experimental measurements are practically overlapped. This confirms the effectiveness of the alternate bias technique that is insensitive to any static stray charge present on the test mass. It is important to stess that the points reported in figure 4.21, representing the measurements in AC bias, were multiplied by a factor 2 to take into account the presence of the modulation at ω_M that introduce a factor 1/2 in the force expression (eq. 4.14). In this way it is possible to compare the two different bias condition on a single graph. Of course all the measurements were performed in the same run, without opening the vacuum chamber to not intentionally change the charge distribution on the test mass.

Similar result were obtained also for the $f = 20$ Hz excitation, but in this case the measurements were affected by a larger error, caused by the suspension filter, the resulting displacement, at 20 Hz, is not very large respect to the noise floor and the final error on the force estimation is of the order of 20% making very difficult to decide if the points follow the model or not (see fig.4.22).
Finally we report all measurements in different conditions on the same graph

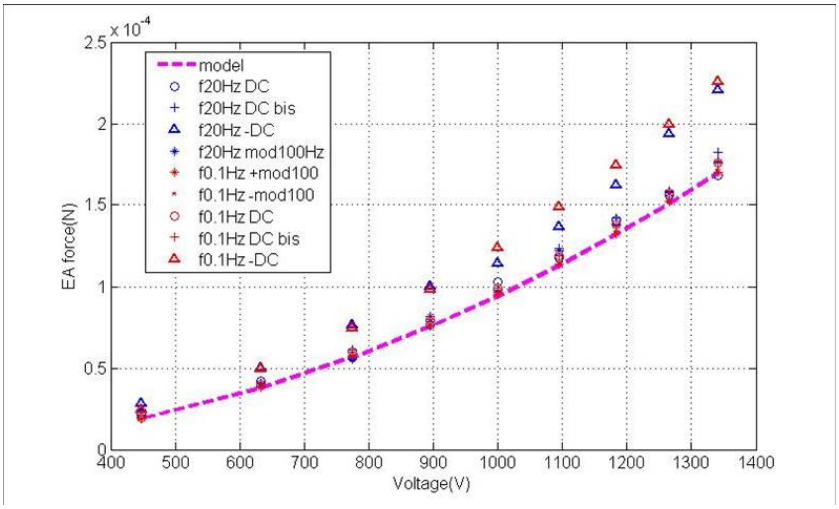

Figure 4.23: Measurements of force in vacuum at z=2.5mm, in AC bias modulated and in DC bias

4.23 with d=2.5mm, and can conclude that measurements made in DC bias given different result also with the same measure conditions, because the stray charge on attach the mass continuously changes. Instead the measurement in AC modulated bias are totally free by this problem.

Following the (4.22) a larger disagreement would be expected also for the case of DC bias with positive G, but one should consider that the description of the electrical field between the EA and the test mass is very roughly approximated in the model; more investigations are need in this direction which also require some upgrade in the experimental set-up, as the possibility to change the distance between the EA and the test mass without opening the chamber and changing, in this way, the amount of charges on the mass.

4.6 Applications and next steps

in order to verify the possibility to use the electrostatic actuator to lock an multipendular suspended interferometer we have tested the EA with the interferometer shown in figure.4.24.
The first arm optics are mounted on the lower stage of a double pendulum suspension. The position of its upper stage is controlled using coils-magnet

system . The end mirror is suspended by a double pendulum suspension and on the lower stage we use the electrostatic actuator to control the mirror longitudinal motion.

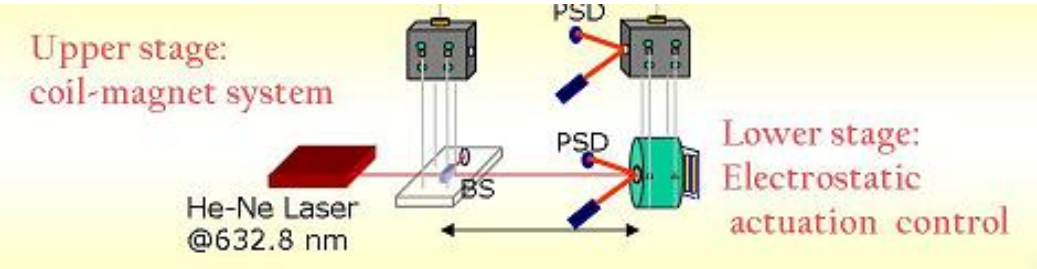

Figure 4.24: Basic scheme of the suspended interferometer

In particular the control of the interferometer was, conceptually and practically, divided in two part. The first issue was the damping and the positioning of the suspended elements, namely the bench and the mirror. This was performed by using a VME based digital control system, able to manage the high number of analog inputs coming from the optical sensing system of the two suspensions. Once the damping was performed, the interferometer was manually aligned by acting on the reference values of the control loops, in order to maximize the contrast.

Finally the interferometer is locked by acting on the suspended mirror with the electrostatic actuator.

The next step will be to test a new EA, designed and realized for an ultra low frequency suspension that the Virgo Napoli group have developed fig.4.26 in the last years. The new actuator have the electrodes composed by four patterns in order to actuate tilt and translation on the test mass, for aligning and locking purpose.

The test with ULF will allow as to investigate and possibly to solve other problems linked to use EA in advanced GW interferometers.

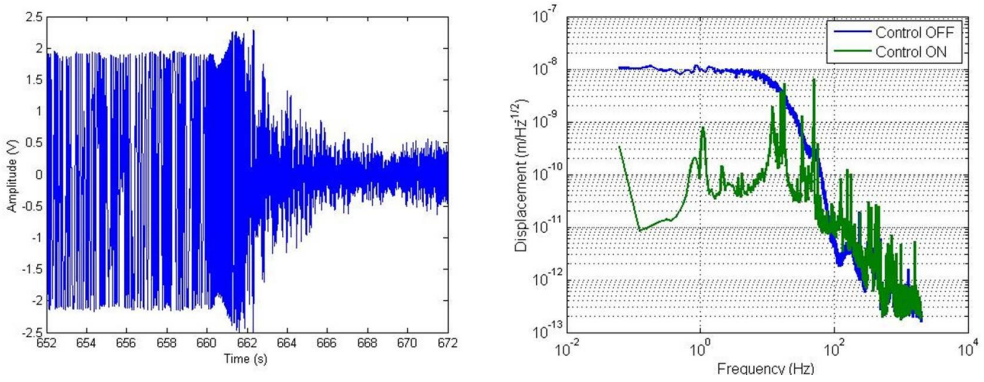

Figure 4.25: displacement and displacement spectral density of the residual relative motion between the interferometer arms.

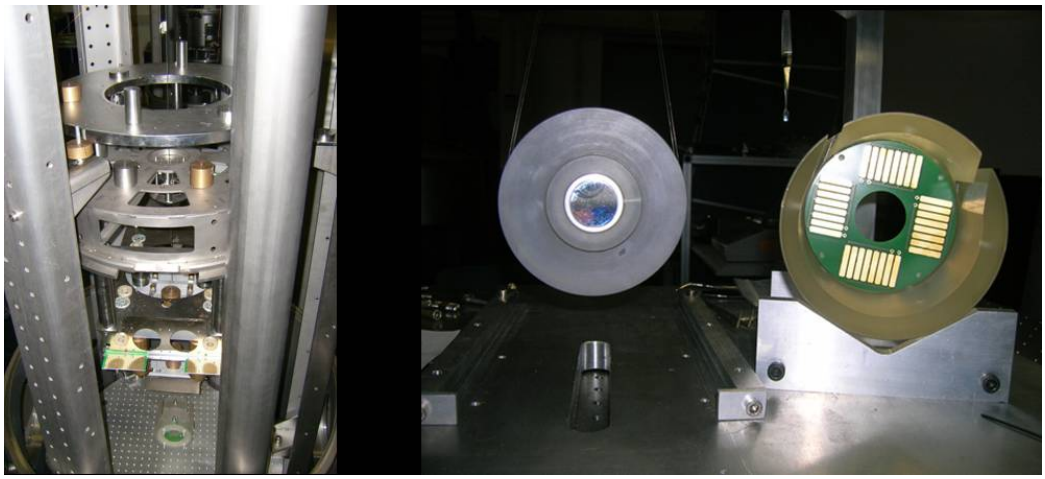

Figure 4.26: Detail of mirror suspension and picture of test mass with the new electrostatic actuator .

Conclusions

The work developed during this thesis was mainly devoted to correctly face and try to find suitable solutions for problems expected in upgrading the current interferometric detectors for gravitational waves detection, in particular for the Virgo+ detector.

Two particular topics were be analyzed.

The first one is related the use of high power laser as source light for the interferometer. The use of high power is the simplest way to reduce the shot noise limit in the detection, at high frequencies. Nevertheless very high powers are expected to induce not negligible effects in the input optics of the interferometer. These effect were investigated using different techniques on an experimental prototype of the input optics system of Virgo+, and suitable solutions were individuated. One of the results of this investigations was also implemented on the Virgo+ interferometer, resulting in an increasing of the injection system stability.

During the experimental activity also unexpected effects were found, in particular the spin to orbital momentum conversion of the light crossing the Faraday isolator, due to thermal effect induced by the laser power. This last effect was also studied and modeled, trough an wave front and a tomographic analysis of beam, allowing to theoretically explain a compensation system whose effectiveness was checked for 100 W of power in previous works, but without any theoretical explanation. In this way the tools were supplied to optimize this compensation also for higher powers. The experimental development and the characterization of such compensator will be part of the future activities foreseen by this work.

The second topics, instead, is related to the design and characterization of an alternative actuation technique for the last suspended stage of the pen-

dular chain used to isolate the test masses from the ground motion, namely the interferometer mirrors. The proposed actuation system is based on the use of a simple electrostatic actuator, that allows to reduce the control noise and the thermal noise of the mirrors thanks to its intrinsic characteristics. Nevertheless also this actuator suffers of some drawback, in particular its sensitivity to stray charge that could be present on the test mass.

The reduce this problem an alternative driving technique for such actuators was developed and tested on different experimental set-up, both in air and in vacuum environment, aimed to allow a full characterization of such driving systems. Also an effective and simple method to measure the contamination of the test masses, in term of spurious electric charges, was developed.

The next steps, for this topic, will be the set-up of a more sensitive device, placed under vacuum, for the actuator characterization, together with a compensation system to reduce the stray charges on the test mass by using the method here developed.

Appendix A

Intensity distribution of transverse mode

Transverse modes are defined by the designation TEM_{mn} for cartesian coordinate. The integers m and n represent the number of nodes or zeros of intensity transverse to the beam axis in the vertical and horizontal direction. In cylindrical coordinates the modes are labeled TEM_{pl} and are characterized by the number of radial nodes p and angular nodes l. The higher the values of m, n, p, and l, the higher the mode order. The lowest-order mode is the TEM_{00} mode, which has Gaussian-like intensity profile with its maximum on the beam axis. Modes with subscripts of 1 or more, intensity maxima, occur in off-axis position in a symmetrical pattern. To determine the location and amplitudes of the peaks and nodes, it is necessary to employ higher-order expressions which either involve Hermite or Laguerre polynomials. The Hermite polynomials are used when working with rectangular coordinates while Laguerre polynomials are more convenient when working with cylindrical coordinates. In cylindrical coordinates, the radial intensity distribution of allowable circularly symmetric TEM_{pl} mode is given by the expression

$$I_{pl}(r, \phi, z) = I_0 \rho^l [L_p^l \rho]^2 (cos^2 l\phi) e^{-\rho} \tag{4.23}$$

with $\rho = \frac{2r^2(z)}{w^2(z)}$, where z is the propagation direction of the beam, and r, Φ are the polar coordinates in a plane transverse to the beam direction. The radial intensity distributions are normalized to the spot size of Gaussian profile; that is, w(z) is the spot size of the Gaussian beam, defined as the radius at which the intensity of the TEM_{00} mode is $1/e^2$ of its peak value on the axis.L_p is the generalized Laguerre polynomial of order p and index l. The intensity distribution given in 4.23 is the product of a radial part and an angular part. For modes with l=0 (i.e., TEM_{p0}), the angular dependence

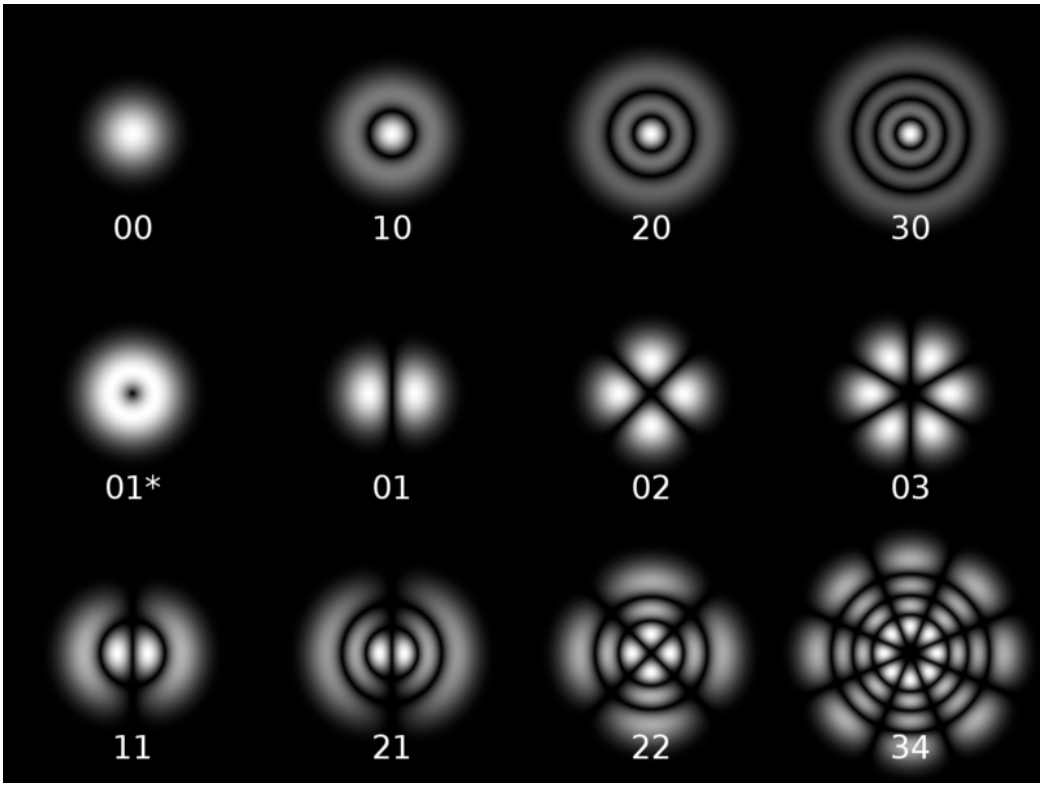

Figure 4.27: Examples of cylindrical transverse mode pattern. For cylindrical modes, the first subscript indicates the number of dark rings, whereas the second subscript indicates the number of dark bars across the pattern.

drops out and the mode pattern contains p dark concentric rings, each ring corresponding to a zero of Lp^0(p). The radial intensity distribution decay due to the factor $exp^{-\rho}$. The center of a pl mode will be bright if $l = 0$, but dark otherwise because of the factor p^l. These mode, besides having p zeros in the radial direction, also have $2l$ nodes in azimuth.

The only change in a (pl) mode distribution comes through the dependence of the spot size w(z) on the axial position z. However, the modes preserve the general shape of their electric field distributions for all values of z. As w increases with z, the transverse dimension increase so that the size of the mode patterns stay in constant ratio to each other. From the eq.(4.23) it is possible to determine any beam mode profile. Figure 4.23 show various cylindrical transverse intensity pattern. Note that the area occupied by a

mode increases with the mode number. A mode designation accompanied by an asterisk indicates that it is a linear superposition of two like modes, one rotated at 90 degrees the axis relative to the order. For example, the TEM mode designated 01^* is obtain of two TEM_{01} modes. The intensity distribution of the modes shown in Figure 4.23 can be calculated if we introduce the appropriate Laguerre polynomials into 4.23, i.e.,

$$L_0^l(\rho) = 1; \quad L_1^0(\rho) = (1-\rho); \quad L_2^0(\rho) = 1 - 2\rho + \frac{1}{2}\rho^2 \tag{4.24}$$

in rectangular coordinates the intensity distributions of a (m,n) mode is given by

$$I_{mn}(x,y,z) = I_0\big[H_m\big[\frac{x(2)^{\frac{1}{2}}}{w(z)}\big]e^{\frac{-x^2}{w^2(z)}}\big]^2 \times \big[H_n\big[\frac{y(2)^{\frac{1}{2}}}{w(z)}\big]e^{\frac{-y^2}{w^2(z)}}\big]^2. \tag{4.25}$$

As before, w(z) is the spot size at which the transverse intensity decreases to $\frac{1}{e^2}$ of the peak intensity of the lowest-order mode. The function H_m (s) is the m^{th} order Hermite polynomial, for example,

$$H_0 = 1; \quad H_1(s) = 2s; \quad H_2(s) = 4s^2 - 2. \tag{4.26}$$

At given axial position z, the intensity distribution consists of the product of a function of x alone and a function of y alone. The intensity pattern of rectangular transverse modes are shown in figure 4.28 The m, n values of a single spatial mode can be determined by counting the number of dark bars crossing the pattern in the x and y direction. Note that the fundamental mode (m=n=0) in this geometry is identical with the fundamental mode in cylindrical geometry.

An other important class of paraxial wave modes is expressed in the polar coordinate in which its complex amplitude is proportional to confluent Hypergeometric function (see Appendix D). These modes have a singular phase profile and are eigenfunctions of the photon orbital angular momentum (OAM). The intensity profile is characterized by a single brilliant ring with a singularity at its center, where the field amplitude vanish (see fig4.29)

$$I_{pm}(\rho,\Phi,\zeta) = \sqrt{\frac{2^{p+|m|+1}}{\pi\Gamma(p+|m|+1)}}\frac{\Gamma(1+|m|+\frac{p}{2})}{\Gamma(|m|+1)}$$

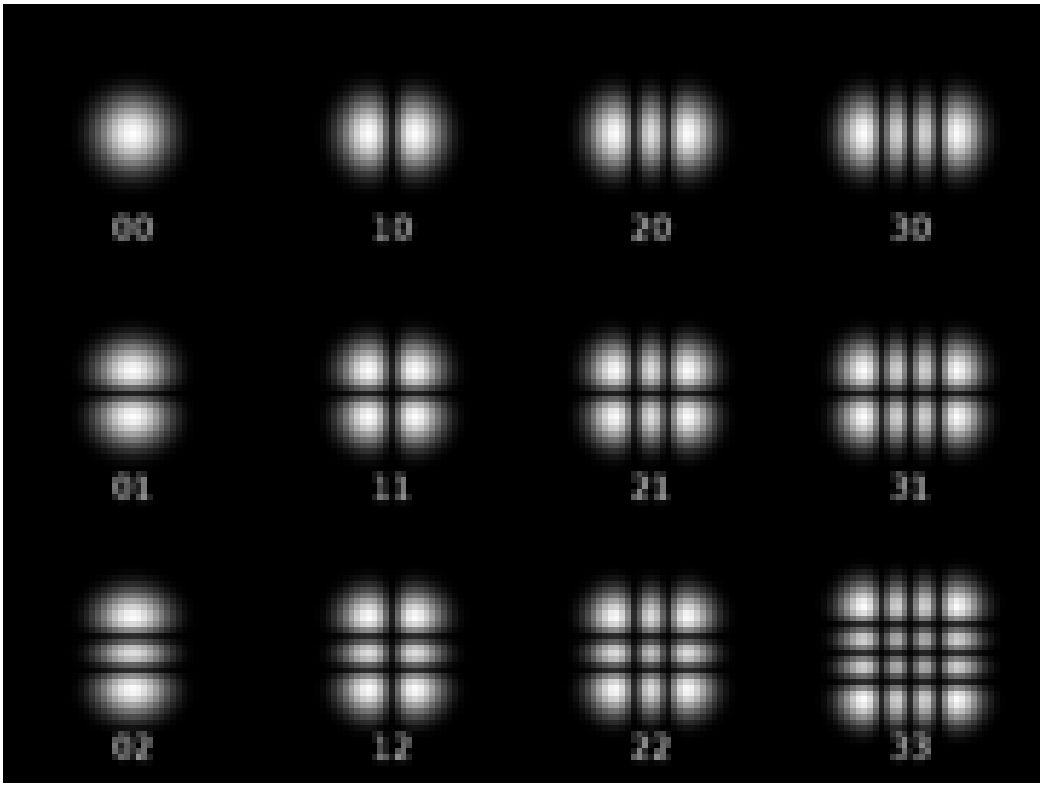

Figure 4.28: Examples of rettangular transverse mode pattern. For rectangular patterns, the two subscripts give the number of dark bars in the x and y direction

$$i^{|m|+1}\zeta^{\frac{p}{2}}(\zeta+i)^{(-1+|m|+\frac{p}{2})}\rho^{|m|}e^{-\frac{i\rho^2}{(\zeta+i)}}e^{im\phi}$$
$${}_1F_1\big(-\tfrac{p}{2},|m|+1;\tfrac{r^2}{\zeta(\zeta+i)}\big),$$

where m is integer, $p \geq -|m|$ is real value, $\Gamma(x)$ is the gamma function, $\zeta(z)$ and ${}_1F_1(a,b;c)$ is a confluent hypergeometric function (Appendice D). The Hypergeometric-Gaussian beam (HyGG) modes is overcomplete and it is not an orthogonal set of modes [36].
In the plane they have a simple profile:

$$I(\rho,\Phi,0) = I_0\rho^{p+|m|}e^{-\rho^2+im\Phi}. \tag{4.27}$$

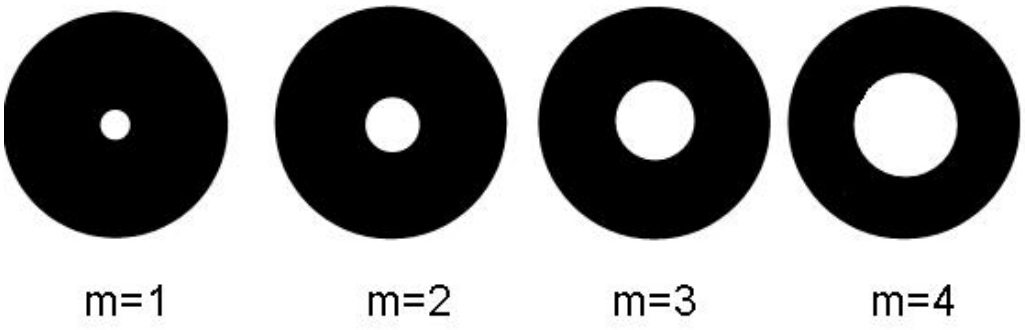

Figure 4.29: Intensity profile of Hypergeometric modes

Appendix B

Light Propagation in an Anisotropic Medium

Anisotropic crystal and Optical indicatrix

An important characteristic of crystals is that many of their properties depend on the crystals direction, that is crystal are generally anisotropic. The dielectric constant ϵ_r, depends on electronic polarization which involves the displacement of electrons with respect to positive atomic nuclei. Electronic polarization depends on the crystal direction since as it easier to displace electrons along certain crystal directions. This means that the refractive index n of a crystal depends on the direction of the electric field in the propagating light beam. Consequently, the velocity of light in a crystal depends on the direction of propagation and on the state of its polarization, i.e. the direction of the electric field. Most noncrystalline material such as glasses and liquids, and all cubic crystals are optically isotropic, that is the refractive index is the same in all direction. For all classes of crystal excluding cubic structures, the refractive index depends on the propagation direction and the state of polarization. The result of optical anisotropy is that, except along certain special directions, any unpolarized light ray entering such a crystal breaks into two different rays with different polarizations and phase velocities. When we see an image through a calcite crystal, an optically anisotropic crystal, we see two images, each constituted by light of different polarization passing through the crystal, whereas there is only one image through an optically isotropic crystal. Optically anisotropic crystals are called birefringent because an incident light beam may be doubly refracted. Experiment and theories on "most anisotropic crystals", i.e. those with the highest degree of anisotropy, show that we can describe light propagation in terms of three re-

fractive indices, called principal refractive indices n_1 , n_2 and n_3 , along three mutually orthogonal direction in the crystal, say x,y and x called principal axes. These indices correspond to the polarization state of the wave along these axes. Crystal that have three distinct principal indices also have two optic axes and are called biaxial crystal. On the other hand, uniaxial crystal have two of their principal indices the same ($n_1 = n_2$) and only have one optic axis. Uniaxial crystal, such as quartz, that have $n_3 > n_1$ and are called positive, and those such as calcite that have $n_3 < n_1$ are called negative uniaxial crystal. The refractive index associated with a particular EM wave in a crystal can be determined by using Fresnel's refractive index ellipsoid, called the optical indicatrix, which is a refractive index surface placed in the center of the principal axes where x,y and z axis intercepts are n_1 , n_2 , and n_3 . If all three indices were the same, $n_1 = n_2 = n_3 = n_0$ we would have a spherical surface and all electric field polarization direction would experience the same refractive index, n_0 . Such a spherical surface would represent an optically isotropic crystal. For positive uniaxial crystals such as quartz $n_1 = n_2 < n_3$.

Optical activity and circular birefringence

When a linearly polarized light wave is passed trough a quartz crystal along its optic axis, it is observed that the emerging wave has the E-vector (plane of polarization) rotated. This rotation increases continuously with the distance traveled through the crystal (about 21.7^0 per mm of quartz). The rotation of the plane of polarization by a substance is called optical activity. In very simply intuitive terms, optical activity occurs in materials in which the electron motions induced by the external electromagnetic field follow spiraling of helical paths (orbits). Electron flowing in helical paths resemble a current flowing in a coil and thus possess a magnetic moment.The optical field in light therefore induces oscillating magnetic moments which can be either parallel or antiparallel to the oscillating electric dipoles. Wavelets emitted from these oscillating induced magnetic and electric dipoles to interfere and constitute a forward wave that has its optical field rotated either clockwise or counterclockwise. If Φ is the angle of rotation of E, then Φ is proportional to the distance L propagated in the optically active medium. For an

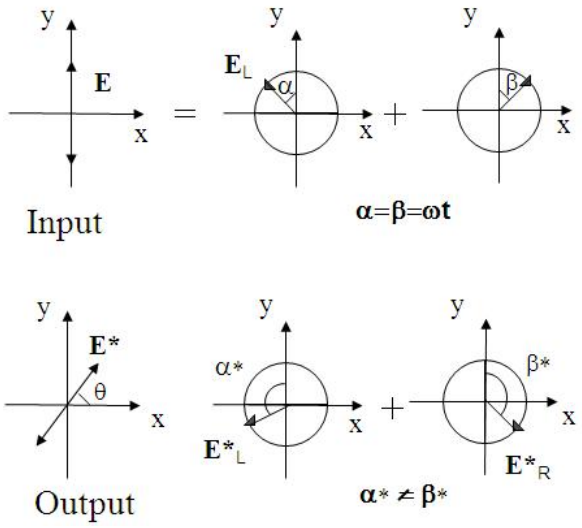

Figure 4.30: Vertically polarized wave at the input can be thought of as two right and left handed circularly polarized waves that are symmetrical, i.e. at any instant $\alpha = \beta$. If these travel a different velocities through a medium then at the output they are non longer symmetric with respect y $\alpha \neq \beta$, and the result is a vector E^2 at the angle o to y

observer receiving the wave through quartz, the rotation of the plane of polarization may be clockwise (to the right) or counterclockwise (to the left) which are called dextrorotatory and levorotatory forms of optical activity. The structure of quartz is such that atomic arrangements spiral around the optic axis either in clockwise or counterclockwise sense. Quarts thus occurs in two distinct crystalline forms, righ-handed and lef-handed, which exhibit dextrorotatory and levorotatory types of optical activity respectively. Although we used quartz as an example, there are many substances that are optically active, including various biological substances and even some liquid solution (e.g. corn syrup) that contain various organic molecules with a rotatory power.

The specific rotatory power (θ/L)is defined as the extent of rotation per unit length of distance traveled in the optically active substance. Optical activity can be understood in terms of left and right circularly polarized waves traveling at different velocities in the crystal, i.e. experiencing different refractive indices. Due to the helical twisting of the molecular or atomic arrangements

in the crystal, the velocity of a circularly polarized wave depends whether the optical field rotates clockwise or counterclockwise. A vertically polarize light with a field E at the input can be thought of as two right and left handed circularly polarized waves, EL and EB , that are symmetrical with respect to the y-axis, i.e. at any instant $\alpha = \beta$, as shown in Figure 4.30. If they travel at the same velocity through the crystal then they remain symmetrical with respect to the vertical ($\alpha = \beta$ remain the same) and the resultant is still a vertically polarized light. If however these travel ad different velocities through a medium then at the output E_L and E_B are no longer symmetrical with respect to the vertical $\alpha' \neq \beta'$ and their resultant is a vector E_B at an angle θ to y-axis. Suppose that n_r and n_l are the refractive indices experienced by the right and left circularly polarized light respectively. After traversing the crystal length L, the phase difference between the two optical fields E'_L and E'_R at the output leads to a new optical field E' that is E rotated by θ, given by

$$\theta = \frac{\pi}{\lambda}(n_R - n_L)L \tag{4.28}$$

where λ is the free-space wavelength.
In a circularly birefringent medium, the right and left handed circularly polarized waves propagate with different velocities and experience different refractive indices n_R and n_L. Since optically active materials naturally rotate the optical field, it is not unreasonable to expect that a circularly polarized light, with its optical field rotating in the same way sense as the optical activity will find it easier to travel through the medium. Thus, an optically active medium possesses different indices for right and left circularly polarized light and exhibits circular birefringence. It should be mentioned that if the direction of the light wave is reversed in Figure 7.17, the ray simply retraces itself and $E'1$ becomes E.

When an optical inactive material such as glass is placed in a strong magnetic field and then a plane polarized light is sent along the direction of the magnetic field, is is found that the emerging light s plane of polarization has been rotated. This is called the **Faraday effect** as originally observed by Michael Faraday 1845. It seems to appear that an "optical activity" has been induced by the application of the strong magnetic field. There is however an

important distinction between the natural optical activity and the faraday effect. The sense of rotation θ in the Faraday effect, for a given material depends only on the direction of the magnetic $\mathbf{B}$. If θ is positive, for light propagating parallel to $\mathbf{B}$, the optical field $\mathbf{E}$ rotates in the same sense as an advancing right-handed screw pointing in the direction of $\mathbf{B}$. The direction of light propagation, does not change the absolute sense of rotation of θ. If we reflect the wave to pass through the medium again, the rotation increases to 2θ.

Appendix C

Expansion in power of DC bias signal

Let us suppose to apply a single frequency signal to the Electrostatic Actuator with square amplitude A_{AC}, frequency $2\pi\omega$, by using a bias square amplitude A_{DC}.

In this case the linearized signal has of the following form:

$$V = \sqrt{A_{DC} + A_{AC}\cos\omega t} \tag{4.29}$$

Now, by denoting with α the coupling constant with the electrostatic force, and by β the coupling constant of the force due to the stray charges present on the test mass, the total force exerted on the mass is:

$$F = \alpha V^2 + \beta V = \alpha(A_{DC} + A_{AC}\cos\omega t) + \beta\sqrt{A_{DC} + A_{AC}\cos\omega t} \tag{4.30}$$

The first term, apart from the DC bias, consists of a signal at fixed frequency $2\pi\omega$, while the second term requires some special attention. Since the applied signal is strictly lower than the bias, one can write the second term of the (4.30) as:

$$\sqrt{A_{DC} + A_{AC}\cos\omega t} = \gamma\sqrt{1 + a\cos\omega t} \tag{4.31}$$

being $\gamma = \sqrt{A_{DC}}$ and $a = A_{AC}/A_{DC} < 1$. The square root can be expanded in power series around $a = 0$, obtaining:

$$\sqrt{1 + a\cos\omega t} = \sum_{n=0}^{+\infty} \frac{(-1)^n}{n!}\left(-\frac{1}{2}\right)_n a^n \cos^n \omega t \tag{4.32}$$

where:

$$(m)_n = \frac{\Gamma(m+n)}{\Gamma(m)} \tag{4.33}$$

is the Pochhammer symbol. The (4.32) series contains integer powers of the cosine that can be written as:

$$\cos^{2n+1}\omega t = \frac{1}{2^{2n}}\sum_{k=0}^{n}\binom{2n+1}{k}\cos(2n-2k+1)\omega t \tag{4.34}$$

for odd powers and as:

$$\cos^{2n}\omega t = \frac{1}{2^{2n}}\binom{2n}{n} + \frac{1}{2^{2n-1}}\sum_{k=0}^{n-1}\binom{2n}{k}\cos(2n-2k)\omega t \tag{4.35}$$

for even powers. In the last equation the first term is the DC part of an even power of a sinusoidal signal. By writing (4.32) by separating even and odd values of n:

$$\begin{aligned}\sqrt{1+a\cos\omega t} = &\sum_{n=0}^{+\infty}\frac{(-1)^{2n}}{(2n)!}\left(-\frac{1}{2}\right)_{2n}a^{2n}\cos^{2n}\omega t + \\ &\sum_{n=0}^{+\infty}\frac{(-1)^{2n+1}}{(2n+1)!}\left(-\frac{1}{2}\right)_{2n+1}a^{2n+1}\cos^{2n+1}\omega t\end{aligned} \tag{4.36}$$

and substituting the (4.34) and (4.35), it results:

$$\begin{aligned}\sqrt{1+a\cos\omega t} = &\sum_{n=0}^{+\infty}\frac{(-1)^{2n}}{(2n)!}\left(-\frac{1}{2}\right)_{2n}\frac{a^{2n}}{2^{2n}}\binom{2n}{n} + \\ &\sum_{n=1}^{+\infty}\frac{(-1)^{2n}}{(2n)!}\left(-\frac{1}{2}\right)_{2n}\frac{a^{2n}}{2^{2n-1}}\sum_{k=0}^{n-1}\binom{2n}{k}\cos(2n-2k)\omega t + \\ &\sum_{n=0}^{+\infty}\frac{(-1)^{2n+1}}{(2n+1)!}\left(-\frac{1}{2}\right)_{2n+1}\frac{a^{2n+1}}{2^{2n}}\sum_{k=0}^{n}\binom{2n+1}{k}\cos(2n-2k+1)\omega t\end{aligned} \tag{4.37}$$

Now, by substituting $n \to n+1$ in the second line of (4.37), one obtains:

$$\begin{aligned}\sqrt{1+a\cos\omega t} = &\sum_{n=0}^{+\infty}\frac{(-1)^{2n}}{(2n)!}\left(-\frac{1}{2}\right)_{2n}\frac{a^{2n}}{2^{2n}}\binom{2n}{n} + \\ &\sum_{n=0}^{+\infty}\frac{(-1)^{2n+2}}{(2n+2)!}\left(-\frac{1}{2}\right)_{2n+2}\frac{a^{2n+2}}{2^{2n+1}}\sum_{k=0}^{n}\binom{2n+2}{k}\cos(2n-2k+2)\omega t + \\ &\sum_{n=0}^{+\infty}\frac{(-1)^{2n+1}}{(2n+1)!}\left(-\frac{1}{2}\right)_{2n+1}\frac{a^{2n+1}}{2^{2n}}\sum_{k=0}^{n}\binom{2n+1}{k}\cos(2n-2k+1)\omega t\end{aligned} \tag{4.38}$$

The expression (4.38) only contains terms in the form:

$$\sqrt{1 + a\cos\omega t} = \sum_{m=0}^{+\infty} c(m)\cos m\omega t \tag{4.39}$$

hence, by using the Fourier series, it can be wroten as:

$$\sqrt{1 + a\cos\omega t} = c_0 + 2\sum_{l=1}^{+\infty} c_l \cos l\omega t \tag{4.40}$$

where:

$$c_l = \frac{\omega}{2\pi}\int_0^{2\pi/\omega} c(m)\cos m\omega t\cos l\omega t\mathrm{d}t = \begin{cases} \frac{1}{2}c(m)\delta_{lm} & \text{for } l \neq 0 \\ \\ c(m)\delta_{0m} & \text{for } l = 0 \end{cases} \tag{4.41}$$

By replacing the right expressions of $c(m)$, it results:

$$c_0 = \sum_{n=0}^{+\infty} \frac{(-1)^{2n}}{(2n)!}\left(-\frac{1}{2}\right)_{2n}\frac{a^{2n}}{2^{2n}}\binom{2n}{n} \quad (m = 0) \tag{4.42}$$

$$c_m = \frac{1}{2}\sum_{n=\frac{m}{2}-1}^{+\infty} \frac{(-1)^{2n+2}}{(2n+2)!}\left(-\frac{1}{2}\right)_{2n+2}\frac{a^{2n+2}}{2^{2n+1}}\sum_{k=0}^{n}\binom{2n+2}{k}\delta_{2n-2k+2,m} \quad (\text{even } m) \tag{4.43}$$

$$c_m = \frac{1}{2}\sum_{n=\frac{m}{2}-\frac{1}{2}}^{+\infty} \frac{(-1)^{2n+1}}{(2n+1)!}\left(-\frac{1}{2}\right)_{2n+1}\frac{a^{2n+1}}{2^{2n}}\sum_{k=0}^{n}\binom{2n+1}{k}\delta_{2n-2k+1,m} \quad (\text{odd } m) \tag{4.44}$$

The first summations in the last two lines do not start from zero since the m^{th} harmonics of the $2\pi\omega$ signal are only present for powers $n \geq m$. The second summation, in the same lines, can be removed by using the constraint on the values of k given by the δ symbol:

$$c_m = \frac{1}{2}\sum_{n=\frac{m}{2}-1}^{+\infty} \frac{(-1)^{2n+2}}{(2n+2)!}\left(-\frac{1}{2}\right)_{2n+2}\frac{a^{2n+2}}{2^{2n+1}}\binom{2n+2}{n-\frac{m}{2}+1} \quad (\text{even } m) \tag{4.45}$$

$$c_m = \frac{1}{2}\sum_{n=\frac{m}{2}-\frac{1}{2}}^{+\infty} \frac{(-1)^{2n+1}}{(2n+1)!}\left(-\frac{1}{2}\right)_{2n+1}\frac{a^{2n+1}}{2^{2n}}\binom{2n+1}{n-\frac{m}{2}+\frac{1}{2}} \quad (\text{odd } m) \tag{4.46}$$

Now, by making the substitutions $n \to n + m/2 - 1$ in the equation (4.45) and $n \to n + m/2 - 1/2$ in the equation (4.46) the c_m Fourier coefficients

read:

$$c_m = \frac{1}{2}\sum_{n=0}^{+\infty}\frac{(-1)^{2n+m}}{(2n+m)!}\left(-\frac{1}{2}\right)_{2n+m}\frac{a^{2n+m}}{2^{2n+m-1}}\binom{2n+m}{n} \text{ (even } m) \quad (4.47)$$

$$c_m = \frac{1}{2}\sum_{n=0}^{+\infty}\frac{(-1)^{2n+m}}{(2n+m)!}\left(-\frac{1}{2}\right)_{2n+m}\frac{a^{2n+m}}{2^{2n+m-1}}\binom{2n+m}{n} \text{ (odd } m) \quad (4.48)$$

The two expressions (4.47) and (4.48) now coincide and one can write, also including the case $m = 0$ (cfr equation 4.42):

$$c_m = \left(-\frac{a}{2}\right)^m\sum_{n=0}^{+\infty}\frac{1}{(2n+m)!}\left(-\frac{1}{2}\right)_{2n+m}\frac{a^{2n}}{2^{2n}}\binom{2n+m}{n} \quad (4.49)$$

By explicitly writing the binomial coefficient and by using the property: $n! = \Gamma(n+1)$ the (4.49) becomes:

$$c_m = \left(-\frac{a}{2}\right)^m\sum_{n=0}^{+\infty}\frac{1}{n!}\left(-\frac{1}{2}\right)_{2n+m}\frac{a^{2n}}{2^{2n}}\frac{1}{\Gamma(n+m+1)} \quad (4.50)$$

The Pocchammer symbol has the following properties:

$$(2x)_{2n} = 4^n\,(x)_n\left(x+\frac{1}{2}\right)_n \quad (4.51)$$

$$(x)_{n+m} = (x)_m\,(x+m)_n \quad (4.52)$$

From equation (4.51) it follows:

$$\left(-\frac{1}{2}\right)_{2n+m} = 4^{n+m/2}\left(-\frac{1}{4}\right)_{n+m/2}\left(\frac{1}{4}\right)_{n+m/2} \quad (4.53)$$

Then the (4.52) gives:

$$\left(-\frac{1}{4}\right)_{n+m/2} = \left(-\frac{1}{4}\right)_{m/2}\left(\frac{m}{2}-\frac{1}{4}\right)_n \quad (4.54)$$

$$\left(\frac{1}{4}\right)_{n+m/2} = \left(\frac{1}{4}\right)_{m/2}\left(\frac{m}{2}+\frac{1}{4}\right)_n \quad (4.55)$$

By substituting the (4.54) and (4.53) in the (4.53) it results:

$$\left(-\frac{1}{2}\right)_{2n+m} = 2^{2n}\left(\frac{m}{2}-\frac{1}{4}\right)_n\left(\frac{m}{2}+\frac{1}{4}\right)_n 4^{m/2}\left(-\frac{1}{4}\right)_{m/2}\left(\frac{1}{4}\right)_{m/2} \quad (4.56)$$

But using the (4.51) on the last two terms it can be written as:

$$\left(-\frac{1}{2}\right)_{2n+m} = 2^{2n}\left(\frac{m}{2}-\frac{1}{4}\right)_n\left(\frac{m}{2}+\frac{1}{4}\right)_n\left(-\frac{1}{2}\right)_m \tag{4.57}$$

In this way the (4.50) becomes:

$$c_m = \left(-\frac{1}{2}\right)_m\left(-\frac{a}{2}\right)^m\sum_{n=0}^{+\infty}\frac{a^{2n}}{n!}\left(\frac{m}{2}-\frac{1}{4}\right)_n\left(\frac{m}{2}+\frac{1}{4}\right)_n\frac{1}{\Gamma(n+m+1)} \tag{4.58}$$

Now, by multiplying and dividing for $\Gamma(m+1)$ and recalling the (4.33), the previous expression becomes:

$$c_m = \frac{\left(-\frac{1}{2}\right)_m}{\Gamma(m+1)}\left(-\frac{a}{2}\right)^m\sum_{n=0}^{+\infty}\frac{a^{2n}}{n!}\frac{\left(\frac{m}{2}-\frac{1}{4}\right)_n\left(\frac{m}{2}+\frac{1}{4}\right)_n}{(m+1)_n} \tag{4.59}$$

Recalling the definition of the Gauss Hypergeometric function (see Appendix D):

$${}_2F_1(a,b,c,z) = \sum_{n=0}^{+\infty}\frac{z^n}{n!}\frac{(a)_m(b)_m}{(c)_m} \tag{4.60}$$

and the equality:

$$\left(-\frac{1}{2}\right)_m = \frac{\Gamma(m-\frac{1}{2})}{\Gamma(-\frac{1}{2})} = -\frac{\Gamma(m-\frac{1}{2})}{2\sqrt{\pi}} \tag{4.61}$$

the Fourier coefficients can be written in the final form:

$$c_m = -\frac{\Gamma(m-\frac{1}{2})}{2\sqrt{\pi}\Gamma(m+1)}\left(-\frac{a}{2}\right)^m{}_2F_1\left(\frac{m}{2}-\frac{1}{4},\frac{m}{2}+\frac{1}{4},m+1,a^2\right) \tag{4.62}$$

Appendix D

Generalized hypergeometric function

A generalized hypergeometric function ${}_pF_q(a_1, ..., a_p; b1, ...b_q; x)$ is a function which can be defined in the form of a hypergeometric series, i.e.,a series for which the ratio of successive terms can be written

$$\frac{C_{k+1}}{k} = \frac{P(k)}{Q(k)} = \frac{(k+a_1)(k+a_2)...(k+a_p)}{(k+b_1)(k+b_2)...(k+b_q)(k+1}x. \tag{4.63}$$

The function ${}_2F_1(a, b; c; x)$ corresponding to $p = 2$, $q = 1$ is know as Gauss's hypergeometric function. The hypergeometric functions are solutions to the hypergeometric differential equation, which has a regular singular point at the origin:

$$z(1-z)y'' + [c - (a+b+1)z]y' - aby = 0, \tag{4.64}$$

and have as solution:

$$\sum_{n=0}^{+\infty} \frac{(a)_n(b)_n}{(c)_n} \frac{z^n}{n} \tag{4.65}$$

Acknowledgements

I've got quite a list of people who contributed in some way to this thesis, people which I would like to thank

My supervisor Rosario De Rosa, for everything that he taught me every day and for all chance that he has given me to improve myself. A guide and reference point for me.

Prof. L. Milano, for encouragements and for the very special person he is. I was very lucky to meet him on my way.
Benjamin, for making possible any complicate optical set-up whit their brilliant ideas. I was very happy to work with him.

Prof. Santamato, for illuminating discussions about the spin to orbital conversion in TGG crystal.

Ebrahim, for the great help to tomographic analysis, and for clear explanation during train trips.

Eric, for kindness and his true interest at my work.

Prof. Marrucci, a perfect guide for us PhD students, for his suggestions about my work.

Prof. Aloisio for advices given with singleness and liking.

Bruno for helping me with computations of spin orbital conversion.

Guido Celentano, unique and irreplaceable presence for all physics students.

Fabio for availability to solve countless and varied problems and for being a nice tourist guide in New York City.

Luciano, for wisdom and good cheer that he gives all people he meets.

Prof. S. Capozziello for his teaching of cosmology.

Furthermore...

I would like to thank my lab mates , there are no adequate words to convey my appreciation for all of their support, but I will try:

Thanks to Maria, for the shown sincere friendship and for useful discussions.

to Gianluca for giving me many documents and books and helping me in a very practical way in the first year of this work.

to Luca my "physical" help of Mathematica and Latex and for many other things (especially for the help in this very moment...)

to Antonino who after four years has magically re-appeared on my way providing answers to all my useful and useless questions, always with patience and competence.

to Felicia for wise advise and encouragements.

to Iolanda for sincere friendship and for guiding me towards the beautiful experience of the PhD including the difficulties that waited me.

to sweet Adele for pleasant presence. And for teaching me that during life one needs bravery.

to Silvio for the very funny moments. And for always hearing me.

To Enrico, Julien, Saverio, Antonio Perreca, Fabrizio, Fausto, Paolino and all the Virgo people that I met in these years.

But I haven't finished yet...

I thank to all my friends, my buddy-buddy Maria D'Esposito, Antonio Setaro, Annalisa, Massimo, Elvio, Annalura, Peppe and the list should be very long.

I thank my family: my mother for instilling in me the love of knowledge and for very many other things.
To my sisters Sgiusi and Sara for their love and the practical support. To Francesco for his suggest as scientist and friend. to Nando for his massage when I was not well and for being a trusted friend. To Maria for preparing very good pre-cooked food for me.

To little Sofia for all her involving gaiety.

Finally I thank my love and true friend Ernesto, for practical and psychological support and for its example of will and determination.

Bibliography

[1] S. Weinberg, *Gravitation and cosmology*: principles and applications of the general theory of Relativity, john wiley-Sons, New York (1972).

[2] C.W. Misner, K.S. Thorne, J. Wheeler, *Gravitation*, W. H. Freeman, San Francisco (1973).

[3] C. Moller, *The theory of relativity*, Oxford University Press, New Delhi (1972).

[4] R.M. Wald, *General relativity*, The University of Chicago Press, Chicago, (1984).

[5] M.Maggiore, *Gravitational wave theory and expariments*, Oxford University Press, (2007).

[6] P. Saulson *Fundamentals of interforemetric gravitational wave detectors*, P. Saulson World Scientific (1994)

[7] J. Taylor "*Binary pulsar and relativistic gravity*", Rev. Mod. Phys. D 66 (1994) 699-710.

[8] R. Hulse "*The discovery of the binary pulsar*", Rev. Mod. Phys. D 66 (1994) 699-719

[9] B.F.Schutz, *Gravitational wave astronomy*, Class. Quantum Grav., 16 A131(1999).

[10] M.Maggiore *Gravitational Wave Experiments and Early Universe Cosmology*, arXiv:gr $\sim$ qc/99099001 v4 6 Feb 2000.

[11] The LIGO Scientific Collaboration and The Virgo Collaboration *An upper limit on the stochastic gravitational − wave background of cosmological origin*, Nature, Vol 460,20 August 2009 p.990.

[12] J.-Y. Vinet et al., *The Virgo Physics Book*, Vol II (2004) [http://wwwcascina.virgo.infn.it/vpb/]

[13] Callen and walton (1951)

[14] M. Punturo *The VIRGO sensitivity curve* VIRGO NOTE (2004)[http://wwwcascina.virgo.infn.it/vpb/]

[15] R.Drever et al. *laser Phase and frequency stabilization using an optical paramiter oscillator*. Appl. Phys. B, 31 (1983):97.

[16] S. Braccini et al., *Measurement of the seismic attenuation performance of the VIRGO superattenuator*, Astropart. Phys. 23 (2005) 557.

[17] G. Losurdo, *Ultra−low frequency inverted pendulum for the VIRGO testmass suspension*, Ph. D. thesis, Scuola Normale Superiore, Pisa (1998)

[18] M. Beccaria et al., *Extending the VIRGO gravitational wave detection band down to a few Hz: Metal blade springs and magnetic antisprings*, Nucl. Instrum. Meth. A 394 (1997) 397.

[19] F.Acernese et al. (Virgo Coll.), *A local control system for the test masses of the Virgo GW detector*, Astrop. Phys., 20 (2004) 617

[20] L. Barsotti for the VIRGO Collaboration, *The variable finesse locking technique*, *Proceedings of the 6th Amaldi conference*, Class. Quantum Grav. 23 No 8 (2006) S85- S89.

[21] F.Cavalier, *Le controle global de Virgo*, These dHabilitation a diriger des Recherches, Universit‘e de Paris Sud, LAL 01-69 (2001).

[22] D.Z.Anderson, *Alignment of resonant optical cavities*, Appl. Opt., 23, 2944-2949 (1984).

[23] M. Mantovani for the VIRGO Collaboration, The VIRGO automatic alignment system, Proceedings of the 6th Amaldi conference, Class. Quantum Grav. 23 No 8 (2006) S91-S101.

[24] F. Acernese, et al., *First lockingof theVirgo central area interferometer with suspension hierarchical control*, Astrop. Phys., 20 (6), 629-640 (2004).

[25] M. Lorenzini *Silicate bonding properties: investigation through thermal conductivity measurement* Poster section Amaldi8 New York (2009)

[26] http://wwwcascina.virgo.infn.it/DataAnalysis/Calibration/Sensitivity/index.html

[27] The Virgo collaboration *Advanced Virgo Baseline Design*

[28] F. Acernese et all. *The variable finesse locking technique* Class.Quantum Gravity (2006)

[29] EGO *RandD* Program CALVA ESPCI Paris, LAL Orsay, LAPP Annecy, LMA Lyon

[30] S. Hild, G. Losurdo and A. Freise: *Optimising the Advanced Virgo sensitivity for astrophysical sources*. Presentation at Virgo week July 2008. Available at http://wwwcascina.virgo.infn.it/collmeetings/presentations/2008/2008-07/AdV/hild 160708.ppt 11, 46

[31] M. Born and Wolf *Principles of optics*, seventh edition 2001

[32] A. Khazanov et al *Investigation of self induced depolarization of laser radiation in terbium gallium garnet* (1999)

[33] L.N. Soms and A.A. Tarasov, *Thermal deformation in color-center laser active elements* Theoty, Sov. J. Quantum Electron., vol.9, pp.1506-1508,1979

[34] N F Andreev et al. *A 45-dB Faraday isolator for 100-W average radiation power* (2000)

[35] L.Marrucci et al. *Optical Spin-to-Orbital Angular Momentum Conversion in Inhomogeneous Anisotropic Media* (2006)

[36] E. Karimi et al *Hypergeometric-Gaussian Modes, Optics Letters, (Vol 32) Page 3053 (2007).*

[37] E. Karimi et al *Light propagation in a birefringent plates with topological charge, Optics Letters* (Vol 34) Page 1225 (2009).

[38] E. Nagali et all *Quantum information transfer from spin to orbital angular momentum of photons* (2009)

[39] T. beth *Quantum information processing*

[40] Virgo collaboration *In-vacuum optical isolation changes by heating in a Faraday isolator*(2008)

[41] P.Amico et al. *Mechanical quality factor of mirror substrates for VIRGO*, Class. Quant. Grav. 19 (2002) 1663-1668

[42] I.Fiori et al. *Magnetic Noise Coupling, Noise Meeting*, 29 Sept 2005

[43] L Holloway, et al. *A coil system for virgo providing a uniform gradient magnet field*. Physics Letters A, 171:162166, 1992.

[44] Peter R. Saulson *Thermal noise in mechanical experiments* Phisical Review D, third series, volume 42, number 8 (1990).

[45] G. Losurdo for the Virgo Coll., *The inertial damping of the Virgo SA and the residual motion of the mirror*, Class. Quantum Grav., 19 (2002) 1631

[46] S.Grasso et al *Electrostatic systems for fine control of mirror orientation in interferometric GW antennas* (1998)

[47] M. J. Mortonson et al. *Effects of electrical charging on the mechanical Q of a fused silica disk* Rev. Scient. Instrum. 74 (2004)

[48] M. Hewitson et al. *Charge measurement and mitigation for the main test masses of the GEO 600 gravitational wave observatory* Class. Quantum Grav. **24** (2007) 6379.

[49] F. Acernese, F. Barone, A. Boiano, R. De Rosa, F. Garufi, L. Milano, S. Mosca, A. Perreca, G. Persichetti, R. Romano, *Application of a hybrid modular acquisition system to the control of a suspended interferometer with electrostatic actuators.* Jou. of Physics: Conf. Series **122** (2008) 012011.

[50] F.Acernese et al. *An optical readout system for the drag-free control of LISA* Class. Quant. Grav. **22** (2005) S279.

[51] W.Koechner *Solide-state laser engineering*, 1976.

[52] S.O. Kasap *Optoelectronics and Photonics*